UNIVERSITY OF CALIFORNIA
RIVERSIDE

Spectroscopy of Photovoltaic Materials: Charge-Transfer Complexes and Titanium Dioxide

A Dissertation submitted in partial satisfaction
of the requirements for the degree of

Doctor of Philosophy

in

Chemistry

by

Robert John Dillon

August 2013

Dissertation Committee:
Dr. Christopher J. Bardeen, Chairperson
Dr. Ludwig Bartels
Dr. David Bocian

The Dissertation of Robert John Dillon is approved:

_____

_____

_____

Committee Chairperson

University of California, Riverside

Acknowledgements

I am very thankful for having Professor Christopher Bardeen as my advisor. Without his wisdom, guidance, and, above all, patience, none of this would have been possible. I would also like to thank him for encouraging me and giving me multiple opportunities to attend professional conferences to present our work. I can't help but reflect that much of my professional development is due to his mentoring.

I would also like to thank Professors Francisco Zaera and Yadong Yin for allowing me to participate in their studies of titanium dioxide. As well as, Dr. Ji Bong Joo, who made most of the samples.

ABSTRACT OF THE DISSERTATION

Spectroscopy of Photovoltaic Materials: Charge-Transfer Complexes and Titanium Dioxide

by

Robert John Dillon

Doctor of Philosophy, Graduate Program in Chemistry
University of California, Riverside, August 2013
Dr. Christopher Bardeen, Chairperson

The successful function of photovoltaic (PV) and photocatalytic (PC) systems centers primarily on the creation and photophysics of charge separated electron-hole pairs. The pathway leading to separate carriers varies by material; organic materials typically require multiple events to charge separate, whereas inorganic semiconductors can directly produce free carriers. In this study, time-resolved spectroscopy is used to provide insight into two such systems: 1) organic charge-transfer (CT) complexes, where electrons and holes are tightly bound to each other, and 2) Au-TiO_2 core-shell nanostructures, where free carriers are directly generated.

1) CT complexes are structurally well defined systems consisting of donor molecules, characterized by having low ionization potentials, and acceptor molecules, characterized by having high electron affinities. Charge-transfer is the excitation of an

electron from the HOMO of a donor material directly into the LUMO of the acceptor material, leading to an electron and hole separated across the donor:acceptor interface. The energy of the CT transition is often less than that of the bandgaps of donor and acceptor materials individually, sparking much interest if PV systems can utilize the CT band to generate free carriers from low energy photons. In this work we examine the complexes formed between acceptors tetracyanobenzene (TCNB) and tetracyanoquinodimethane (TCNQ) with several aromatic donors. We find excitation of the charge-transfer band of these systems leads to strongly bound electron-hole pairs that exclusively undergo recombination to the ground state. In the case of the TCNB complexes, our initial studies were flummoxed by the samples' generally low threshold for photo and mechanical damage. As our results conflicted with previous literature, a significant portion of this study was spent quantifying the photodegradation process.

2) Unlike the previous system, free carriers are directly photogenerated in TiO_2, and the prime consideration is avoiding loss due to recombination of the electron and hole. In this study, four samples of core-shell Au-TiO_2 nanostructures are analyzed for their photocatalytic activity and spectroscopic properties. The samples were made with increasingly crystalline TiO_2 shells. The more crystalline samples had higher photocatalytic activities, attributed to longer carrier lifetimes. The observed photophysics of these samples vary with excitation wavelength and detection method used. We find the time-resolved photoluminescence correlates with the samples' photocatalytic activities only when high energy, $\lambda \leq 300$ nm excitation is used, while transient absorption experiments show no correlation regardless of excitation source. The results imply that

photoexcitation with high energy photons can generate both reactive surface sites and photoluminescent surface sites in parallel. Both types of sites then undergo similar electron-hole recombination processes that depend on the crystallinity of the TiO_2 shell. Surface sites created by low energy photons, as well as bulk TiO_2 carrier dynamics that are probed by transient absorption, do not appear to be sensitive to the same dynamics that determine chemical reactivity.

Table of Contents

List of Tables

List of Figures

Chapter 1: Introduction

1.1 Motivation

The solar energy incident on the Earth's surface amounts to 86 petawatts.[1] This amount of power over the course of half of a year exceeds the total amount of energy that will ever be had from all of Earth's non-renewable energy sources.[1] Besides the common sense of harnessing a power source as free and reliable as the sun, there are strong reasons for abandoning the use of non-renewable energy sources, fossil fuels in particular. Pollution and climate change threaten to ruin the long-term habitability of the planet. There is much speculation whether the buildup of unprecedented levels of CO_2 in the atmosphere released from the burning of fossil fuels has anything to do with recent trends in the weather, see Figure 1.1.[2] There is much evidence that particulate pollution from burning coal shortens lives.[3] The processes needed to harvest such fuels have severe environmental consequences such as oil spills and deforestation.

Nuclear energy is often promoted as clean, but in fact still generates dangerous radioactive waste that persists for thousands of years. Besides this, nuclear energy remains unpopular due to the devastating consequences of a mishap as well as its potential use as a guise for the manufacture of nuclear weapons. One final technology that remains somewhat distant is fusion power, but even this will generate long-lived hazardous radioactive waste.

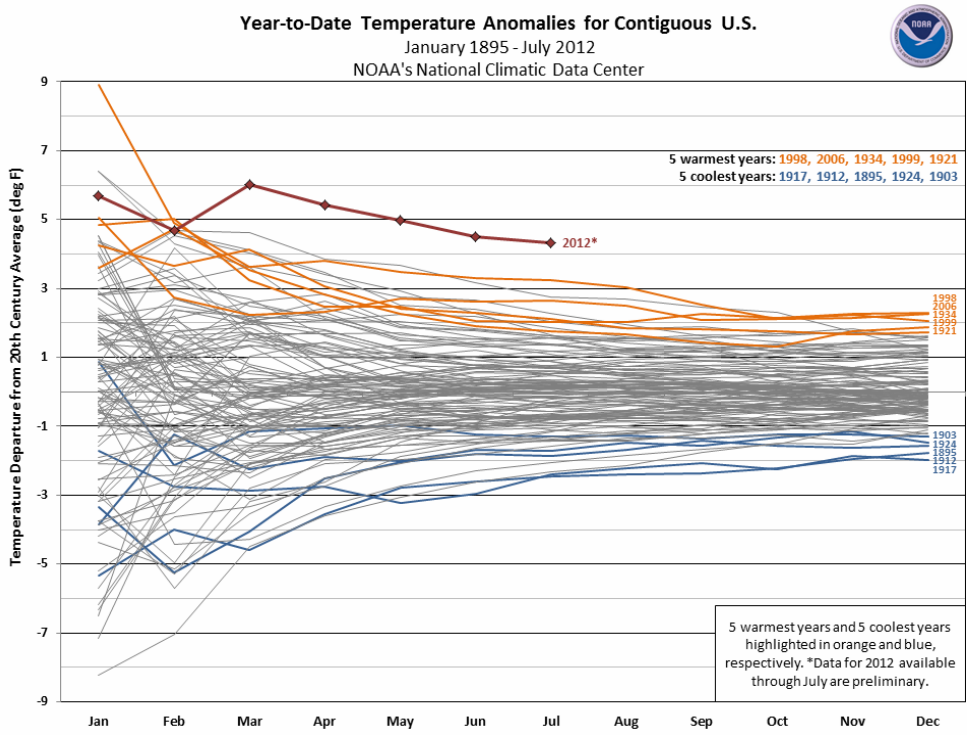

Figure 1.1: Monthly temperature data for the United States since 1895. The plot is the deviation from the average monthly temperature over the 20th century. Is it just coincidence that three of the five hottest years ever, are fairly recent? The year of this publication, 2012, is clearly on track to be the hottest year ever, and not by an insignificant margin. (from 2)

Considering that the sun is one gigantic fusion reactor located a safe distance away, is already fully functioning, and isn't going away any time soon, it seems somewhat silly that we should build an inferior one here on earth. Therefore, the study and improvement of photovoltaics and photocatalysts presents the best pathway to responsibly meeting the world's energy needs.

1.1 Introduction to Photovoltaics and Photocatalysts

Photovoltaics and photocatalysts primarily function from the light activated generation of an electron-hole pair, which is then separated into free electrons and holes. The separated charges can then be used to drive an external circuit or do redox chemistry. The formation and lifetime of the charge separated state is one of the most important aspects of these systems. However, other competing processes may also occur after photoexcitation that do not lead to free carriers but waste the energy instead. Time-resolved fluorescence and transient absorption are two of the most useful tools in evaluating what happens immediately after photoexcitation. In this work, two different systems which rely on photoinduced charge separation are examined: organic charge-transfer (CT) complexes and titanium dioxide (TiO_2) photocatalysts. For the CT complexes, it is shown that electron-hole recombination dominates over creation of free carriers, and therefore, while structurally these systems seem appealing for photovoltaics, by themselves they would not make viable photovoltaics. For the TiO_2 photocatalysts, it is shown that increasing the crystallinity of the TiO_2 slows down electron-hole recombination, enhancing the fluorescence lifetime and photocatalytic activity in tandem.

1.2 Photovoltaics

Figure 1.2 shows a timeline of different solar cells and their efficiencies since 1976.[4] Historically solar cells have almost exclusively utilized inorganic semiconductors[5], and they dominate the plot. Organic photovoltaics are found in the bottom right portion of the plot, having only recently reached efficiencies of approximately 10%. Inorganic and organic cells undergo different processes to arrive at the same end result: charge separated carriers driving a circuit. An understanding of how these systems work is useful in discussing how they may be analyzed spectroscopically.

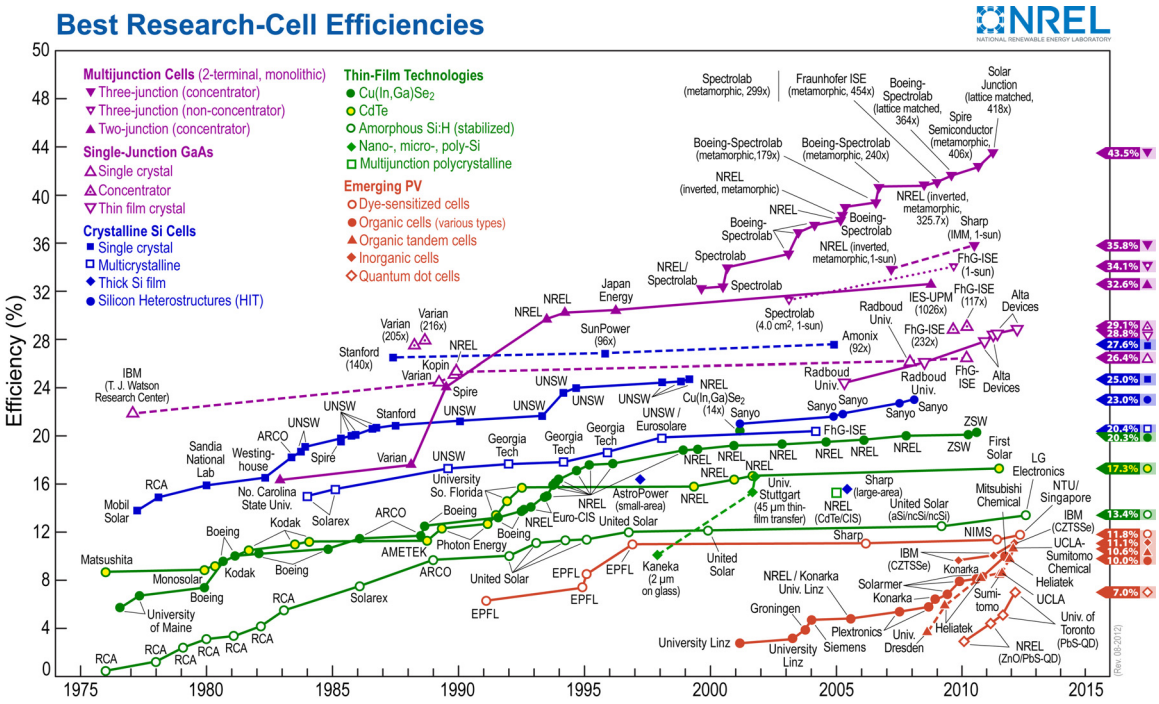

Figure 1.2: Timeline of solar cell technologies and their efficiencies. (from 4)

1.2.1 Inorganic Photovoltaics

One of the simplest cells to understand is the silicon photovoltaic, which consists of a bilayer of p-type and n-type silicon. The formation of the p-n junction is achieved simply by starting with a wafer of p-type silicon (1 ppm boron) and diffusing phosphorous into one side, forming a thin n-type layer less than a micrometer thick.[5] At the p-n junction, electrons from the n-type layer diffuse into the p-type layer, which produces an electric field. When irradiated with light with enough energy, electrons in the valence band can be excited to the conduction band, and are then driven to the n-doped side of the cell by the electric field. Figure 1.3 depicts this process.

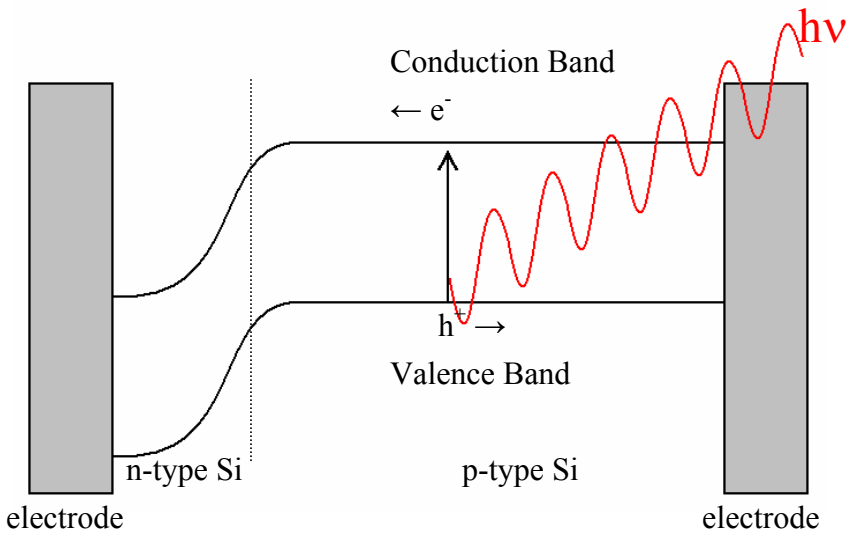

Figure 1.3: Diagram of a simple silicon solar cell.

The bandgap for silicon is 1100 nm; photons with less energy are not absorbed, while photons with more energy are absorbed, but the extra energy is lost as heat. The maximum predicted efficiency of a single junction silicon solar cell is 29% according to the Shockley-Queisser limit which takes into account the balance of photons too low in energy to be absorbed and the photons with too much energy, as well as other energy losses.[6] As shown in Figure 1.2, modern single junction cells are pretty close to this limit. Also shown in Figure 1.2 are multi-junction cells, where by pairing together different semiconductors with different bandgaps much greater efficiencies may be attained. This is achieved by simultaneously absorbing more low energy photons with a low bandgap semiconductor and wasting less of the high energy photons excess energy with a high bandgap semiconductor.

1.2.2 Organic Photovoltaics

Organic photovoltaics have only recently become viable alternatives to those comprised of inorganic semiconductors. As the inorganic semiconductors often require expensive processing techniques and high purity,[5] one of the prime reasons for studying organic based photovoltaics is that they are generally much cheaper and not as reliant on highly purified materials. Figure 1.2 reports the first viable organic solar cell arrived in 2001, with an efficiency of 2.5%.[7] Organic solar cells have been around since the 1950's, but were typically based on crudely sandwiching a single organic compound between two different metal electrodes, with efficiencies less than 1%, if they could be measured at all.[8] The first organic-organic bilayer cell was produced by Tang in 1986, and operated in

a similar manner to the silicon p-n junction cell, utilizing the highest occupied molecular orbital (HOMO) and lowest unoccupied molecular orbital (LUMO) of aromatic organic molecules instead of the valence and conduction bands found in inorganic semiconductors.[9] Without the band structure of a semiconductor, organic photovoltaics rely on a delocalized π-electron system for charge transport, which is in turn dependent on the crystallinity of the material itself.

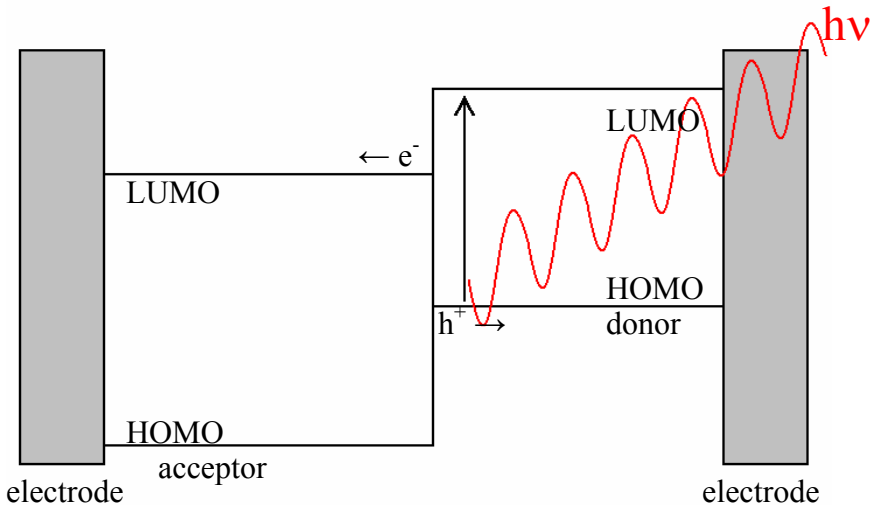

Figure 1.4: Diagram of an organic bilayer solar cell. The donor material is photoexcited and charge separation occurs at the donor-acceptor interface.

The energy level diagram for a simple organic solar cell is shown in Figure 1.4. In this cell the donor material is excited, creating an exciton (electron-hole pair). If the exciton is sufficiently close to the interface of the donor and acceptor, then charge separation may occur as the electron moves to the LUMO of the acceptor material. If the

donor material is excited too far away from the interface, then the exciton will simply relax before it can charge separate. The typical exciton diffusion length for organics is less than 20 nm.[10] This short diffusion length is one of the principle problems of organic photovoltaics. A very thin cell might solve this problem, but at the cost of less material to absorb light overall.

One solution to the diffusion length limitation is the bulk heterojunction (BHJ) cell, where the donor and acceptor are all mixed together. Typically this is done by simultaneous deposition, usually by spin-coating a film from a solution containing both donor and acceptor. The result is a random mix of donor and acceptor that naturally has a donor-acceptor interface throughout the whole film. The system also relies on there existing continuous regions of donor and acceptor such that the separated charges can reach their respective electrodes. In some cases the regions of pure donor or acceptor are too big, resulting in the dead space problem inherent in bilayer cells. One of the most studied donor:acceptor pairs has been the combination of poly(3-hexylthiophene) (P3HT) and Phenyl-C61-butyric acid methyl ester (PCBM), which has shown efficiencies of about 5%. Due to the random nature of creating a BHJ, numerous publications report tricks to tweak the mixing and different processing conditions to make more efficient P3HT:PCBM photovoltaics.[10-12] For example, one of the most studied experimental parameters is the annealing temperature and duration. Annealing for a short duration at a low temperature (5 min at 75 - 115 C) tended to only affect the P3HT crystallinity, annealing for longer times or at higher temperatures resulted in phase separation of the PCBM as it crystallized into needles and fans.[12] Lack of crystallinity of the donor phase

represents one of the key problems of BHJ's, as the polymer donor's poor hole-transport properties become one of the main limiting factors for the cell.[13]

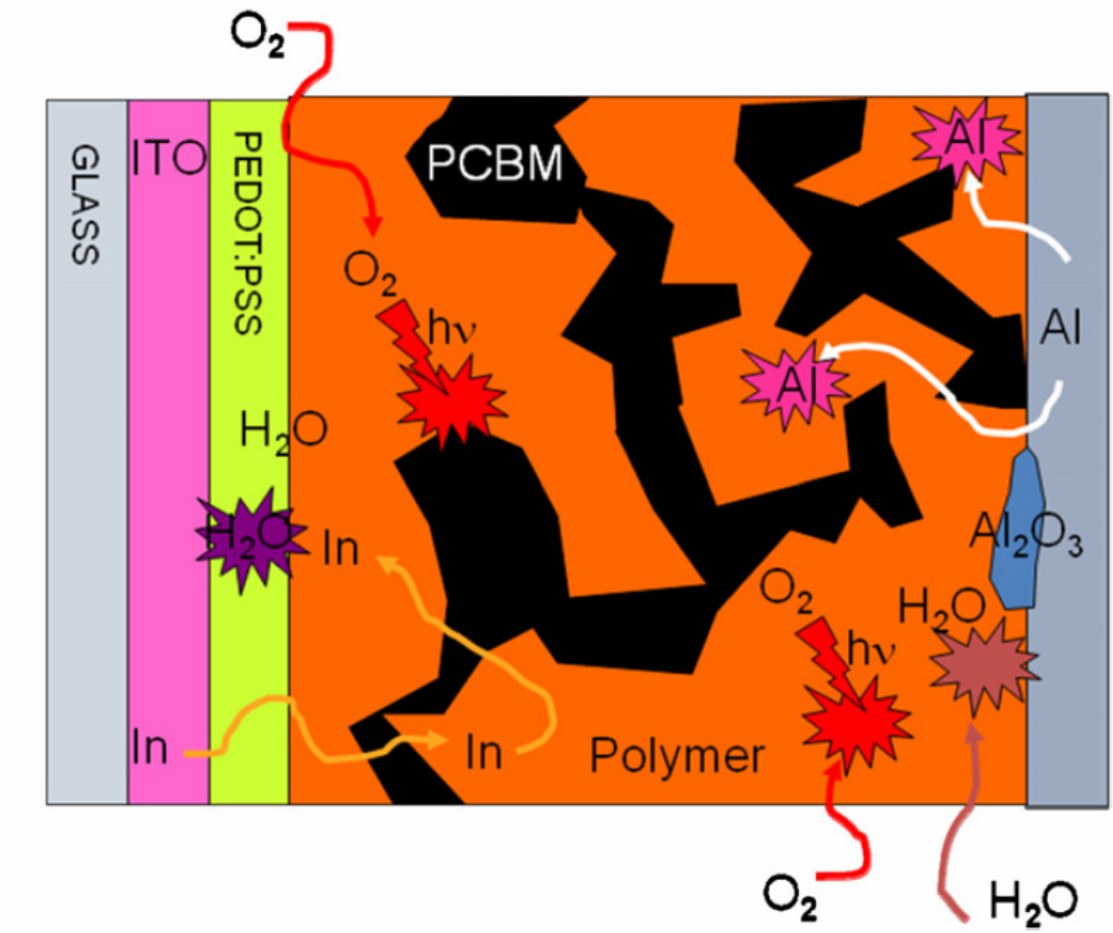

Figure 1.5: Diagram of a typical P3HT:PCBM photovoltaic and all of the things that can ruin it. (from 14)

One final comment on all-organic photovoltaics is their durability, or their lack thereof. Figure 1.5 depicts several of the key processes detrimental to a BHJ, the details of which are beyond the scope of this dissertation. In summary, diffusion of oxygen and water into the cell cause the most damage, and the ideal organic donor material, in terms of absorbing the solar spectrum, typically has a small HOMO-LUMO gap that inherently makes it easily photoxidized, either directly or via singlet oxygen generation.[14]

1.2.3 Charge-Transfer Compounds as Ideal BHJ's

While the BHJ achieves its functional structure through random mixing, as seen in the preceding section, this process entails many problems. One possible solution is to use organic materials that reproducibly self-assemble into donor-acceptor assemblies, such as charge-transfer complexes. For example, Figure 1.6 shows a side view of the crystal structure of the photoconductive charge transfer complex formed by pyrene with TCNQ.

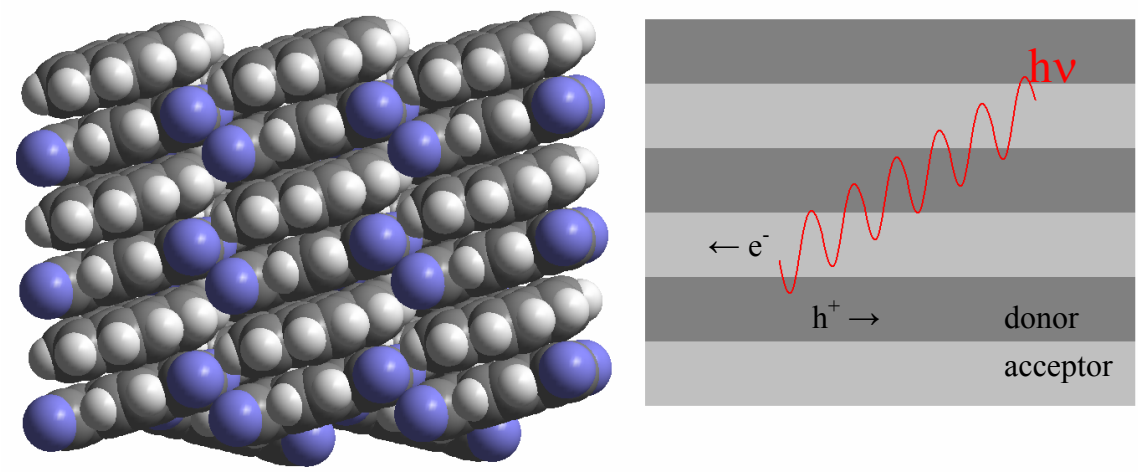

Figure 1.6: Side view of the pyrene:TCNQ crystal structure and schematic of the donor-acceptor layers. The blue molecules are the nitrogens on TCNQ.

Pyrene:TCNQ is classified as a "mixed stack" crystal, where stacks of alternating donor and acceptor crystallize next to each other. However there is some overlap of the π orbitals between adjacent TCNQ molecules, but very little overlap between adjacent pyrenes. The condition of good overlap of either donor or acceptor, but not both is

thought to be the driving factor in separating the electron hole pair, permitting photoconductivity.[15] Looking at the right side of Figure 1.6, the alternating layers of the system resemble the ideal interdigitated donor-acceptor structure of a BHJ, except on the molecular level. This in effect solves the phase separation issue in traditional BHJ's, where dead zones of pure donor or acceptor degrade the device.

Another consideration for using these materials as photovoltaics is the potential for better solar spectral-overlap. When organic donor and acceptor compounds form complexes, an additional charge-transfer transition is possible, where an electron may be excited from the HOMO of the donor directly into the LUMO of the acceptor material. Figure 1.7 shows an example of charge transfer in a bilayer photovoltaic. The energy gap for the excitation of the charge-transfer band is clearly dependent on the relative energies

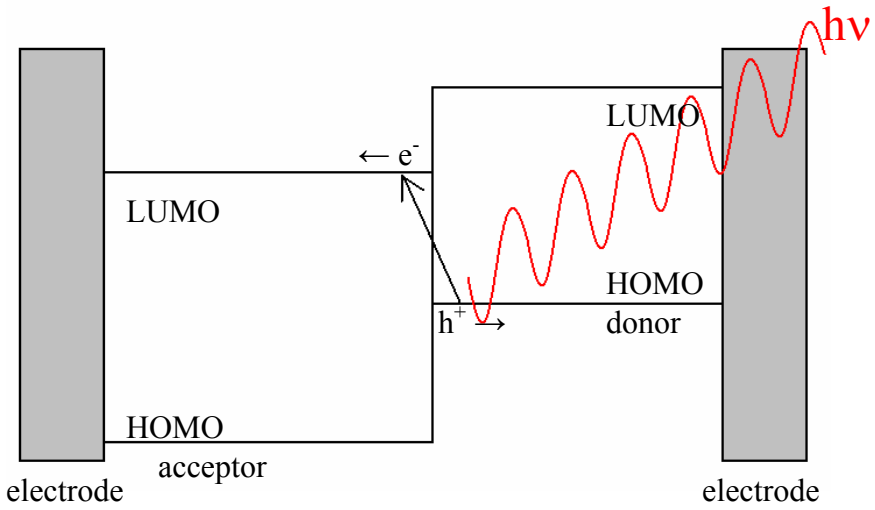

Figure 1.7: Diagram of an organic bilayer solar cell where charge-transfer is taking place. In contrast to the cell shown in Figure 1.4, here the photoexcitation excites an electron from the donor directly into the LUMO of the acceptor.

of the two materials and, in this example, requires less energy than direct excitation of the donor or the acceptor. The energy for the charge-transfer transition can be approximated by the expression:

$$h\nu_{CT} = I_D - E_A - \Delta_C + V_B \quad (1.1)$$

where I_D is the ionization energy of the donor, E_A is the electron affinity of the acceptor, Δ_C is a Coulombic force term from bringing the molecules close to each other, and V_B is a valence bond term due to the overlap of the donor and acceptor wavefunctions.[16] With a charge-transfer complex, two UV absorbing materials can combine to yield a crystal that absorbs all across the visible spectrum into the near-IR - as is the case with pyrene:TCNQ. This also enhances the stability of the system by completely avoiding low-bandgap materials such as those found in BHJ's which are easily photoxidized.

1.2.4 Spectroscopy of Charge-Transfer Complexes

An open question is whether charge-transfer crystals could be used as photovoltaics. Rather than going through the potentially lengthy process of manufacturing a device, time-resolved spectroscopy may be used to monitor the excited state to determine if electron-hole pairs are produced and if they can charge separate, as is needed in a functional cell. In fact, the photophysics of a family of charge-transfer complexes, all with tetracyanobenzene (TCNB) as the acceptor have already been studied in the literature.[17] These complexes were shown to exhibit bicomponent decay kinetics that were attributed to two processes: fast recombination of the electron and hole, and long-lived free carrier production (in some cases less than half of the induced absorption

decayed at the limit of the investigators time resolution, ~4ns).[17] While this family of complexes does not overlap very well with incident solar light, the results suggested that CT complexes could work as photovoltaic devices.

The promising literature results for the TCNB complexes were based solely on transient absorption measurements. In chapter 3 we revisit these compounds using time-resolved fluorescence and transient absorption, where we find that the TCNB complexes are actually a troublesome system to study and that the results of reference 17 are likely incorrect. The TCNB complexes all exhibited bright and long-lived fluorescence, which was one of the first indicators that the excited state was relaxing radiatively as opposed to forming charge carriers, which would have quenched the fluorescence. These samples were also prone to photodamage, which distorted their kinetics. Initial transient absorption experiments were similar to those previously reported in the literature, but when the laser excitation power was significantly lessened, the kinetics became much slower and simpler. Chapter 3 systematically characterizes the effects of photodamage that likely affected the results in previous literature.

Chapter 4 focuses exclusively on the photophysics of one complex, pyrene:TCNQ. This particular complex was much more stable than the TCNB complexes, and also had a much shorter fluorescent lifetime. Experimental limitations on the transient absorption setup, as well as the sample damage problems, prevented full measurement of the decay kinetics for the TCNB compounds. With pyrene:TCNQ it was possible to fully measure the decay of its induced absorption and compare it to its time-resolved fluorescence. For pyrene:TCNQ, the CT complex we felt was among the most promising as a photovoltaic

material, we show that photoexcitation produces nothing but tightly bound electron-hole pairs that rapidly recombine with each other with simple monoexponential kinetics. The inability of the charges to separate precludes the use of this material in a photovoltaic device.

1.3 Photocatalysis

Spectroscopy on the CT complexes was mainly to evaluate if they could work as photovoltaics at all; in this section we examine a well established working photocatalytic system. Semiconductor photocatalysts undergo similar processes as photovoltaics, except instead of generating electricity, the photogenerated electrons and holes are used to do redox chemistry, typically on the surface of the catalysts itself.

1.3.1 TiO_2

The semiconductor TiO_2 has been used to catalyze several types of reactions including oxidation, oxidative cleavage, reduction, isomerization, substitution, condensation, and polymerization.[18] The band structure of TiO_2 is also suitable for one of the most sought after processes: water splitting, where water is oxidized and reduced simultaneously, producing O_2 and H_2 respectively, see Figure 1.8. H_2 is the ultimate clean fuel, as its combustion product is simply water. TiO_2 is not the only photocatalyst capable of splitting water, reference 19 reports the details of more than 130 different catalysts, some of which are much better than TiO_2. Nevertheless, research on TiO_2 continues because it is abundant, stable, inexpensive, and non-toxic. These last two points are really

underscored when considering some of the current applications of TiO_2. For example, while other photocatalysts could potentially do the same job, TiO_2 powders added to polluted water can completely mineralize the organic pollutants in the water, while it itself is not a pollutant and is so cheap it might as well not be recovered.[20]

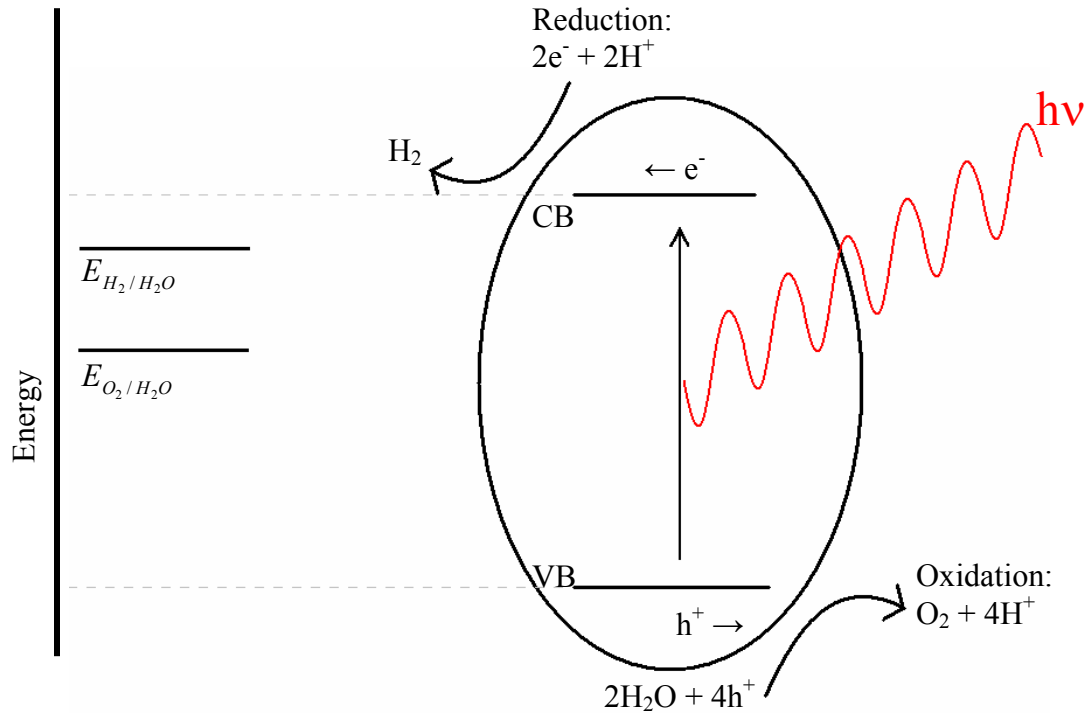

Figure 1.8: Photocatalytic water-splitting.

Figure 1.8 shows the water-splitting process where an electron is photoexcited into the conduction band (CB) where it can then reduce 2H+ to H_2, meanwhile the hole in the valence band (VB) oxidizes the H_2O to O_2. On the left side of the figure are the

reduction potentials for hydrogen and oxygen reduction; as is required for both processes to occur, the conduction band is above the reduction potential for H_2/H_2O, and the valence band is well below the potential for O_2/H_2O. While enabling it to split water, the large bandgap of TiO_2 (3.2 eV) requires UV excitation which limits its practical use for harvesting solar energy. Limited success has been achieved by narrowing the bandgap by doping with Ti^{3+}, C, and N,[19-24] but so far the efficiencies of these devices are too low to be of practical use.

Besides the use of dopants, a significant amount of work has been done to study the effect of the TiO_2 crystal morphology on catalysis, where the photocatalytic activity is enhanced owing to better electron-hole separation or the generation of more catalytically active surfaces. Many studies of this type typically encompass catalysis experiments on TiO_2 powders manufactured by different companies with different particle sizes, crystal phases, crystallinities, or other differences.[25-26] Spectroscopic experiments, transient absorption and photoluminescence, have so far taken the same route, where the samples have been for the most part completely different, and the results not very insightful owing to the sample variation as well as the use of excessive laser fluence.[28-29] One of the most cited articles on the transient absorption of TiO_2 reports results on a self-made sample that is not evaluated at all for photocatalytic activity.[30]

In chapter 5, we present a systematic spectroscopic and photocatalytic study of unique Au@TiO_2 yolk-shell structures with varying degrees of crystallinity. These samples consist of a 20 nm gold particle inside of hollow anatase TiO_2 nanospheres. The crystallinity is varied by the calcination and etching conditions. As the crystal grain size

increases, the photocatalytic activity (measured by H_2 production) predictably increases as well; we show that the spectroscopic observables also change, but these changes only manifest themselves in photoluminescence experiments, under specific excitation conditions.

References

1. Hermann, W. *Energy* **2006**, *31*, 1685–1702.

2. National Climatic Data Center. http://www1.ncdc.noaa.gov/pub/data/cmb/images/us/2012/jul/YTD_allyears_Jul2012.png (accessed Aug 18, 2012).

3. Iii, C. A. P.; Burnett, R. T.; Thun, M. J.; Calle, E. E.; Krewski, D.; Thurston, G. D. *Journal of the American Medical Association* **2002**, *287*, 1132–1141.

4. National Renewable Energy Laboratory. http://www.nrel.gov/ncpv/images/efficiency_chart.jpg (accessed Aug 20, 2012)

5. Green, M. A., Crystalline Silicon Solar Cells. In *Clean Electricity From Photovoltaics*; Archer, M. D., Hill, R. Ed; Imperial College Press: London, United Kingdom, **2005**, 1-49.

6. Shockley, W., Queisser, H. J. *Journal of Applied Physics* **1961**, *32*, 510–519.

7. Shaheen, S. E.; Brabec, C. J.; Sariciftci, N. S.; Padinger, F.; Fromherz, T.; Hummelen, J. C. *Applied Physics Letters* **2001**, *78*, 841.

8. Chamberlain, G. a. *Solar Cells* **1983**, *8*, 47–83.

9. Tang, C. W. *Applied Physics Letters* **1986**, *48*, 183–185.

10. Hoppe, H.; Sariciftci, N. S. *Journal of Materials Research* **2004**, *19*, 1924–1945.

11. Vakhshouri, K.; Kozub, D. R.; Wang, C.; Salleo, A.; Gomez, E. D. *Physical Review Letters* **2012**, *108*, 026601.

12. Swinnen, A.; Haeldermans, I.; Vanlaeke, P.; Haen, J. D.; Poortmans, J.; Olieslaeger, M. D.; Manca, J. V **2007**, *256*, 251–256.

13. Coakley, K. M.; Srinivasan, B. S.; Ziebarth, J. M.; Goh, C.; Liu, Y.; McGehee, M. D. *Advanced Functional Materials* **2005**, *15*, 1927–1932.

14. Jørgensen, M.; Norrman, K.; Krebs, F. C. *Solar Energy Materials and Solar Cells* **2008**, *92*, 686–714.

15. Vincent, B. Y. V. M.; Wright, J. D.; Ct, K. *Journal of the Chemical Society, Faraday Transactions 1* **1974**, *70*, 58–71.

16. Haarer, D. Optical and Photoelectric Properties of Organic Charge Transfer Crystals. In *Festkörperprobleme 20*; Treusch, J., Ed.; Springer: Berlin, **1980**; pp. 341–367.

17. Hubig, S. M.; Kochi, J. K. *Journal of Physical Chemistry* **1995**, *99*, 17578–17585.

18. Fox, M. A.; Dulay, M. T. *Chemical Reviews* **1993**, *93*, 341–357.

19. Ni, M.; Leung, M. K. H.; Leung, D. Y. C.; Sumathy, K. *Renewable and Sustainable Energy Reviews* **2007**, *11*, 401–425.

20. Schrauzer, G. N., Guth, T. D. *Journal of the American Chemical Society* **1977**, *99*, 7189–7193.

21. Zuo, F.; Bozhilov, K.; Dillon, R. J.; Wang, L.; Smith, P.; Zhao, X.; Bardeen, C.; Feng, P. *Angewandte Chemie* **2012**, *124*, 6327–6330.

22. Park, J. H.; Kim, S.; Bard, A. J. *Nano letters* **2006**, *6*, 24–8.

23. Khan, S. U. M.; Al-Shahry, M.; Ingler, W. B. *Science* **2002**, *297*, 2243–5.

24. Cong, Y.; Zhang, J.; Chen, F.; Anpo, M. *Journal of Physical Chemistry C* **2007**, *111*, 6976–6982.

25. Liu, Z.; Hou, W.; Pavaskar, P.; Aykol, M.; Cronin, S. B. *Nano Letters* **2011**, *11*, 1111–6.

26. Kato, H.; Asakura, K.; Kudo, A. *Journal of the American Chemical Society* **2003**, *125*, 3082–9.

27. Furube, A.; Asahi, T.; Masuhara, H.; Yamashita, H.; Anpo, M. *The Journal of Physical Chemistry B* **1999**, *103*, 3120–3127.

28. Colombo, D. P.; Bowman, R. M. *Journal of Physical Chemistry* **1995**, *99*, 11752–11756.

29. Katoh, R.; Murai, M.; Furube, A. *Chemical Physics Letters* **2010**, *500*, 309–312.

30. Yoshihara, T.; Katoh, R.; Furube, A.; Tamaki, Y.; Murai, M.; Hara, K.; Murata, S.; Arakawa, H.; Tachiya, M. *The Journal of Physical Chemistry B* **2004**, *108*, 3817–3823.

Chapter 2: Experimental

This chapter contains the experimental details for the experiments discussed in this work. Section 2.1 describes the preparation of the charge transfer crystals and powders as well the TiO_2 samples studied. Section 2.2 describes the typical methods of sample characterization (imaging, photocatalytic activity, steady-state spectroscopy). Section 2.3 describes in detail the laser systems, optical layouts, and instruments for the time-resolved experiments performed, and section 2.4 outlines the exact parameters used for each of the time-resolved experiments.

2.1 Sample Preparation

2.1.1 CT Sample Preparation

Complexes with TCNB as the acceptor were prepared by adding stoichiometric amounts (about 8 mg of TCNB and 6-9 mg of donor) to 2 mL of acetone in a glass vial. All compounds were obtained from Sigma Aldrich and were used without further purification (sublimation and recrystallization did not prevent the anomalous photokinetics described in chapter 3). This was covered with foil and left undisturbed to evaporate slowly. The pyrene:TCNQ complex was prepared similarly but in THF solution in a petri dish, a few drops of xylenes were also added to slow the evaporation process. A few of the biggest crystals were kept for single crystal fluorescence lifetime measurements, others were picked out and used to make the diffuse reflectance powder samples. Table 2.1 lists the specific crystals and their qualities.

Table 2.1: CT crystal properties.

Complex	Color	Shape
Naphthalene:TCNB	yellow	rods
Durene:TCNB	light yellow	prisms
Phenanthrene:TCNB	yellow	ribbons/needles
Pyrene:TCNB	orange	ribbons
9-Methylanthracene:TCNB	orange-red	ribbons/needles
Pyrene:TCNQ	black	rods

Powder samples were prepared by adding a few of the crystals (~6 mg) to $BaSO_4$ (1-4 μm, Alfa Aesar) powder or Teflon (1 μm, Sigma Aldrich) powder (~294 mg), and crushing them together for at least 25 minutes in an agate mortar and pestle resulting in a 2 %wt sample. Great care must be taken when Teflon powder is used as it tends to fly out of the mortar very easily. The best way to prepare samples in Teflon is to add the Teflon slowly; as the pulverized crystal sample mixes with the Teflon it helps to prevent it from getting everywhere. After ~25 minutes of grinding, the powder samples should appear uniform in color and no tiny crystals should be visible in the powder. The final color of the powder should also match the original color of the crystal, albeit lightened (ex. a red crystal should produce a pink powder); if the color changes, either the donor or acceptor of the complex has reacted with impurities in the dilutant.

Random polycrystalline films of CT crystals were prepared using a Laurell WS-400B-6NPP/LITE Single Wafer Spin Processor. Solutions containing stoichiometric amounts (about 5mg each of donor and acceptor) in 2 mL of THF were used to cover a small microscope slide, which was then spun at 2000 rpm for 30 seconds. These films contained significant amounts of monomer, but were still useful given that the monomer components absorbed only UV light, whereas the CT absorption band(s) were much lower in energy. An example is shown in Figure 2.1.

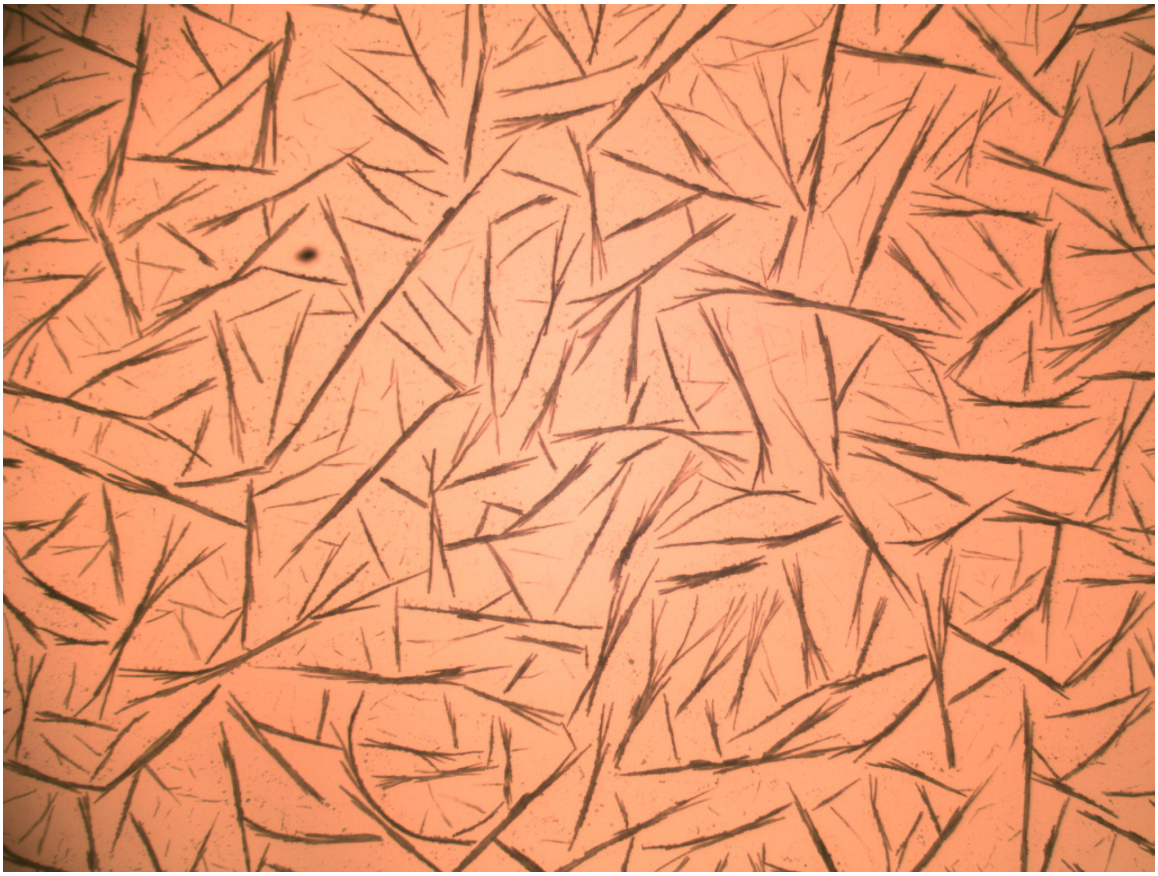

Figure 2.1: Image of random film of pyrene:TCNQ CT rods taken with the DCM300 camera.

Films of aligned pyrene:TCNQ microrods were made by dipcoating glass substrates into a concentrated THF solution of donor and acceptor (about 70 mg each of donor and acceptor in 10 mL). Using the slowest setting on the home-made motorized dip coater, the sample was retrieved very slowly while a current of air was blown over it. With some adjustment of the air flow, rows of aligned CT crystals could be grown, as seen in Figure 2.2.

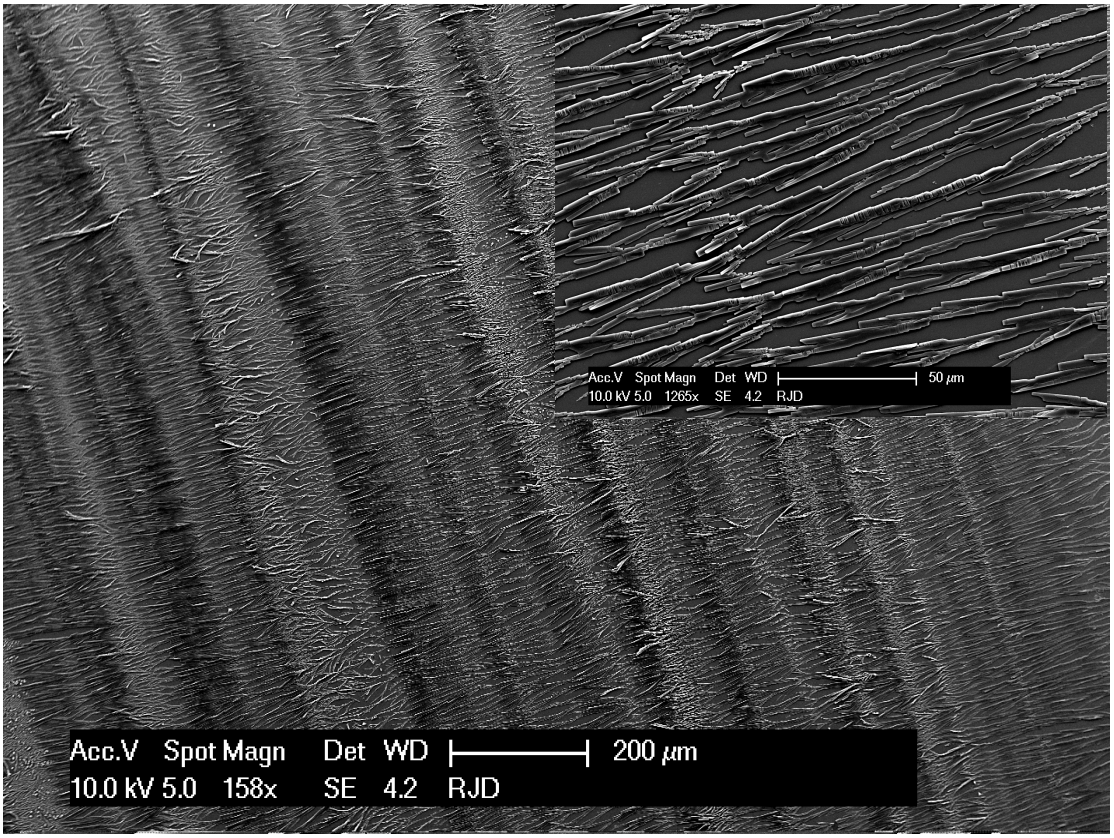

Figure 2.2: SEM image of aligned pyrene:TCNQ microrods. The alternating layers of light and dark occur as the surface of the solution undulates slightly due to the air current used to hasten solvent evaportation.

2.1.2 TiO_2 Sample Preparation

Au@TiO_2 yolk-shell samples were prepared by Dr. Ji Bong Joo in the Yin research group according to his previously published methods.[1] Four samples with different crystallinity were prepared starting from the same colloidal solution of gold nanoparticles. The particles were coated sequentially with silica, titania, and another silica layer via sol-gel processes, and then calcined and etched.

Au nanoparticles were prepared starting with an aqueous solution of $HAuCl_4$-$3H_2O$ (2.54 M, 18 μL) added to deionized water (30 mL) and heated to boiling point (100ºC). A sodium citrate solution (3 wt%, 1 mL) was added, and the resulting mixture was kept for 30 min under stirring. Upon cooling down to room temperature, an aqueous polyvinyl pyrrolidone (PVP) solution (Mw, 40,000, 12.8 mg/mL, 0.235 mL) was added and the solution was kept overnight under stirring to allow for the adsorption of PVP on the Au surface. The Au nanoparticles were separated from the solution by centrifugation, and re-dispersed in water (5 mL).

The particles were then coated with silica by taking some of the PVP treated Au solution (1 mL) and sequentially mixing with water (3.3 ml), ethanol (23 mL), tetraethyl orthosilicate (TEOS, 0.86 mL), and an aqueous solution of ammonia (28%, 0.62 mL). The reaction mixture was stirred for 4 h at room temperature, and then the resulting Au@SiO_2 particles were separated by centrifuging and washed three times with ethanol. Finally, the particles were re-dispersed in ethanol (20 ml) under sonication.

The above-mentioned Au@SiO_2 solution (20 ml) was dispersed in a mixture containing hydroxypropyl cellulose (HPC 400 mg), ethanol (80 mL) and water (0.48 mL).

After the reaction mixture had been stirred for 30 min, a solution of tetrabutyl titanate (TBOT, 4 ml) dissolved in ethanol (18 mL) was slowly added to the above solution using a syringe pump (0.5 mL/min). After injection, the temperature was increased to 85ºC while the reaction mixture was stirred for 90 min under reflux conditions. The precipitate which contained $Au@SiO_2@TiO_2$ nanocomposites, was collected using centrifugation, washed with ethanol and re-dispersed in the deionized water (40 mL). PVP (Mw, 40,000, 0.8 g) was added into the solution and it was kept overnight under stirring to allow for the adsorption of PVP on the TiO_2 surface. The $Au@SiO_2@TiO_2$ particles were separated using centrifugation, washed and re-dispersed in ethanol (20 mL).

The PVP treated $Au@SiO_2@TiO_2$ solution (20 mL) was then sequentially mixed with water (17.2 mL), ethanol (72 mL), tetraethyl orthosilicate (3.44 mL) and an aqueous solution of ammonia (28%, 2.48 mL). The reaction mixture was stirred for 4 h at room temperature, and then the resulting $Au@SiO_2@TiO_2@SiO_2$ particles were separated by centrifuging, washed three times with ethanol, and finally calcined in air at 800ºC for 4 h to crystallize the amorphous TiO_2 to small anatase TiO_2 grains. At this point the particles were divided into four different portions. Sample **A** was obtained by completely etching out the inner and outer layer of silica by using NaOH solution at 90ºC, centrifuging, and washing.

Samples **C-D** were prepared as follows: The calcined $Au@SiO_2@TiO_2@SiO_2$ particles (170 mg) were dispersed in 30 mL of water under ultrasonication and etched with NaOH solution (typically, 0.5 mL, 2.5 M) at 90 oC for 1 h. During the etching process, the silica layers were dissolved out preferentially near or inside the TiO_2 layer

and it produce a small gap small gap between SiO_2 and TiO_2 layers which allows space for the TiO_2 to further grow into large crystal grains. The partially etched $Au@SiO_2@TiO_2@SiO_2$ particles were then isolated by centrifugation, washed 5 times with de-ionized water, dried under vacuum, re-calcined in air at the desired temperature for a certain period (e. g. 4 or 16 h) to enhance the crystallinity of the TiO_2, and finally etched in a mixture of water (30 mL) and NaOH (2 mL, 2.5 M) at 90º C for 2 h to completely remove the silica. The samples were isolated by centrifugation, washed 5 times with de-ionized water, and dried. Sample **B** was re-calcined at 700ºC for 4 h, Sample **C** was re-calcined at 800ºC for 4h, and Sample **D** was re-calcined at 800ºC for 16 h, respectively. The degree of crystallinity was characterized with powder x-ray diffraction using a Bruker D8 Advance X-ray powder diffractometer (CuKα radiation, l = 1.5406 Å).

2.2 Sample Characterization

2.2.1 Imaging

Routine imaging of samples was done with an Olympus IX70 microscope as well as simpler microscopes. ScopePhoto software and a DCM300 camera were used to capture images. Scanning Electron Microscopy (SEM) was performed with an XL30-FEG scanning electron microscope in the UCR Central Facility for Advanced Microscopy and Microanalysis. The typical accelerating voltage used to image the samples was 10-15 kV. Film samples were affixed to SEM stubs with conductive copper tape, and, if need be, sputter coated with gold or platinum with a Cressington 108 Auto sputter coater for a few seconds. Transmission Electron Microscopy (TEM) on the TiO_2 samples was performed by Dr. Ji Bong Joo on a Tecnai T12 microscope.

2.2.2 Photocatalytic Activity of the TiO_2 Samples

Photocatalytic tests for hydrogen production were performed by Dr. Ji Bong Joo with a pyrex glass reactor system. The photocatalyst (5 mg) was suspended in 50 ml of an aqueous methanol solution (10 vol%). An Opti-Quip 100 W Hg lamp was used as a light source for irradiation. This lamp did not have sufficient output to measure the spectral dependence of the hydrogen output. The amount of hydrogen produced was determined by gas chromatography (HP 5890, equipped with a Molecular sieve 5A, Restel, packed column) with thermal conductivity detection. A diagram of the setup is shown in Figure 2.3.

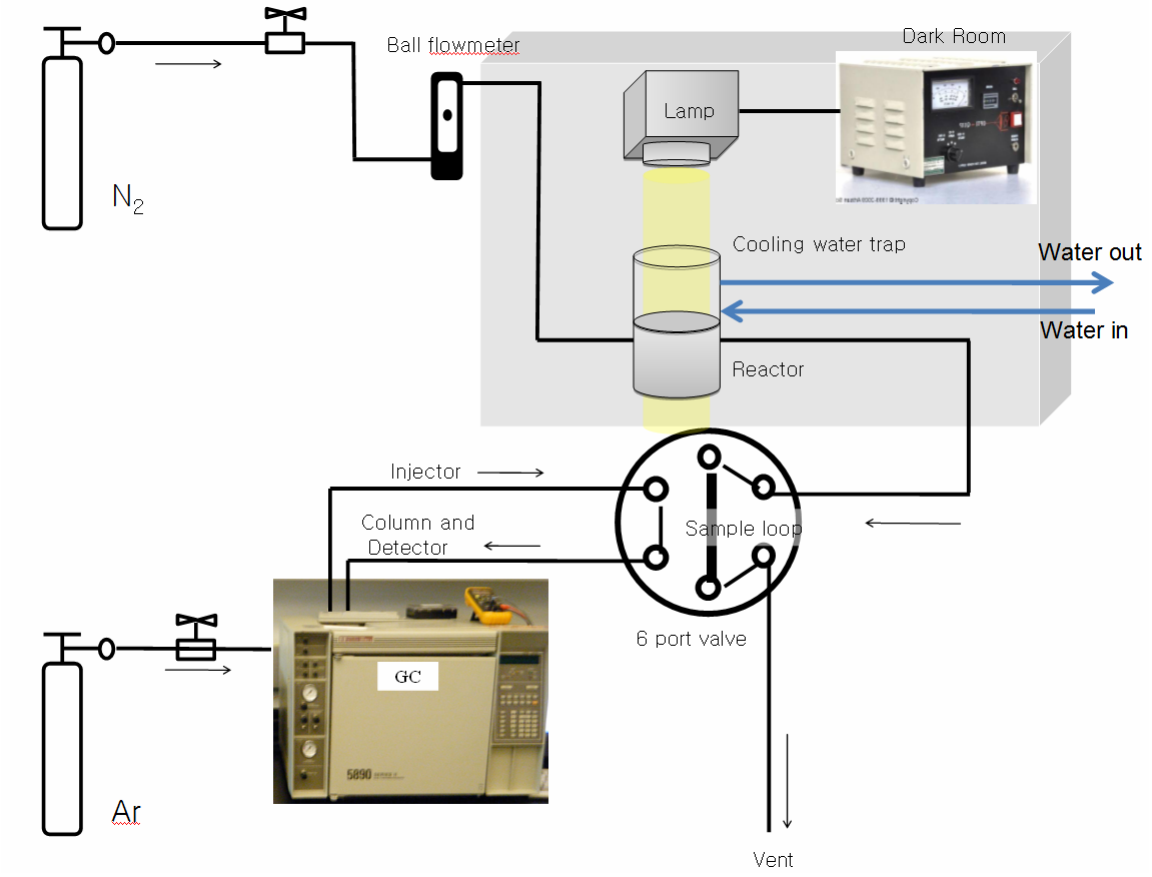

Figure 2.3: Reactor setup for measuring the photocatalytic production of hydrogen by the Au@TiO_2 samples with a gas chromatograph.

2.2.3 Steady-state Absorption & Diffuse Reflectance

Steady-state UV-Vis absorption spectra were taken with a Varian Cary 50 spectrometer, or with an Ocean Optics SD2000 with a Analytical Instrument Systems Model DT 1000 light source. A clean glass slide, air, or a cuvette containing pure solvent were used as sample blanks as needed.

Steady state diffuse reflectance measurements were also performed with the Ocean Optics SD2000 and the Analytical Instrument Systems Model DT 1000 light source. An example of the setup is shown in Figure 2.4. The output lens on the source fiber is adjusted to achieve the smallest spot possible on the sample, then another lens is used to collect the scatter and direct it into the detector fiber. The powder sample and reference sample are simultaneously sandwiched between two transparent substrates on a translation stage (points A and B in Figure 2.4). The translation stage is necessary so that the sample and the reference may be compared under the same geometry and conditions. The choice of lenses and absolute distances is not critical, less optimal setups will simply require longer integration times but are still workable. The angle of the incident beam on the samples is important and should be as close to normal as possible; specular reflection off of the sample or substrate into the detector will distort the results. As the signal for these experiments is typically very low, room lights and other lightsources (the computer monitor used in the experiment!) should be turned off or minimized.

Three scans are necessary for a steady-state diffuse reflectance measurement and should be performed in the following order:

1) Reference: the optical dilutant ($BaSO_4$, MgO, Teflon, et cetera) in the sample to be studied should be used as the reference sample. This sample, since it contains nothing that will absorb light, will have the most intense scatter. For this reason, scanning it first allows for easier optimization and also prevents saturating the detector later on when switching to the other sample(s). The integration time for the detector is increased until the peak signal is about 3500 - 3800 out of a maximum of 4000 counts. Depending on the integration time, a feasible number of averages should be chosen next. These values are then kept constant for the remaining scans. For some samples, such as UV absorbers, it may be known ahead of time where the absorption will roughly be - and that there is no (or no important) absorption in the visible spectral region where the lamp is most intense. In this case it is sometimes useful to increase the integration time past the point of saturation (of the peak lamp signal) to get more signal at other wavelengths.

2) Sample: After the reference scan, the translation stage is used to carefully switch to the sample which is then scanned under the same conditions. This scan typically looks very similar to the reference scan, but is usually less intense. If the signal too low, then the number of scans may be increased to achieve better signal to noise, but the integration time must stay the same.

3) Dark Scan: Once the sample scan is done, the light source is either turned off or blocked, and the sample scanned again. This scan is necessary to account for the dark current and electrical noise in the detector, which can be significant at the long

integration times necessary for diffuse reflectance measurements. It is subtracted from both of the previous scans.

Once all three scans are acquired the Kubelka-Munk equation, 2.1, is used to plot the spectrum:

$$f(R_\lambda) = \frac{(1 - R_\lambda)^2}{2R_\lambda} \qquad (2.1)$$

Where R_λ is simply the ratio of the light intensity of the sample divided by the reference at that wavelength.

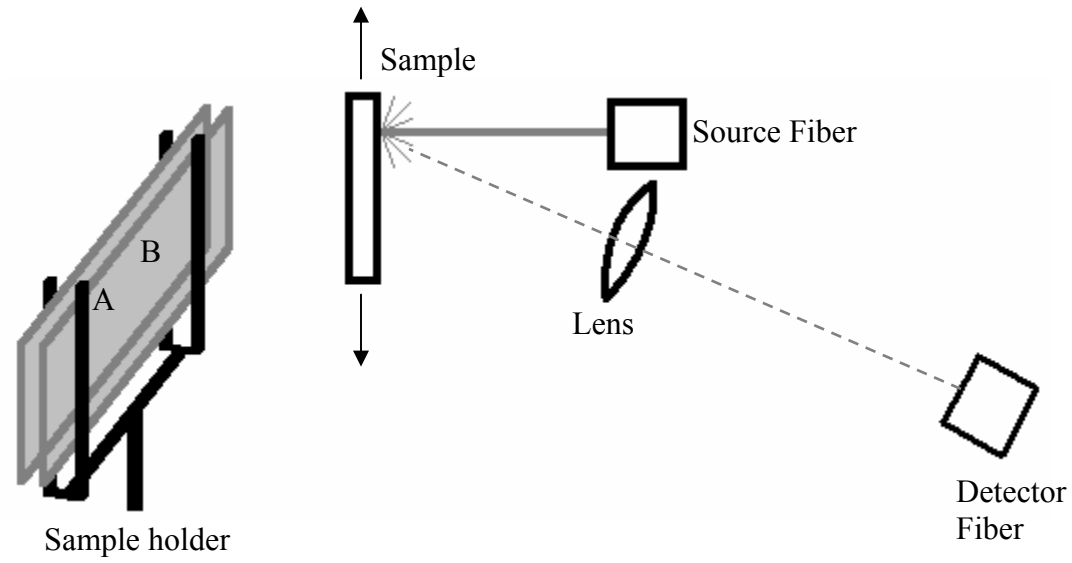

Figure 2.4: Sample holder depiction and layout for steady state diffuse reflectance measurements. The source light is focused onto the sample using only the lens on the fiber optic output of the DT 1000 light source. The distance from the source to the sample is 2.9 cm. The sample (A) and reference (B) are between two microscope slides that are exactly perpendicular to the source beam. The translation stage holding the sample is placed such that its movement is also exactly perpendicular to the source beam. A fused silica lens with a focal length of 3.5 cm is placed 4 cm away from the point at which the source hits the sample. The detector fiber is 13.3 cm from the lens. The angle between the source beam and input path into the lens and detector is ~30°.

2.2.4 Measurement of the CT Absorption Coefficient and Association Constant

The calculation of the CT epsilon and association constant for the pyrene:TCNQ complex in chloroform was performed with the Cary 50. For this experiment, a series of solutions containing the same amount of TCNQ and various amounts of pyrene were made and their absorption in a quartz cuvette measured. Since the CT absorption band does not overlap with that of the monomers, when the relative amount of complex formed is small, the following expression may be used:

$$\frac{Abs(\lambda_{CT})}{[Donor]_0[Acceptor]_0} = K\left(\varepsilon(\lambda_{CT}) - \frac{Abs(\lambda_{CT})}{[Acceptor]_0}\right) \qquad (2.2)$$

where $[Donor]_0$ and $[Acceptor]_0$ are the initial concentrations of the donor and acceptor and $Abs(\lambda_{CT})$ is the measured absorption at the CT band.[2] For a 1:1 complex, a Scatchard Plot of $\frac{Abs(\lambda_{CT})}{[Donor]_0[Acceptor]_0}$ versus $\frac{Abs(\lambda_{CT})}{[Acceptor]_0}$ results in a straight line. The slope is -*K*, the association constant, and the y-intercept is the absorption coefficient multiplied by the association constant, $K\varepsilon(\lambda_{CT})$. This experiment is fairly easy in terms of doing since it consists of just making solutions of various concentrations and taking absorption spectra. Use of a balance to record the mass of solutions and other quantities involved proved to be the most straightforward and reliable method of measurement, while also limiting evaporation and eliminating cross contamination. The Scatchard Plot is a recursive method and the chosen concentrations and quantities for the measurement are based on

doing the measurement a few times. Reliable values for the epsilon and association constant lie within a certain range of concentrations, this range cannot be computed until there is some idea of what the constants are. The amounts of donor and acceptor used here were based on previous experiments and literature. A TCNQ solution was prepared by addition of 3.8 mg of TCNQ to 50 mL of chloroform (delivered via a 50 mL volumetric flask) in an Erlenmeyer flask of known mass which was then re-massed giving a solution density of 1.475g/mL. Into 8 empty glass vials 12.2 - 404.8 mg of pyrene were added, then into each vial, 4.5 - 7.4 g of the TCNQ solution were added. The vials were capped tightly and given about 20 minutes for the contents to completely dissolve and equilibrate. Then the UV-Vis absorption was taken for each sample in a quartz cuvette. Care was taken to clean and dry the cuvette from sample to sample, and the least concentrated samples were measured first. The observed spectra, from low to high concentration, did not change, except in intensity and a very slight blueshift that was likely due to the extremely high concentration of pyrene in the last few solutions. Charge transfer compounds are not limited to 1:1 stoichiometries, hence the need to watch for spectral changes at high concentrations where other association constants, if present, will manifest themselves. The Scatchard plot will not be linear if there is more than one stiochiometry present (assuming the range of values tested is complete).

2.2.5 Fluorescence

Steady-state fluorescence spectra were collected with a Spex Fluorolog Tau-3 fluorescence spectrophotometer. The excitation wavelength used was typically chosen based on previous absorption measurements, or set to 400 nm to match the excitation wavelength typically used in fluorescence lifetime measurements on the laser system. Measurements were typically done in the front-face geometry so as to match with the laser system's geometry.

2.3 Time-resolved Spectroscopy Instrumentation

Time-resolved measurements were performed using two laser systems: a 40 kHz Spectra-Physics laser system and a 1 kHz Coherent Libra laser system. The layout and operating properties of each laser system as well as the optical layout of their associated laser tables will be discussed separately. Typically, time-resolved fluorescence experiments were performed on the 40 kHz Spectra-Physics laser system, while the 1 kHz Coherent Libra laser system was predominantly used for transient absorption experiments.

2.3.1 Spectra-Physics Laser System and Table Layout

The layout for the regeneratively amplified 40 kHz Spectra-Physics laser system is shown in Figure 2.5. This system uses a Spectra-Physics Millennia Vs continuous-wave diode laser operating at 3.31 W to pump a Kapteyn-Murnane Labs (KML) Ti:Sapphire oscillator. The oscillator produces an 800 nm laser pulse (91 MHz) with a typical power output of 250 - 300 mW (modelocked). The oscillator seeds the Spectra-Physics Spitfire amplifier which is pumped by a Spectra-Physics Merlin. The Merlin is a Q-switched Nd:YLF laser with an output of 6-8 W, operating at 40 kHz. The amplified 800 nm pulse out of the Spitfire has a typical power of 150-250 mW and a pulse width of 100 fs.

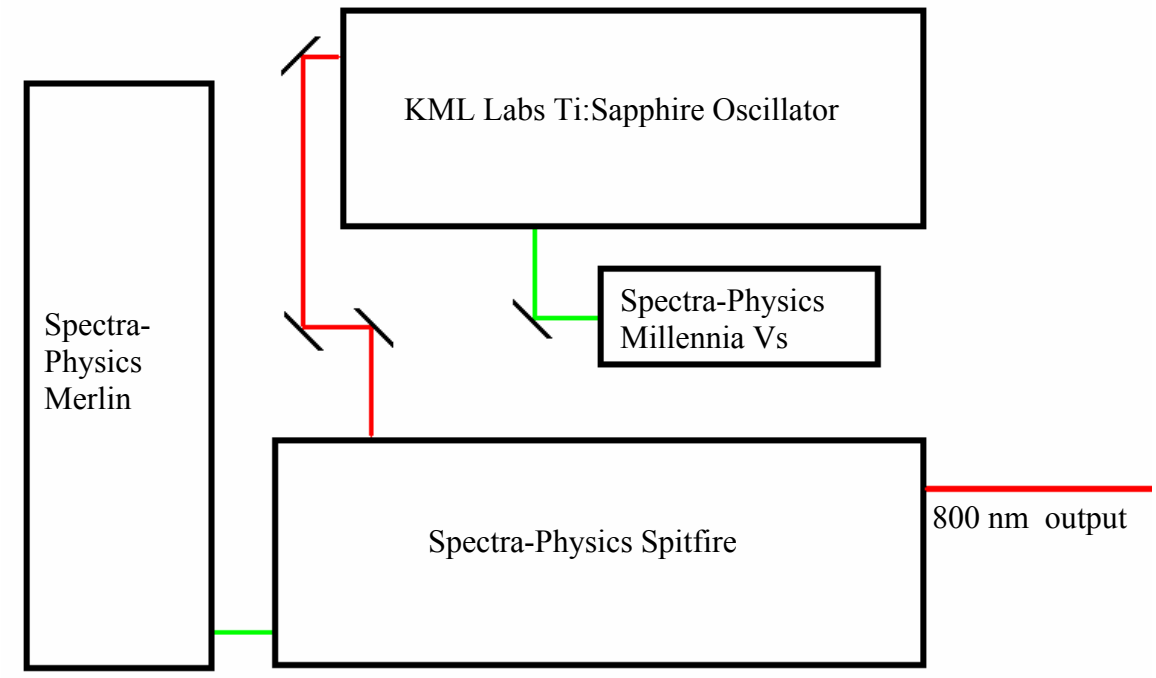

Figure 2.5: Layout of the Spectra-Physics 40 kHz laser system.

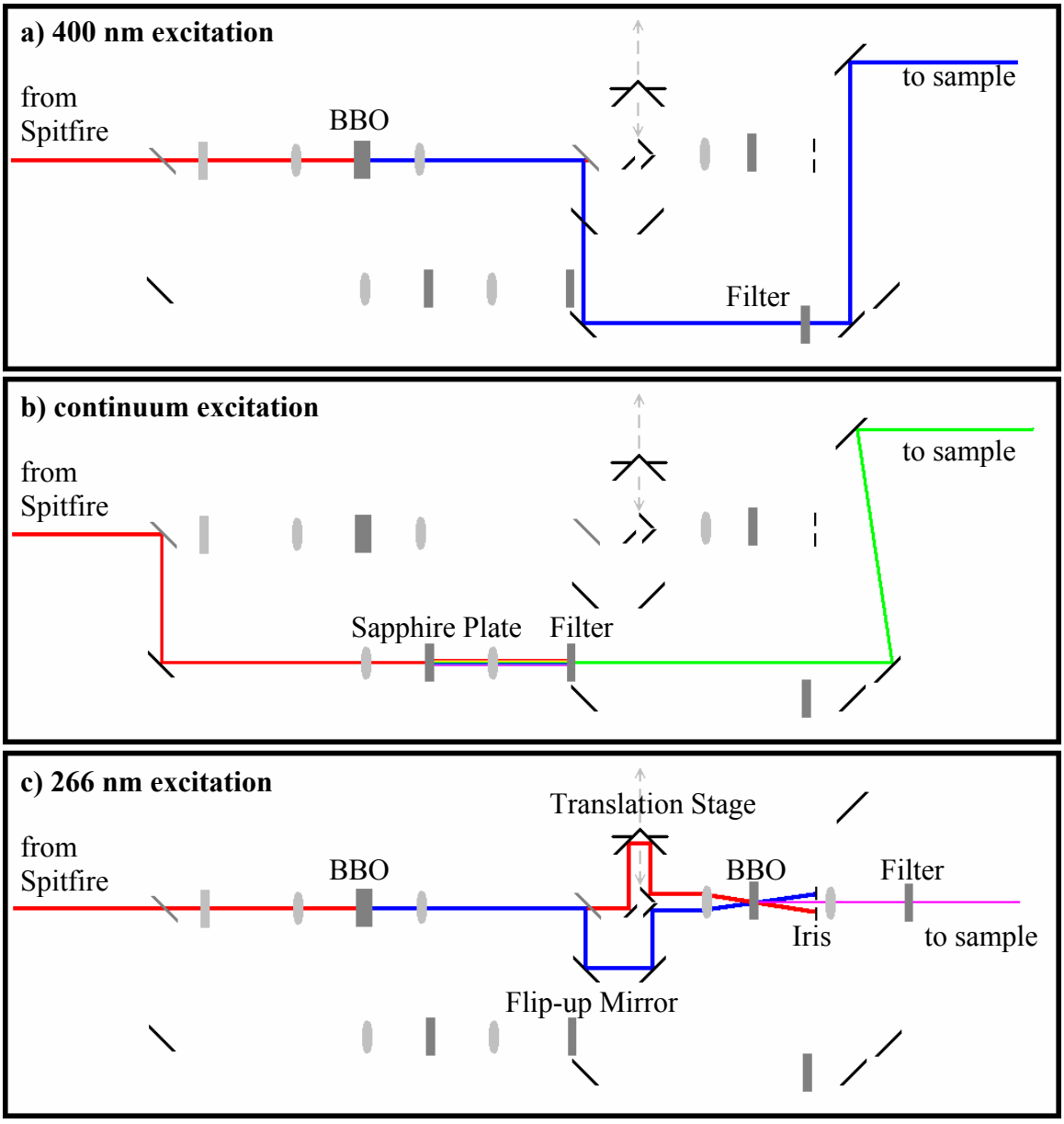

Figure 2.6: Layout of the laser table for the Spectra-Physics 40 kHz laser system showing the three beam paths for a) 400 nm, b) continuum, and c) 266 nm excitation.

For experiments on the 40 kHz laser system, there are three different beam paths, shown in Figure 2.6, allowing for the generation of multiple wavelengths. For 400 nm light, Figure 2.6a, the 800 nm fundamental is frequency doubled with a BBO to 400 nm. Residual 800 nm light is removed with a hot mirror and/or Schott Glass BG39 filters. For continuum generation, some of the 800 nm light is split off of the path to the BBO and instead focused onto a sapphire plate to generate a white light continuum. A bandpass filter may be placed right after the sapphire plate to select one desired wavelength. For 266 nm light, Figure 2.6c, the 800 nm beam is frequency doubled with the BBO to 400 nm, but is then mixed with residual 800 nm in a second BBO to generate the 266 nm beam. The first mirror after the first BBO is actually a dichroic mirror that reflects the 400 nm beam and transmits the 800 nm beam. A flip-up mirror is used to change the 400 nm beam path, that directs it to the second BBO instead of directly to the sample. A short delay stage on the 800 nm beam path is used to ensure the two beams hit the second BBO simultaneously. After the 266 nm beam is generated, an iris and a 266 nm bandpass filter are used to remove the residual 400 and 800 nm beams.

The benefit of this system is that the alignment for each of the three beam paths does not change, and switching from one to another requires minimal work (i.e. moving the flip-up mirror up or down). The laser table is configured such that the choice of beam(s) can be sent over to the fluorescence detection setup or to a transient absorption setup. Another important aspect of the setup is that the continuum can be generated simultaneously with the 400 or 266 nm beam, which is necessary for transient absorption where two beams are involved.

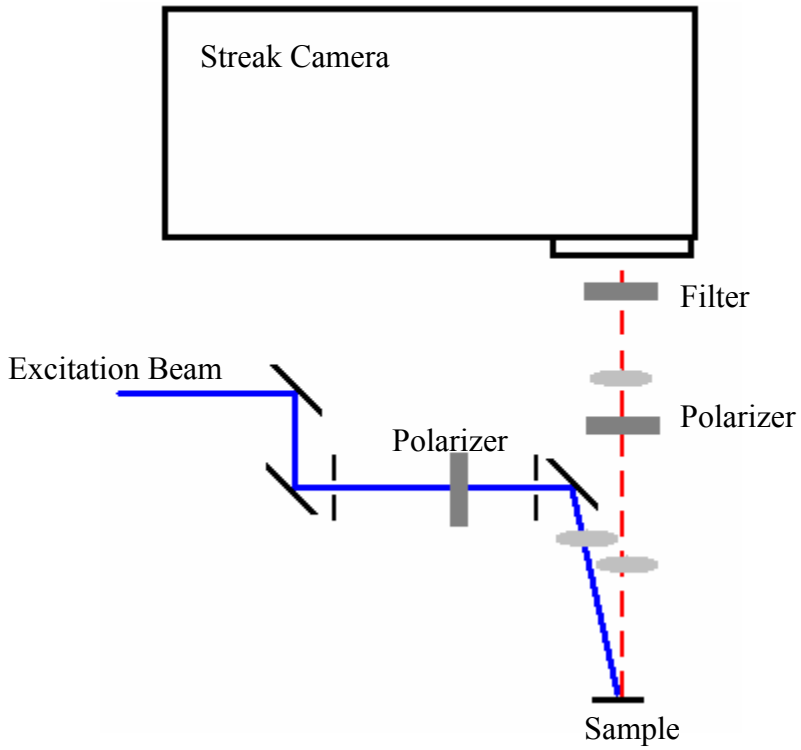

Figure 2.7: Fluorescence detection layout for the Spectra-Physics 40 kHz laser system. A similar setup was erected on the Libra system except that the sample and signal were at a right angle to the camera aperture and a so an extra mirror was necessary to input into it (the geometry was still front-face excitation/detection).

Figure 2.7 shows the fluorescence detection setup. The input excitation beam is aligned through two irises with the first two mirrors shown in the diagram, and focuses on the sample. The fluorescence from the sample is collected with a lens and directed into a Hamamatsu C4334 streak camera detector. A pair of polarizers, one on the pump and one on the signal can be used for magic angle (54.7º) signal detection. An appropriate optical filter on the fluorescent signal is also necessary to remove scattered excitation pulse.

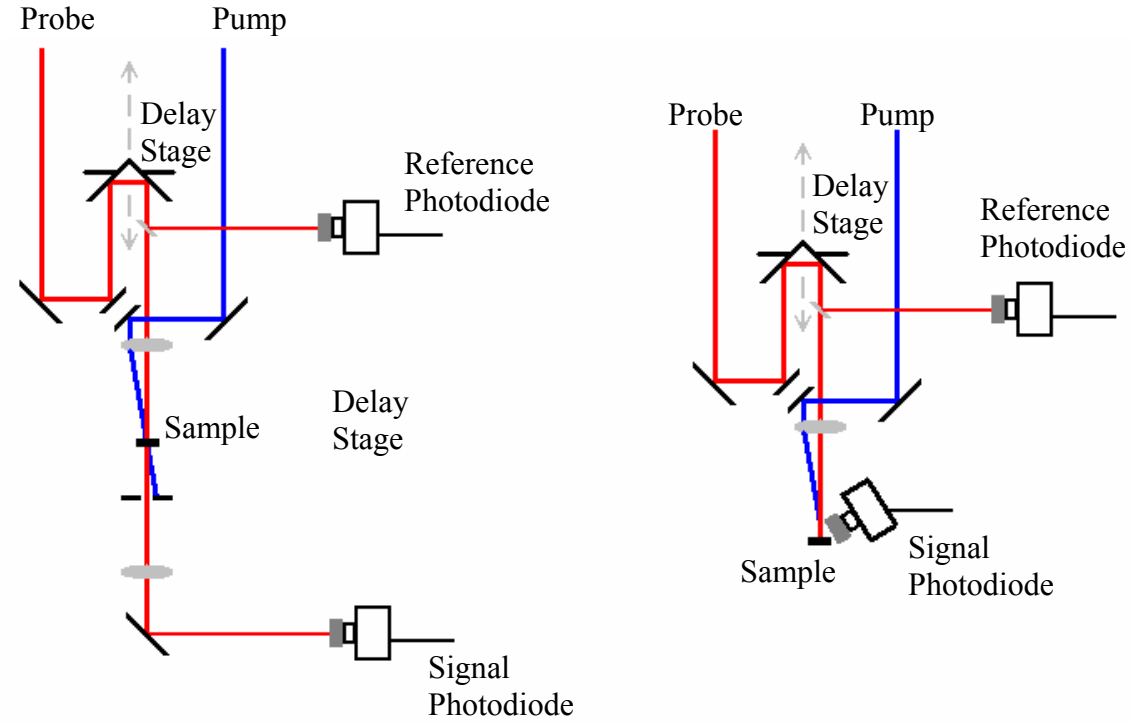

Figure 2.8: Transient absorption setups for the 40 kHz laser system. The setup to the left is the traditional transmission setup where the probe goes through the sample. On the right is the setup for diffuse reflectance, where the probe hits an opaque scattering sample, and the scatter is collected.

Figure 2.8 shows the two setups used for transient absorption. The layouts are nearly identical except the geometry right at the sample. Two input beams are necessary, the pump (usually 400 nm, see Figure 2.6a) and the probe (usually sapphire generated continuum, see Figure 2.6b) are generated simultaneously and directed over to the transient absorption setup. The path length each beam has to travel is roughly the same, such that the laser pulses arrive at the sample at nearly the same time. A retroreflector mounted on a computer controlled 5 cm translation stage (Aerotech Unidex 511) was used to change the path length of the probe beam, permitting it to arrive before or after

the pump. Exiting the retroreflector, the probe beam passes through a beamsplitter, and is then focused onto the sample with a lens. The purpose of the above mentioned beamsplitter is to direct a small portion to a second photodiode so that noise in the beam can be subtracted from the signal. The pump is also directed through the same lens to the sample, but it is intentionally off centered so that it arrives at the sample at an angle. For a traditional transmission setup, the pump and probe go through the sample. The probe is re-collimated with a lens and directed into a photodiode, while the pump comes in at an angle and is mostly filtered out by an iris on the other side of the sample. For diffuse reflectance pump probe, the pump and probe beam hit the sample and scatter in all directions. For this setup, optimal signal was achieved by simply having the detecting photodiode right next to the sample. In each case, more so for diffuse reflectance, appropriate filters were put on the photodiodes to block the pump beam. A Stanford Research Systems Model SR830 DSP Lock-In Amplifier was used to process the signal, the probe beam was chopped at 150 Hz. The delay stage and lock-in amplifier were controlled with a computer using LabVIEW software.

2.3.3 Coherent Libra Laser System and Table Layout

The 1 kHz Coherent Libra laser system essentially uses the same types of lasers as the Spectra-Physics system, but is an all-in-one system where the oscillator, pump, and regen amplifier are integrated and housed together. It is also significantly more powerful than the aged Spectra-Physics system. The Vitesse oscillator is used as the seed and is pumped by a diode laser (Verdi). The typical Verdi power is 4.14 W at 18 A; the output

power of the Vitesse is typically about 885 mW (modelocked). The Evolution pump laser operates at 20.6 A, and the overall output of the system is 3.8 W at 1 kHz, 800 nm.

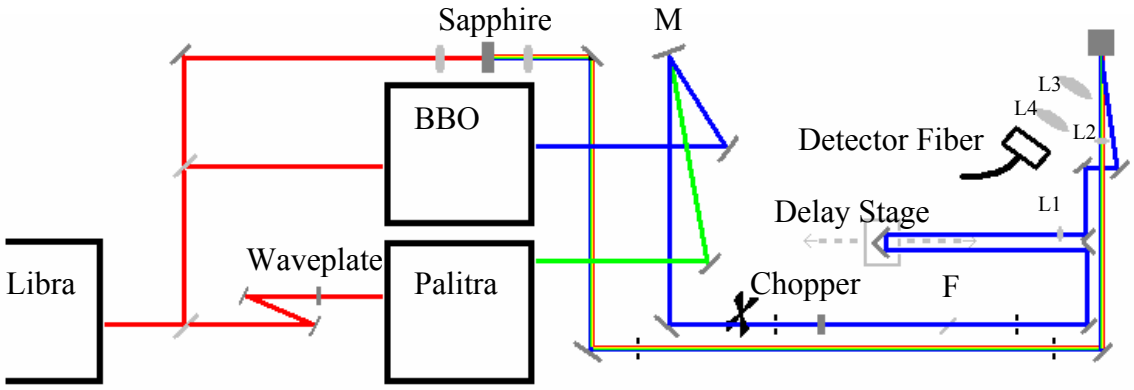

Figure 2.9: Layout for the Libra laser system.

Shown in Figure 2.9, the output of the Libra is split into three parts with beamsplitters, and there is sufficient power for each option to function simultaneously. Just like the Spectra-Physics system, there are paths for continuum generation and 400 nm pump generation with a BBO. The third beam path goes through a waveplate to a Quantronix Palitra FS optical parametric amplifier (OPA), which is described in detail below. The OPA permits the conversion of the 800 nm fundamental into a beam of any wavelength from 270 nm to 1600 nm.

In terms of experimental configurations, the Libra is primarily used for diffuse reflectance transient absorption experiments using either the 400 nm output from the BBO or the Palitra as the pump and sapphire continuum as the probe. An important aspect of this setup is that the output from the BBO and the Palitra both go to the same mirror, marked "M" in Figure 2.9. This is not to imply both are used simultaneously, but that only a very minor adjustment is required to switch between the two. In this manner, the timing of the sapphire probe and the pump beam, whether it is from the BBO or the Palitra, is kept the same. The Libra system uses an Ultrafast Systems Helios transient absorption setup with a 0.5 m Newport delay stage and an Ocean Optics S2000 detector. Just after the delay stage, the pump beam is focused with lens L1, and then directed at the sample. The pump lens used is a 50 cm focal length fused silica lens, however the sample position is actually about 65.5 cm from the lens. As the power of the laser system is quite high, it is more desirable to have a large laser spot than one small intense spot. Lens L2, is a 20 cm focal length lens that is used to focus the probe onto the sample (the sample is at the focus). The scattered probe is collected with a 3.5 cm focal length fused silica lens, L3, and then coupled into the fiber optic cable to the detector with a 10 cm lens, L4.

As transient absorption can yield results with positive and negative signal (absorption and bleaching for example), one important experimental practice is to check the pump alignment by scanning the delay stage and monitoring the position of the beam. This is done by the insertion of a mirror into the pump beam after the delay stage (typically near L2) and using this mirror to put a laser spot on a piece of paper taped to the wall (with due caution it stays parallel to the laser table - and that no one else is

around to get it in their eyes!). With the delay at ~5 ps, a pencil tracing of the spot is done on the paper. Then, the delay stage is set to move to ~1500 ps, and the laser operator watches the spot on the wall as the motorized stage moves. The position of the laser spot should not move. In the event that the spot moves, the pump alignment through the irises should be rechecked/redone. The asymmetric laser spot generated by the Palitra, coupled with the use of wavelengths the human eye cannot see, makes it particularly problematic in regard to alignment into the delay stage. Failure to ensure proper pump alignment results in an artificial change in signal intensity as the pump beam can "walk" off the probe beam as the delay is changed. This is further complicated by the focusing of the continuum probe, the different wavelengths do not necessarily focus the same way, thus it is possible for one spectral region to be completely normal while other wavelengths report anomalous decay kinetics.

Besides the laser system, the sample holder for diffuse reflectance transient absorption is also important. Figure 2.10 depicts the custom built sample holder used for performing diffuse reflectance transient absorption experiments. The holder consists of a small baseplate with a few cylindrical skids held in place by being squeezed between some rectangular blocks (Figure 2.10a). The powder samples for diffuse reflectance are kept in special glass vials with flat bottoms (cuvettes may also be used). Shown in Figure 2.10b, the vial is laid flat on the skids and held in place with copper wire (not shown). In this manner, samples can easily be swapped in and out relatively quickly, and there is no risk for cross contamination. The vials may be sealed with a rubber septum, and scans can be conducted under weak vacuum.

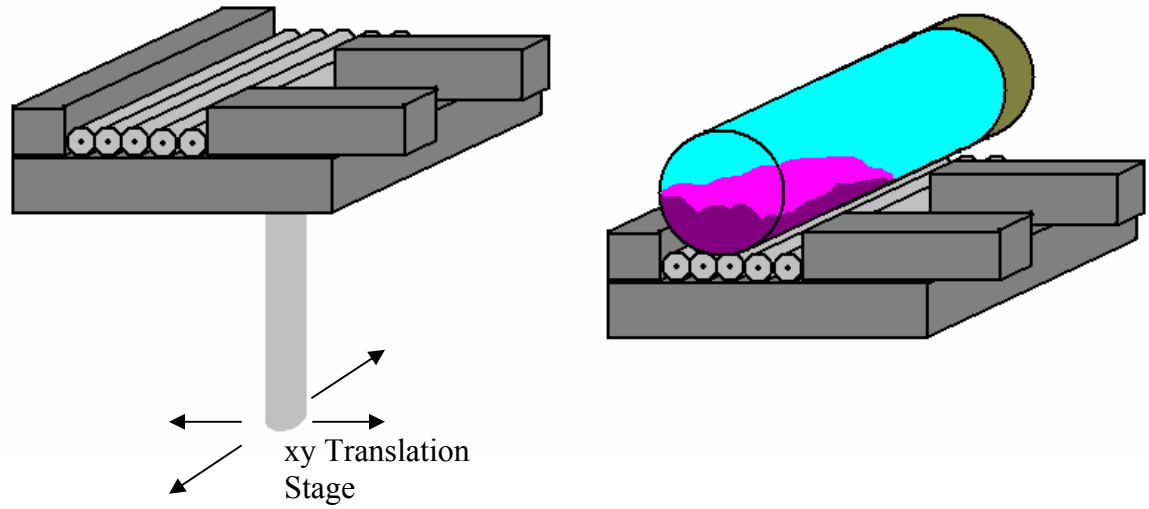

Figure 2.10: Sample holder for diffuse reflectance transient absorption.

The sample holder rests on a xy translation stage which is also very important for alignment during diffuse reflectance transient absorption experiments. Seen in Figure 2.9, the collection lens L3 is at angle to the probe beam. The distance of the sample from the probe focusing lens, L2, has to be exactly the same for every sample, or the angle will change and the scattered probe signal will not be collected. Instead of a burden, this is actually a blessing. Using the Helios software to actively show the probe signal (CCD Scope, see Figure 2.11), the operator simply has to move the sample forwards or backwards with the translation stage to maximize the continuum signal. The added bonus is that not only does this reproduce the sample position, but in doing so also preserves to overlap of the pump beam with the probe. This assumes that sample to sample the

scattering properties are the same, which is generally valid for similar samples (i.e. a series of compounds that use same optical dilutant $BaSO_4$, etc).

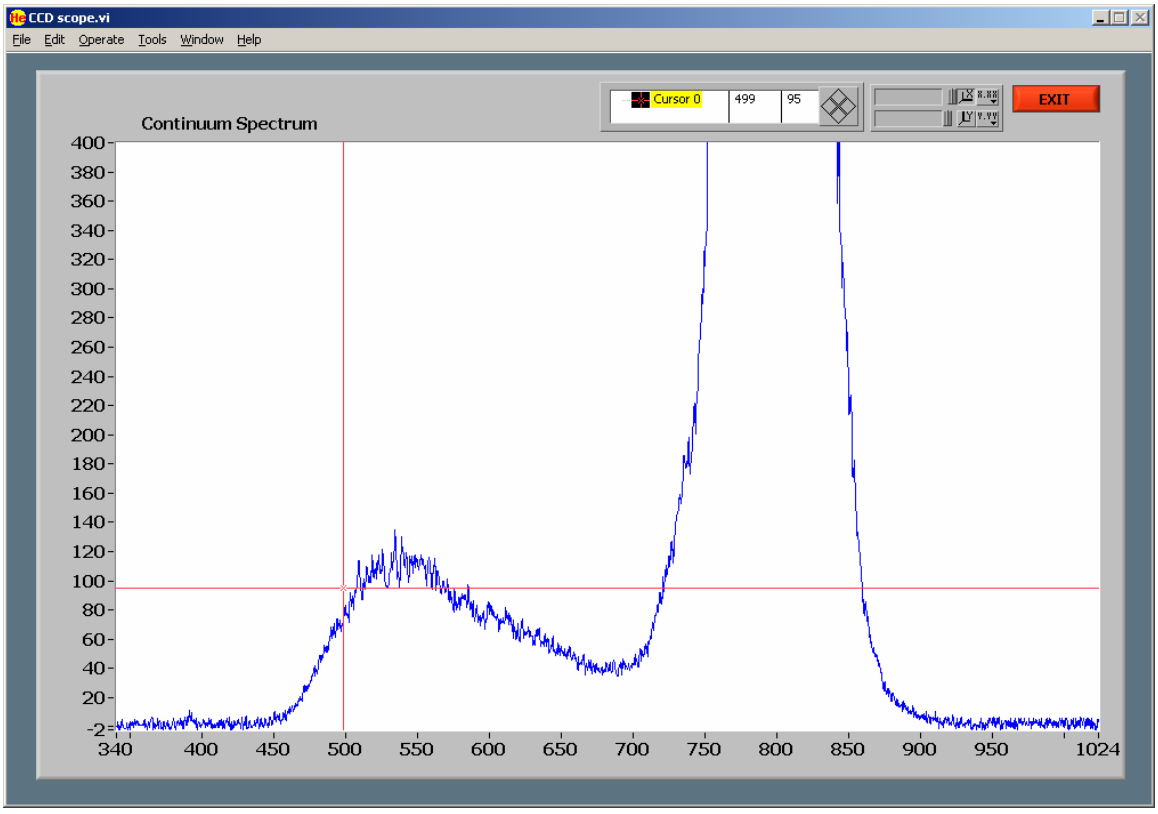

Figure 2.11: Screenshot of the CCD Scope function in the Helios transient absorption software. This spectrum is the continuum probe signal scattered off of one of the $Au@TiO_2$ samples described in chapter 5. The detector maximum is 4000 counts, as shown here, the signal is not very strong, in part because this particular sample strongly absorbs visible light. The best data for these experiments was measured around 800 nm, where, as shown here, the probe signal is the strongest. The user can then compare the noisy kinetics at the shorter wavelengths with those at 800 nm, to see if they appear to be the same. Use of the CCD Scope enables the operator to quickly change samples, as one simply needs to move the sample into the correct position to maximize the signal.

The signal levels for diffuse reflectance pump probe are generally low, the differential absorption being about 10^{-3} at most. In the Helios software, the maximum integration time per data point is 10 seconds. For diffuse reflectance transient absorption experiments, the maximum integration time is almost always necessary. If a sample

undergoes simultaneous rapid and long-lived decay kinetics, one useful feature of the Helios software is the ability to take more or less data points for certain periods of time. The following scheme of time durations and step sizes was developed during the research done in chapter 5: Begin scan 7 ps before T_0 (the time on the delay stage when pump and probe pulses overlap temporily). 1) Scan 1 ps in 0.1 ps steps. 2) Scan 4 ps in 0.5 ps steps. 3) Scan 10 ps in 0.1 ps steps, 4) Scan 100 ps in 2ps steps. Scan 1420 ps in 20 ps steps. 5) End scan at 1536 ps, taking 0.1 ps steps to the end. This scheme starts be establishing a good baseline by taking 10 tiny steps at the very beginning. Then it skips ahead to when the signal is about to start and takes tiny steps for the next 10 ps. Then the scan step sizes and ranges get progressively bigger. Small step sizes are for the most part only useful at the beginning of the scan, when rapid processes are occurring, once these are done, large step sizes should be taken. The exception to this rule is at the very end, where this scheme scans the last picosecond in 0.1 ps steps; this is to establish a good endpoint. Often it is worthwhile to compare the spectrum of the sample at different points in time, and to do so it is necessary to average a few data points together to get spectra that aren't debilitatingly noisy.

The Libra system is also sometimes used for fluorescence lifetime experiments, but only rarely so as it requires removal of the streak camera from the other laser system. When fluorescence experiments are performed, a mirror is inserted into the pump beam at point "F" in Figure 2.9, that beams the laser over to a fluorescence setup similar to that of Figure 2.7.

2.3.5 Palitra FS Optical Parametric Amplifier

The Quantronix Palitra FS optical parametric amplifier is a versatile tool for spectroscopy experiments. Originally installed on a Quantronix Integra laser system, the Palitra FS had to be realigned and reconfigured to work on the Coherent Libra system. The stability, power, shorter pulse duration, and large uniform laser mode of the Libra seem to benefit the Palitra greatly. While loss of 10% power on the Integra resulted in loss of function of the Palitra, the Libra does not suffer such problems. The Palitra FS used by the Bardeen lab is actually one of the first ones built by Quantronix, who subsequently changed its design slightly. There is currently no literature on the correct operation of this model. Because of this and the necessary reconfiguration to work on the Libra system, along with the technical information here, Appendix I contains detailed information on the operation and troubleshooting of the instrument.

Optical parametric amplification in the Palitra is done using a relatively new nonlinear crystal, BiBO (BiB_3O_6). The Palitra contains two BiBO crystals that provide two stages of amplification. Optical parametric amplification is essentially a wave-mixing process, governed by the conservation of energy and phase-matching in the crystal. For amplification, two input beams propagate through the nonlinear crystal at a certain angle generating third beam. The pump beam, ω_1, plus the weak seed beam, ω_2, combine to generate a third beam ω_3, where $\omega_3 = \omega_1 + \omega_2$. The created beam, known as the idler, is essentially discarded, while the seed beam, ω_2, also known as the signal, is greatly amplified in the process. Shown below, this process occurs twice in the Palitra where the amplified output of the first crystal is used to seed the second crystal.

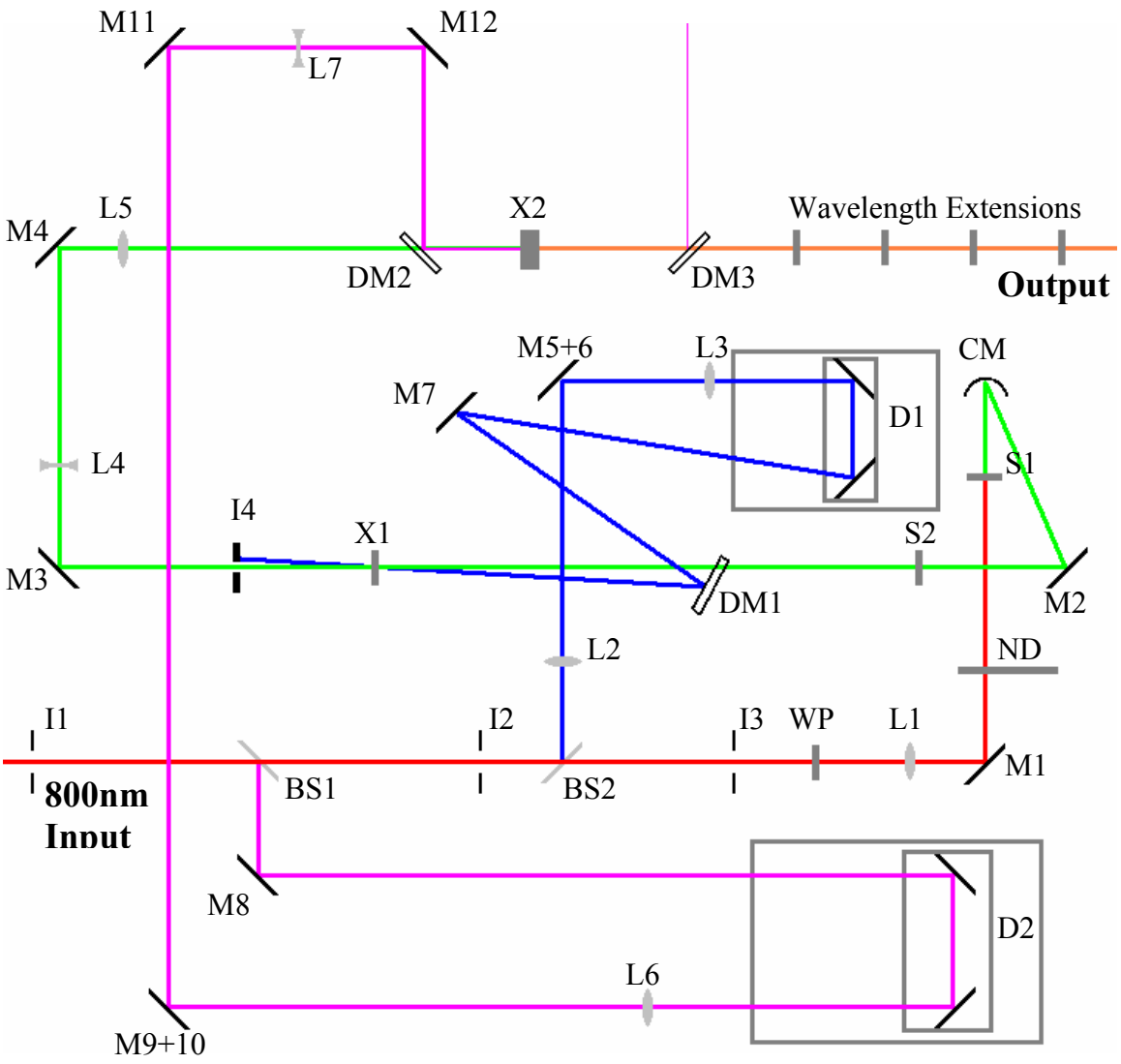

Figure 2.12: Optical layout of the Palitra FS OPA. Key: I - iris, M - mirror, BS - beamsplitter, WP - waveplate, L - lens, ND - graduated neutral density slide, S1 - sapphire, CM - curved mirror, S2 - stretcher, X - BiBO crystal, DM - dichroic mirror, D - delay stage. Beam color key: 800 nm input - red, continuum - green, 800 nm 2nd stage pump - purple, 800 nm 1st stage pump - blue, output - orange. Some mirrors are labeled with two numbers (ex. "M5+6") where in the operational manual there are two mirrors, but only one is present in this version of the Palitra.

The layout of the Palitra is shown in Figure 2.12. The 800 nm fundamental from the Libra enters the unit at I1. Irises I1 and I3 are intended to be used in aligning the input into the unit, I2 is off center and intended to be used only for attenuation purposes. The input beam passes through two beamsplitters, BS1 and BS2, which divide the laser into three parts: 2nd stage pump, 1st stage pump, and continuum. The continuum beam path is composed of the remaining 800 nm input that passes through both beamsplitters. It passes through a waveplate and then is attenuated by a graduated ND slide. It is reflected off of a curved mirror and continuum is generated in the sapphire at S1. The continuum then travels through a stretcher (S2) and through the back of dichroic mirror 1 (DM1) and into the BiBO crystal at X1. The 1st stage pump is also directed at X1, its beam path begins at BS2, it is directed into delay stage 1 (D1), and then eventually on to X1 with DM1. By using a dichroic mirror that the continuum can transmit through, the angle between the 1st stage pump and the continuum beam is small. M5+6 is named so to avoid confusion with the operational manual which is based on a later Palitra version that has two mirrors instead of one. The pump is spatially overlapped onto the continuum beam at X1, and the timing of the pulses is controlled by changing D1, making the 1st stage pump beam path longer or shorter. The white light continuum seed is amplified by the 1st stage pump at X1 and continues on through an aperture (I4), the 1st stage pump is blocked by this aperture. M3 and M4 are then used to direct the amplified continuum through another dichroic mirror (DM2) on to the second crystal X2, and then out of the unit. It is important to note that M3 and M4 are gold mirrors that may be damaged if the 1st stage pump is permitted to pass through I4. Similar to what occurs at X1, now the amplified

continuum serves as the seed for optical parametric amplification at the second BiBO crystal X2, where it is overlapped with the 2nd stage pump. The 2nd stage pump's beam path begins at BS1; compared to the 1st stage pump and continuum beams, the 2nd stage pump is significantly more powerful. M12 and DM2 are used to direct the beam onto X2 and overlap it with the amplified continuum at X2 AND after it. The second stage of amplification differs from the first in this respect, that the pump and continuum are parallel and on top of each other spatially while delay stage 2 (D2) is used to adjust the temporal overlap. The final amplified signal generated in X2 is then sent through DM3 and through the various wavelength extension crystals that produce the desired wavelength through frequency doubling. The purpose of DM3 is to remove leftover 2nd stage pump, but sometimes it is removed for generation of certain wavelengths (Vis3 and UV3). The position of the delay stages, D1 and D2, as well as the angles of X1, X2, and the wavelength extension crystals are computer controlled with Quantronix Palitra Commander software.

2.4 Specific Experimental Conditions for the Time-resolved Experiments

2.4.1 TCNB Complexes

Laser experiments described in chapter 3 on the TCNB complexes were performed exclusively on the 40 kHz Spectra-Physics system. The samples were kept under vacuum in a Janus ST-100 cryostat. For fluorescence and transient absorption, a 400 nm pump was used. Two Schott Glass OG 420's and a 450 nm long-wave-pass were used to filter the pump from the signal. For fluorescence, the typical per-pulse fluence

was controlled with neutral density filters and was 0.2 μJ/cm^2 or less. For experiments to intentionally bleach the sample, to compare the before/after decay kinetics, the samples were scanned, subjected to a 60 s exposure to a 500 μJ/cm^2 pump pulse, and then rescanned. The experiments to determine the bleaching cross-section and process were done in a similar manner where the samples were exposed to 180 s of pump radiation of different intensities (from 3.8 μJ/cm^2 to 530 μJ/cm^2) with low power scans performed before and after. For transient absorption, the lowest feasible pump fluence was 260 μJ/cm^2. After preparation and alignment, the sample would be moved so the beam hit a fresh spot on the sample and the first scan was kept. Subsequent scans exhibited laser damage by the presence of a new fast decay in the decay kinetics.

2.4.2 Pyrene:TCNQ

Experiments performed on pyrene:TCNQ in chapter 4 were performed on both laser systems. The fluorescence experiments were done on the 40 kHz in much the same way as the TCNB complexes except the typical per-pulse fluence was 3 μJ/cm^2 or less and an additional filter, an OG 570, was used along with the OG 420's and the 450 nm long-wave-pass filters. Fluorescence from the pyrene:TCNQ complex was observed around 840 nm; because the streak camera uses a grating, the extra filter was included to prevent any short wavelength radiation, either from pump scatter or monomer fluorescence, from entering the detector and falsely appearing as double its original wavelength. The temperature dependence was also done in the Janus ST-100 cryostat, using liquid He and a Lakeshore 321 temperature controller. Transient absorption

experiments were performed on the 1kHz Libra using a 400 nm pump (from the BBO) and sapphire generated continuum. The pump fluence was 6 $\mu J/cm^2$.

2.4.3 TiO_2

Experiments performed on the TiO_2 samples in chapter 5 were done on both systems. Fluorescence experiments with 266 nm excitation were done on the Spectra-Physics system, while 300, 350, and 430 nm excitation were done with the Libra using the Palitra. The per-pulse fluence for 266, 300, 350, and 430 nm excitation was 1, 7, 6, and 7 $\mu J/cm^2$ respectively. The samples were packed into a pitted copper sample holder that could be stored in the ST-100 cryostat. For 266 nm excitation, the pump pulse was filtered out from the detector with two glass plates. For 300 and 350 nm excitation, a Schott Glass UG 11 filter was used to remove other wavelengths from the excitation pulse, and a 400 long-wave pass and a Schott Glass OG 420 color filter were placed in front of the detector to filter out the scattered excitation light. For 430 nm excitation, a 500 nm short-wave pass filter and a Schott Glass BG39 filter were used to filter the excitation pulse, and two Schott Glass OG 435 filters were used in front of the detector. Transient absorption measurements were performed on the Libra system with a 300 nm pump pulse generated with by the Palitra and white light continuum probe. The pump pulse fluence was 1 $\mu J/cm^2$ and the peak differential absorbance signals were 10^{-3} or lower.

References

1. Joo, J. B.; Zhang, Q.; Lee, I.; Dahl, M.; Zaera, F.; Yin, Y. *Advanced Functional Materials* **2011**, *22*, 166–174.

2. Deranleau, D. A. J. Am. Chem. Soc. 1969, 91, 4044-4049.

Chapter 3: The effects of photochemical and mechanical damage on the excited state dynamics of charge-transfer molecular crystals composed of tetracyanobenzene and aromatic donor molecules

3.1 Introduction

The existence of low energy charge-transfer (CT) electronic states in donor-acceptor complexes makes these useful systems for studying how molecular interactions can affect electron-hole delocalization and transfer rates.[1] Molecular donor-acceptor cocrystals are chemically simple and structurally well-defined, making them ideal systems to study CT phenomena.[2] Technological applications may result from the ability to grow such crystals into different shapes, for example nanorods.[3] McConnell et al. showed that all CT crystals could be grouped into two broad classes: ionic ground state CT, where the ground state involves an electron that has already been transferred, and nonionic ground state, where an electron transfer occurs only after absorption of a photon provides sufficient energy.[4] Both types of CT crystals have been the subject of extensive research interest. Ionic CT crystals or CT salts can function as organic conductors and even superconductors. Nonionic CT crystals are neutral in their ground state but undergo excited state photoinduced electron transfer reactions. Several groups have studied the timescale of charge separation in nonionic CT crystal systems, with the general conclusion that the CT state is populated within a few hundred femtoseconds after excitation of the neutral state.[5-7] The separated charges recombine when they relax back to the ground state, providing a second opportunity to study electron transfer dynamics. The recombination of charge separated states in solution complexes has been extensively studied[8-11], but there is much less data on recombination in CT crystals. In this context,

previous work by Kochi and coworkers was especially intriguing.[12] Using transient absorption spectroscopy on powdered samples, they found that the CT excited state relaxation in a variety of TCNB:donor complexes proceeded via two channels: recombination to the ground state and dissociation into free carriers. Both processes were complete within a few hundred picoseconds in the crystals studied. The yield of carrier dissociation was significant in all cases, and approached 50% for some crystals. This high yield of dissociated charges, coupled with reports of high photoconductivity in appropriately structured CT crystals[13-14], suggested to us that CT crystals might be able to function as highly ordered analogs of the bulk heterojunction structures commonly used to achieve high efficiency photovoltaics.[15] It is possible to generate CT crystals with absorptions extending into the near infrared, and thus these materials might constitute a molecular crystal alternative to polymer-based bulk heterojunction photovoltaic materials.

In this chapter we have re-examined a subset of the TCNB compound originally studied in reference 12 in order to better understand the origins of the efficient charge dissociation. In all compounds, we found that the CT fluorescence survived for nanoseconds, much longer than the lifetimes derived from the earlier transient absorption experiments. By doing careful power dependence measurements and comparing single crystal and powdered samples, we have determined that this class of CT crystals is highly susceptible to both mechanical and photochemical damage. Both types of damage resulted in more rapid excited state relaxation dynamics as measured by both fluorescence and transient absorption (TA) decays. We see no evidence of rapid

dissociation of the CT electron-hole pair, and the dynamics appeared to be consistent with the traditional picture of a relatively tightly-bound electron-hole pair that decays slowly back to the ground state. We do see a similar trend of recombination rate with charge transfer energy (E_{CT}) as seen in reference 12, but with measured recombination rates that are now 1-2 orders of magnitude slower. Our work does not rule out the formation of other types of long-lived states like triplets or dissociated charge carriers, but their formation rates must be relatively slow in order to be consistent with the nanosecond fluorescence lifetimes. These systems are thus quite different from the polymer bulk heterojunction systems, where dissociation into free carriers occurs on femtosecond to picosecond timescales.[16]

3.2 Results and Discussion

3.2.1 Steady-state Spectra

The steady-state emission spectra for the five CT molecular crystals studied in this work, along with the donor molecular structures, are shown in Figure 3.1. All the emission spectra have broad, featureless lineshapes. The phenanthrene crystal exhibited a pronounced shoulder at shorter wavelengths, indicating the presence of a second emitting state. The fluorescence spectra of powdered samples of these compounds were very similar to those of the single crystals shown in Figure 3.1. For all cases, the fluorescence could be easily observed in the solid state, in contrast to the analogous donor-acceptor complexes in solution, where the non-rigid environment permits rapid internal conversion and recombination to the ground state. [20]

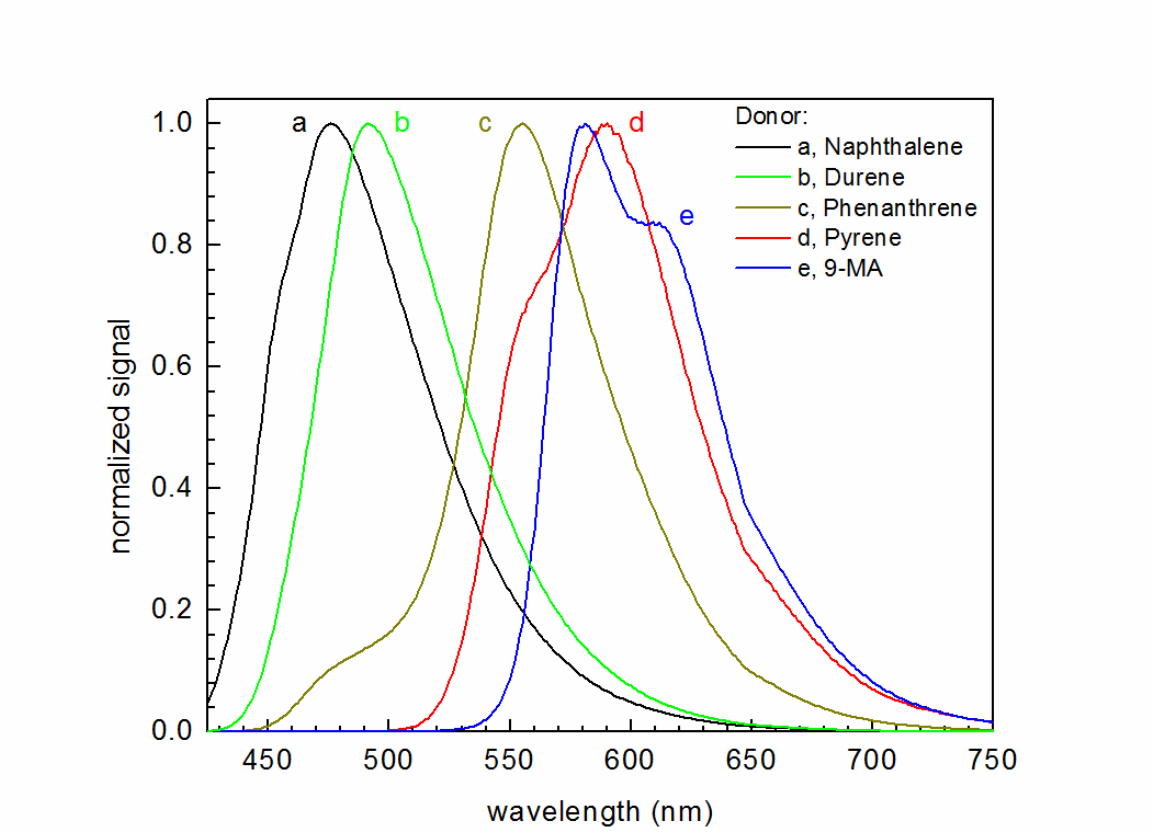

Figure 3.1. Normalized steady state fluorescence spectra of TCNB CT crystals. The excitation source was set to 400 nm for all compounds to match the laser excitation source used in the time-resolved fluorescence experiments.

3.2.2 Time-resolved Fluorescence

The strong steady-state fluorescence indicated a reasonably long fluorescence lifetime, and that is exactly what was observed for all five CT complexes in the solid state. For the single crystals, the fluorescence lifetimes extended well into the nanosecond regime, as shown in Figure 3.2 and in Table 3.1a. Note that the fluorescence decays plotted in Figures 3.2 and 3.3 are for data taken at the peak wavelength of the emission. For all compounds the fluorescence lifetime varied slightly with detection wavelength, and for this reason we report fluorescence decay times for two representative

wavelengths in the Table 3.1. In four of these compounds, this variation did not result in a qualitative change in spectral shape, leading us to conclude that the nature of the electronic state is the same, but due to heterogeneity in the crystal, different energy sites experience slightly different relaxation times. The exception was TCNB:phenanthrene, where we observed a clear multiexponential decay indicative of energy relaxation between two emissive states. This compound has an initially excited emission at 508 nm that decayed on a 1.7 ns timescale while the emission at 556 nm grew in on the same timescale and then persisted for tens of nanoseconds. Our measured fluorescence lifetimes are reasonably consistent with those reported earlier in the literature. TCNB:naphthalene crystals are the most extensively studied and have reported fluorescence lifetimes ranging from 17 ns to 21 ns[21-23], which is exactly the range we measure depending on the detection wavelength. TCNB:durene has a reported lifetime of 34 ns[24], as compared to 46-48 ns in Table 3.1a. The largest discrepancy is for TCNB:pyrene, where the fluorescence lifetime has been reported as 31.5 ns[22], considerably longer than the 14-16 ns reported in Table 3.1a. The variation in fluorescence lifetimes for these CT crystals may reflect their sensitivity to preparation conditions, as discussed below. All the decays summarized in Table 3.1a were measured using a very low laser fluence of 2×10^{-7} J/cm^2 per pulse or less.

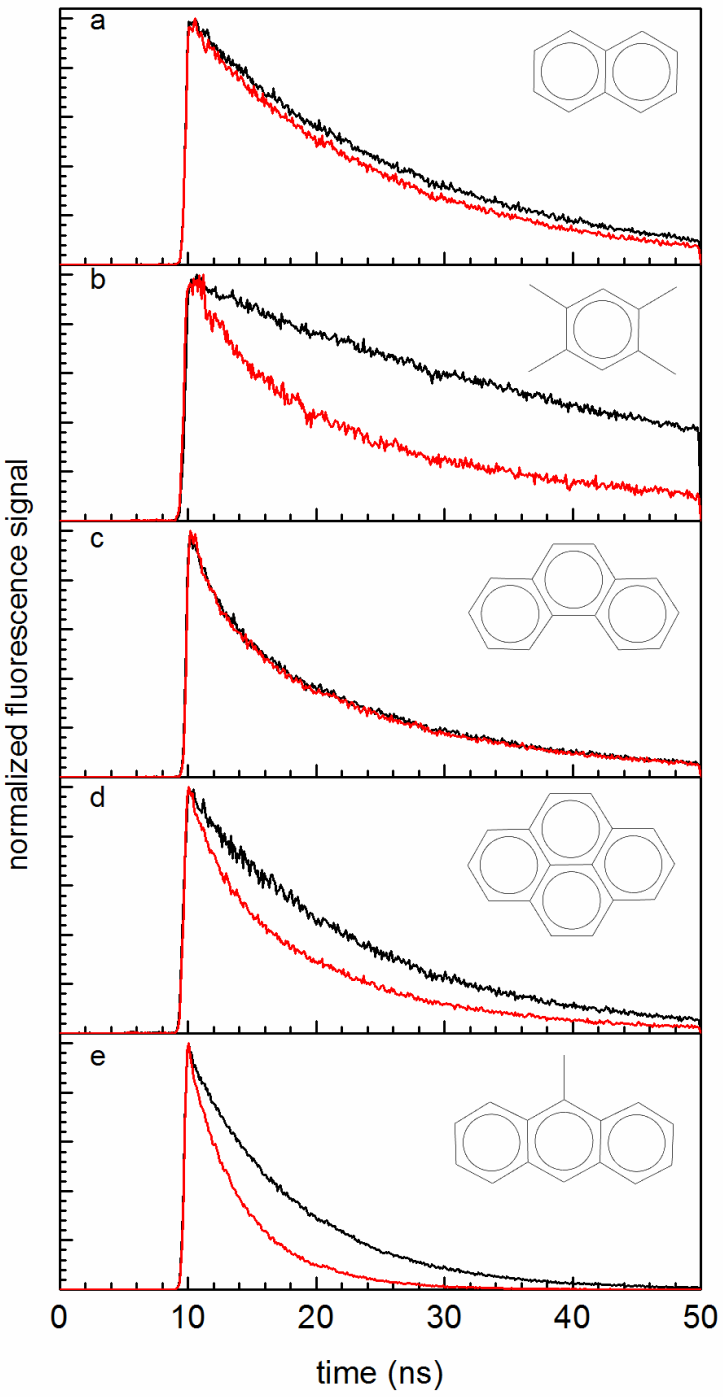

Figure 3.2. Normalized time-resolved fluorescence decays of TCNB CT single crystals before and after (in red) a 60 second laser exposure of 500 μJ/cm^2. Donors: (a) naphthalene, (b) durene, (c) phenanthrene, (d) pyrene, (e) 9-MA.

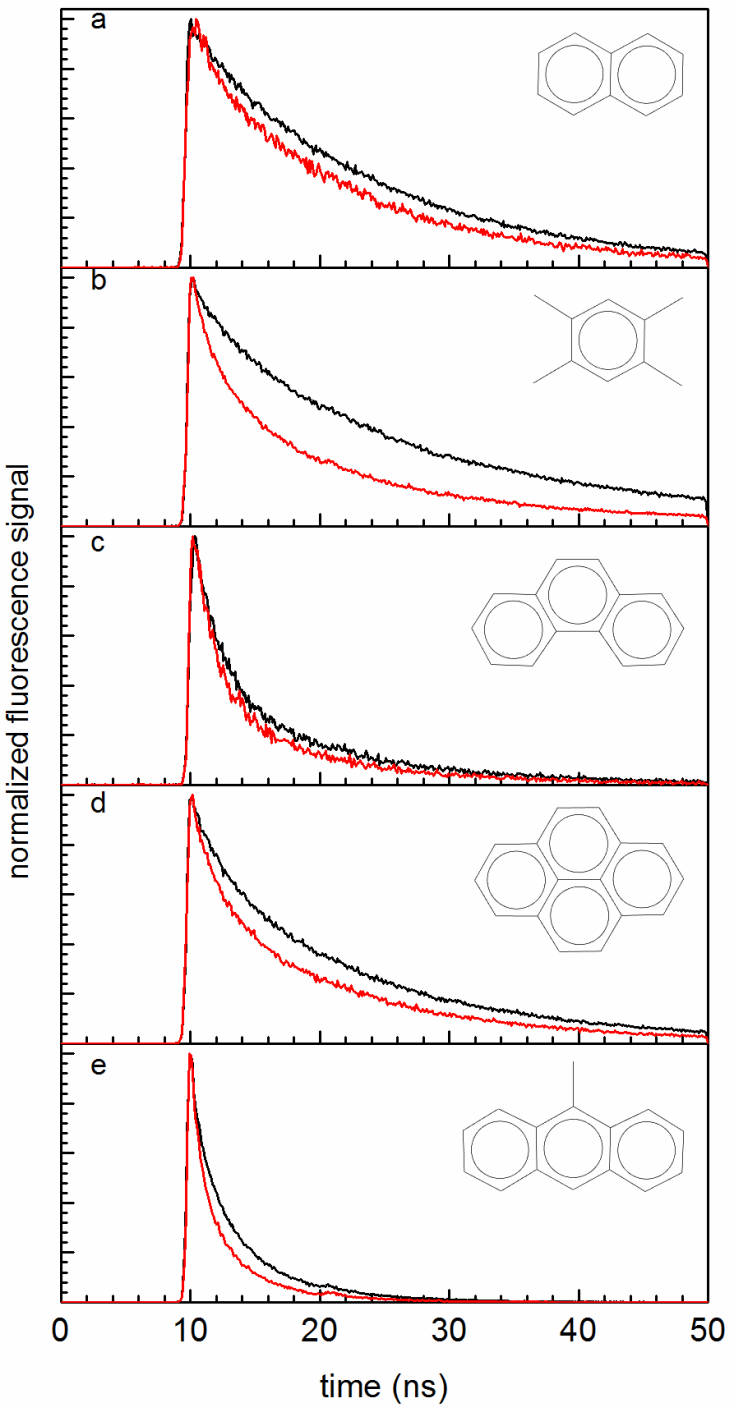

Figure 3.3. Normalized time-resolved fluorescence decays of dilute pulverized TCNB CT crystals in $BaSO_4$ powder before and after (in red) a 60 second laser exposure of 500 μJ/cm^2. Donors: (a) naphthalene, (b) durene, (c) phenanthrene, (d) pyrene, (e) 9-MA.

Table 3.1a: Fluorescence lifetimes of TCNB CT Single Crystals.

Donor	λ_{fl} (nm)	τ_1 (ns)	τ_2 (ns)	a_1	a_2
Naphthalene	476	17.3 ± 0.5	-	1	-
	555	21.1 ± 0.5	-	1	-
Durene	492	48.1 ± 0.5	-	1	-
	570	46.5 ± 0.5	-	1	-
Phenanthrene	508	1.7 ± 0.2	14.8 ± 0..5	0.38	0.62
	556	1.8 ± 0.2	34.5 ± 0.5	-0.72	1.72
Pyrene	590	13.6 ± 0.5	-	1	-
	640	15.5 ± 0.5	-	1	-
9-MA	582	8.3 ± 0.2	-	1	-
	674	7.8 ± 0.3	-	1	-

Table 3.1b: Fluorescence lifetimes of TCNB CT Powders in $BaSO_4$:

Donor	λ_{fl} (nm)	τ_1 (ns)	τ_2 (ns)	a_1	a_2
Naphthalene	459	14.1 ± 0.3	-	1	-
	591	34 ± 1	-	1	-
Durene	480	2.0 ± 0.2	18.7 ± 0.3	0.149	0.85
	582	25.4 ± 0.3	-	1	-
Phenanthrene	473	1.5 ± 0.1	9.4 ± 0.1	0.67	0.33
	550	1.2 ± 0.2	30.3 ± 0.2	-0.51	1.51
Pyrene	564	1.5 ± 0.1	13.4 ± .3	0.29	0.71
	664	19.5 ± 0.1	-	1	-
9-MA	595	0.6 ± 0.1	4.1 ± 0.3	0.527	0.473
	681	0.6 ± 0.1	4.5 ± 0.3	0.23	0.770

The tabulated lifetimes above include the peak fluorescence and the fluorescence of their respective shoulders in the red (with the exception of TCNB:phenanthrene which peaked in the red). The calculated lifetimes were determined by integrating over a ±5 nm range for each given wavelength. The decays were fit to a function of the form $a_1 \exp[t/\tau_1] + a_2 \exp[t/\tau_2]$.

3.2.3 Decay Kinetics Are Sensitive to Photo and Mechanical Damage

After exposure to higher fluences, we noticed that the fluorescence signals decreased and the decays became more rapid, especially for the durene, pyrene and 9-methylanthracene (9-MA) crystals. The normalized fluorescence decays after a total laser dose of 1200 J/cm^2 (i.e. 5x10^{-4} J/cm^2 per pulse at 40 kHz over a 60 s period)

exhibited a significant increase in the fluorescence decay rates, and these damage-induced decays are overlaid with the original signals in Figure 3.2. The change in lifetime depended on the crystal: TCNB:naphthalene's decay was only about 15% faster, while for durene and 9-MA the decay was almost twice as rapid in the powder as compared to the single crystal. The fluorescence decays of the powdered samples before and after laser exposure are shown in Figure 3.3, while the decay parameters at different wavelengths are summarized in Table 3.1b. The same photo-induced acceleration of the fluorescence decay was observed for the powdered samples, with the main difference being that the initial decay rates were now much faster than in the single crystals, presumably as a result of damage during the mechanical grinding process. Note that the powder decays tended to be more rapid and possessed a pronounced biexponential character at most wavelengths. The susceptibility of the TCNB CT crystals to photodamage was much more pronounced than in other molecular crystal systems that we have studied. For example, a perylene single crystal exposed to the same laser dose showed no measurable photobleaching or change in fluorescence decay rate.

3.2.4 Quantifying the Photodamage Process with Fluorescence

Clearly, the CT crystals are vulnerable to damage, both via mechanical milling and via prolonged exposure to light. These two types of damage appear to act through different mechanisms. For example, mechanical grinding had a large effect on the decay of TCNB:phenanthrene, but this solid was largely unaffected by laser exposure, as seen by comparing the fluorescence decays in Figures 2c and 3c. Quantifying the amount of

damage as a function of mechanical stress is difficult due to the uncontrolled nature of the grinding process.

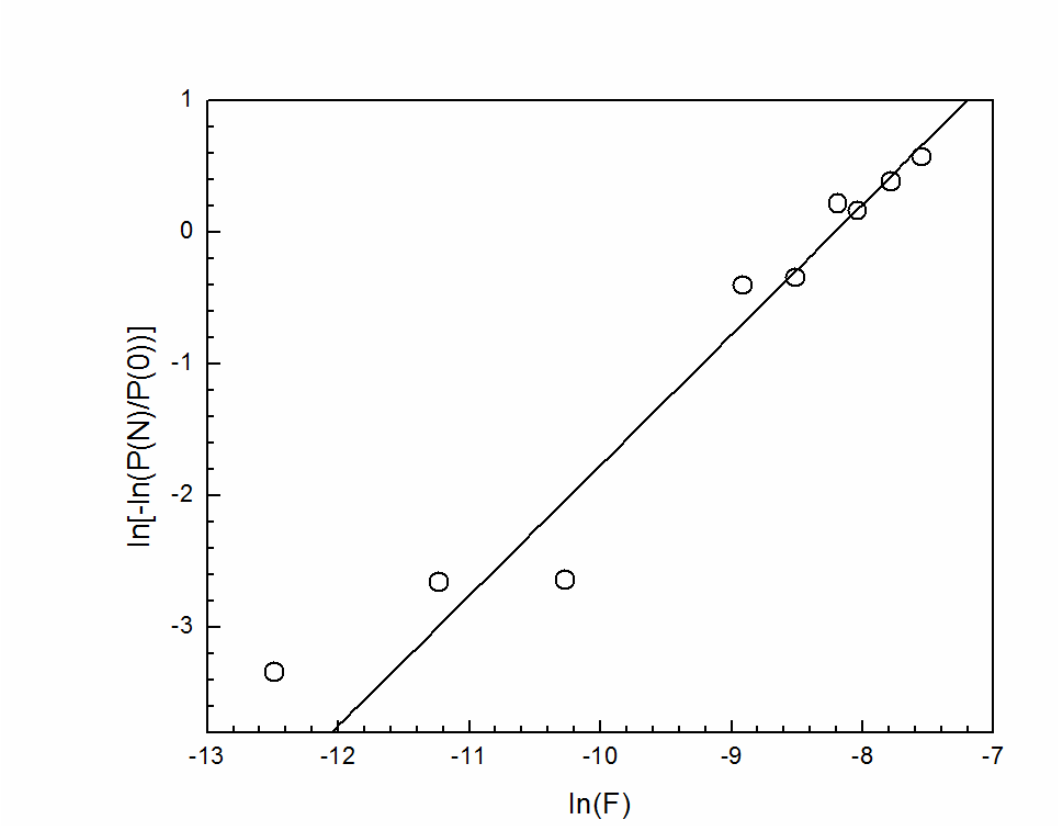

Figure 3.4. Log-log plot of normalized fluorescence signal, $P(N)/P(0)$, vs. laser fluence, F, for TCNB:9-MA in $BaSO_4$ powder. Each data point is the result from a fresh spot on the sample, where its total integrated fluorescent signal was measured twice, before and after photodamage at a fixed fluence and time duration. Using these results in equation 1, the calculated slope was 0.99 ± 0.09, indicating that the photobleaching of the sample occurred via a single photon process.

Quantifying the amount of photodamage is more straightforward since one can precisely control the laser exposure. There are different aspects of laser damage: changes in fluorescence lifetime and changes in the total amount of fluorescence signal. We first examined the decrease in total fluorescence signal, or photobleaching.

Following the treatment of Kao et al.[25], we find that the fluorescence signal P decays after N pulses according to

$$P(N) = P(0)\exp\left[-\beta\left(\frac{F}{h\nu}\right)^{M} N\right] \tag{3.1}$$

where $h\nu$ is the pulse energy, F is the pulse energy per unit area, and β is the bleaching cross section. From equation (3.1) we see that a plot of ln[-ln[$P(N)/P(0)$]] versus ln(F) should yield a straight line with slope M giving the multiphoton power law. In Figure 3.4, a log-log plot of the bleach fraction versus the accumulated fluence for TCNB:9-MA yielded a slope M = 0.99±0.09, indicating that the photobleaching proceeds through a single photon process with M=1. For TCNB:naphthalene, we could also extract β=4.1x10^{-22} cm^2 from this plot. The ratio of β to the absorption cross section σ_{abs} gives the photobleaching yield Φ_{bleach} [25],

$$\Phi_{bleach} = \frac{\beta}{\sigma_{abs}} \tag{3.2}$$

Using equation (3.2) and the value σ_{abs}=9.2x10^{-18} cm^2 for the absorption cross section at 400 nm [21], we find Φ_{bleach}=4.4x10^{-5} for this CT crystal in powder form. We observed similar single photon bleaching behavior for the four other compounds in this study, all with Φ_{bleach} values of approximately 10^{-4} to 10^{-5}. Typical organic dyes have Φ_{bleach} =10^{-6} or less in solution[25-26], so this value is surprisingly high for a polycrystalline sample under vacuum. We also observed that while the integrated fluorescence signal was bleaching, the fluorescence decay rate was also becoming more rapid. The biexponential decays are fit to the function $a_1 \mathbf{exp}[t/\tau_1] + a_2 \mathbf{exp}[t/\tau_2]$ and Figure 3.5a shows the

change in the average fluorescence decay time τ_{avg} for TCNB:9-methylanthracene powder, defined as

$$\tau_{avg} = \frac{a_1\tau_1 + a_2\tau_2}{a_1 + a_2} \tag{3.3}$$

For comparison, the decrease in the total fluorescence signal, $P(N)/P(0)$ is shown in Figure 3.5b for this compound. From Figure 3.5, it can be seen that the decrease in fluorescence decay time and the decrease in total fluorescence signal parallel each other. It is important to note, however, that τ_{avg} decreased only ~20%, while the total fluorescence decreased by ~80%. The large decrease in total fluorescence signal thus cannot be due solely to the observed decrease in τ_{avg}. But the data in Figure 3.5 strongly suggest that both changes are manifestations of the same damage process.

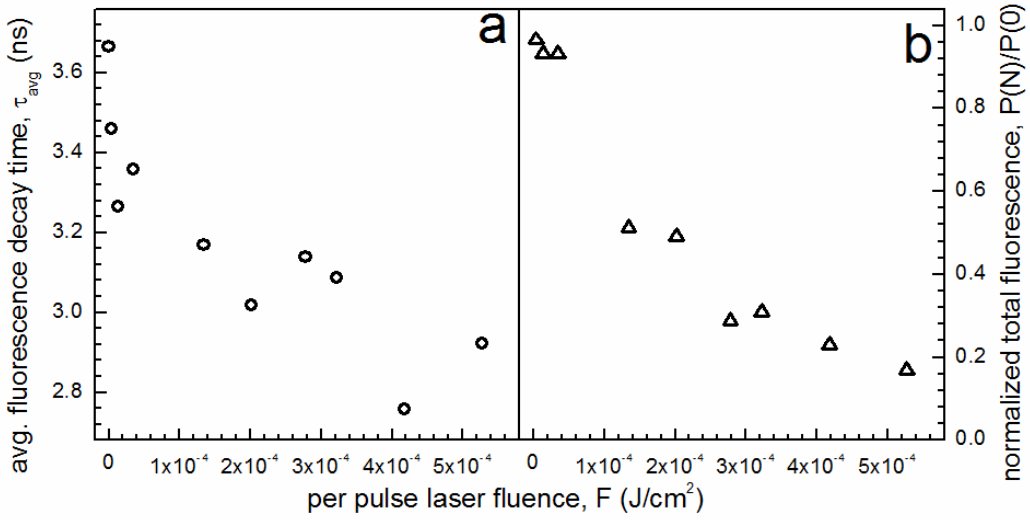

Figure 3.5. (a) Average fluorescence decay time, τ_{avg}, defined by equation 3, and (b) normalized total fluorescence signal, $P(N)/P(0)$ versus the per pulse laser fluence for TCNB:9-MA. The total exposure to this per pulse fluence was, at a repetition rate of 40 kHz, for 180 s. The shortening of the decay time and the fluorescence signal bleaching exhibit a similar dependence on the pulse fluence F.

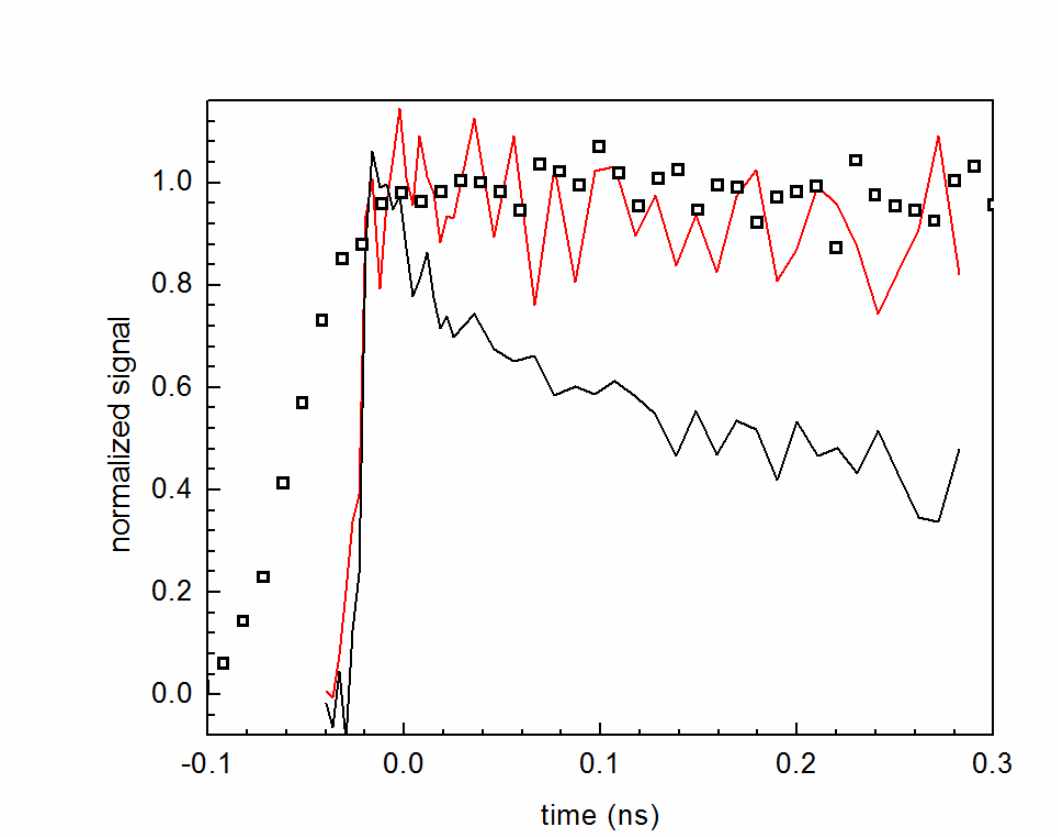

Figure 3.6. Normalized time-resolved fluorescence signal (□),and transient absorption (ΔR/R) for unexposed sample (red), and after exposure to a total fluence of 1.4×10^{5} J/cm^2 (black), of TCNB:naphthalene in $BaSO_4$ powder. Like the fluorescence, transient absorption measurements of a fresh sample exhibited only a slow decay. Note that the lowest feasible fluence for the TA experiments was 2.6×10^{-4} J/cm^2, whereas the fluorescence measurements were done at a laser pulse fluence of 2×10^{-7} J/cm^2 or lower.

3.2.5 Transient Absorption Decay Kinetics are Sensitive to Photodamage

At even higher laser fluence levels, we have found that the TCNB:naphthalene transient absorption kinetics can be affected by photodamage as well. Figure 3.6 shows the pump-probe kinetics for a 400 nm excitation pulse followed by a 700 nm probe pulse. 700 nm is close to the peak of the naphthalene radical cation absorption, and this spectral region was also monitored in reference 12 to measure the disappearance of the CT

species due to recombination. Due to the low absorption coefficients of these compounds (typically ~1000 $M^{-1}cm^{-1}$ or less), relatively high pump pulse fluences were required to obtain reasonable pump-probe signal levels. At a pump pulse fluence of $2.6x10^{-4}$ J/cm^2, the highest fluence where no obvious damage occurs during a scan of the pump-probe delay, the peak $\Delta R/R$ signal was on the order of $2.7x10^{-4}$. This signal was a factor of 1000 lower than that detected in reference 12. Figure 3.6 shows that at this fluence level, the 700 nm induced absorption appeared within the time resolution of the experiment (200 fs) and showed no decay over the next 300 ps. This signal is overlaid with the fluorescence decay obtained from the streak camera measurements in Figure 3.6. When the pump pulse fluence was increased to $9.4x10^{-4}$ J/cm^2, where the $\Delta R/R$ signal level was on the order of 10^{-3}, the signal developed a second decay component on the order of 100 ps. This more rapid decay persisted even when the experiment was repeated on the same sample spot with lower pump power. Shown in Figure 3.6 is the TA decay measured using the pump pulse fluence of $2.6x10^{-4}$ J/cm^2 after the sample had been subjected to a total fluence of $1.4x10^5$ J/cm^2 over the period of ~ 1 hour. This dose was considerably higher than what was used in the fluorescence photodamage experiments, and now the damage-induced decay has moved into the subnanosecond range. The lifetime obtained from the TA decay in Figure 3.5 was 120 ps, about a factor of 2 shorter than that observed in reference 12 for the same compound. This difference may be due to a difference in laser exposure conditions, but since parameters like laser spot size and pulse energy were not reported in reference 12, we cannot be certain that this is the case. We also have not surveyed other TCNB complexes to see if they exhibit the same trend of

damage-induced decays in their TA spectra, although since they all showed similar sensitivities in their fluorescence decays, it is likely that photodamage can affect their TA response dynamics as well.

3.2.6 Discussion

Our results indicate that the TCNB CT solids are highly susceptible to damage, both due to mechanical and photochemical processes. This may be a byproduct of the bicomponent nature of the crystals, since it may be easier to produce defects when one component can be displaced from the lattice due to heating or a chemical reaction. In some sense, the CT crystal is only as strong as its weakest link, which in this case is probably the low molecular weight TCNB. One measure of the weak TCNB-donor packing forces is the significant orientational disorder in TCNB:naphthalene crystals at room temperature, as measured by both x-ray diffraction[27] and by Raman spectroscopy.[28] Similar disorder has also been observed in other TCNB:donor molecular crystals.[29-30] Presumably this orientational disorder could also create sites with different energies and decay times, which would help explain the wavelength-dependent decays of the fluorescence spectra. For higher molecular weight acceptors, like tetracyanoquinodimethane (TCNQ), it is possible that the lattice would be more resistant to disruption. Preliminary studies in our group on both the photoluminescence and TA of TCNQ:pyrene have show this compound to be less sensitive to grinding and laser exposure than TCNB:pyrene. A second possible origin of the damage susceptibility of

these crystals is the nature of the CT excited state itself, which may be more prone to side reactions than a neutral excited state.

Given the sensitivity of the TCNB CT complexes to preparation conditions like grinding, as well as to experimental conditions like laser exposure, it becomes a difficult question as to how to determine the true charge recombination time. The analysis of this recombination time in terms of electron transfer theory was the main result of reference 12. Clearly, the most straightforward systems to analyze are the pristine single crystals under low laser irradiance. As shown in Table 3.1a, four of the five compounds exhibited a single exponential decay at all wavelengths, on the order of 10 ns or longer. TCNB:phenanthrene appears to have an initial state that relaxes to the longer-lived CT state within a few nanoseconds. The ultimate charge recombination back to the ground state is likely reflected by the longest fluorescence lifetime in the single crystals. If we neglect intersystem crossing and charge dissociation into free carriers, we are left with only the internal conversion and radiative recombination mechanisms. In reference 12 it was assumed that the nonradiative electron transfer pathway was dominant. Given the much longer excited state lifetimes deduced in the current work, the neglect of the radiative pathway may no longer be justified. Nevertheless, if we follow reference 12 and assume that the recombination electron transfer rate k_{recomb} depends on the energy difference E_{CT} between the CT and neutral state, we find a similar trend as in the earlier work, albeit for a smaller set of compounds. Of course, our recombination rates are a factor of 100 smaller than those reported in reference 12. Given that our decay rates only vary by a factor of 6 for this set of compounds, it would be premature to try to extract any

definite relation between the recombination rate and E_{CT}. To do this would require a survey of a larger number of donor molecules. We simply point out that our limited data do not contradict the electron transfer theory used in reference 12 to analyze its results.

3.3 Conclusions

Our results on CT crystals of various donors complexed with TCNB indicate that caution must be used when studying their photophysical properties. First, these solids can have multiple excited states and complicated, multi-exponential decay dynamics. Second, both mechanical stress and light exposure can cause various relaxation processes to become more rapid, as well as reducing signal intensity through a high yield photobleaching process. In general, the kinetic parameters of a TCNB CT molecular crystal sample will depend on its preparation conditions and laser exposure history, and its sensitivity to these parameters will depend on its molecular composition. The samples that provided the simplest decay dynamics and consistent results were pristine single crystals, and it is recommended that results obtained on powdered samples be compared to single crystal results whenever possible. To measure transient absorption data, it may be that liquid suspensions of nanocrystals[31-32] are superior to stationary powders in order to prevent damage effects. From the standpoint of the photodynamics of these compounds, our results are consistent with the picture of long-lived, Coulombically bound states that undergo relatively slow charge recombination. The one compound that did exhibit a relatively rapid (1.8 ns) fluorescence decay clearly involved relaxation to a lower energy emissive state and not charge dissociation into free carriers.

We find no evidence for the rapid dissociation channel inferred by Kochi and coworkers in reference 12 and ascribe the picoseconds dynamics observed in that work to unintentional photodamage. This class of CT crystals may provide a good testbed for theories of electron transfer and bound CT states, but probably is not a good analog for bulk heterojunction systems where full charge separation takes place with close to 100% efficiency.

References

1. Kochi, J. K., Charge-transfer excitation of molecular complexes in organic and organometallic chemistry. *Pure Appl. Chem.* **1991,** *63*, 255-264.

2. Wright, J. D., *Molecular Crystals*. 2nd ed.; Cambridge U. Press: Cambridge, 1995.

3. Al-Kaysi, R. O.; Muller, A. M.; Frisbee, R. J.; Bardeen, C. J., Formation of cocrystal nanorods by solid-state reaction of tetracyanobenzene in 9-methylanthracene molecular crystal nanorods. *Cryst. Growth Des.* **2009,** *9*, 1780-1785.

4. McConnell, H. H.; Hoffman, B. M.; Metzger, R. M., Charge transfer in molecular crystals. *Proc. Nat. Acad. Sci.* **1965,** *53*, 46-50.

5. Fukazawa, N.; Fukamura, H.; Masuhara, H.; Prochorow, J., A picosecond diffuse reflectance laser photolysis study on phenanthrene-pyromellitic dianhydride charge-transfer crystal. *Chem. Phys. Lett.* **1994,** *220*, 461-466.

6. Asahi, T.; Matsuo, Y.; Masuhara, H., Localization of a charge transfer excited state in molecular crystals: a direct confirmation by femtosecond diffuse reflectance spectroscopy. *Chem. Phys. Lett.* **1996,** *256*, 525-530.

7. Asahi, T.; Matsuo, Y.; Masuhara, H.; Koshima, H., Electronic structure and dynamics of the excited state in CT microcrystals as revealed by femtosecond diffuse reflectance spectroscopy. *J. Phys. Chem. A* **1997,** *101*, 612-616.

8. Ojima, S.; Miyasaka, H.; Mataga, N., Femtosecond-picosecond laser photolysis studies on the dynamics of excited charge-transfer complexes in solution. 3. Dissociation into free ions and charge recombination decay from the ion pair state formed by charge separation in the excited state of 1,2,4,5-tetracyanobenzene hydrocarbon complexes in polar solvents. *J. Phys. Chem.* **1990,** *94*, 7534-7539.

9. Hubig, S. M.; Bockman, T. M.; Kochi, J. K., Optimized electron transfer in charge-transfer ion pairs. Pronounced inner-sphere behavior of olefin donors. *J. Am. Chem. Soc.* **1996,** *118*, 3842-3851.

10. Nicolet, O.; Vauthey, E., Ultrafast nonequilibrium charge recombination dynamics of excited donor-acceptor complexes. *J. Phys. Chem. A* **2002,** *106*, 5553-5562.

11. Mohammed, O. F.; Vauthey, E., Simultaneous generation of different types of ion pairs upon charge-transfer excitation of a donor-acceptor complex revealed by ultrafast transient absorption spectroscopy. *J. Phys. Chem. A* **2008,** *112*, 5804-5809.

12. Hubig, S. M.; Kochi, J. K., Photoinduced electron transfer in charge-transfer crystals by diffuse reflectance (picosecond) time-resolved spectroscopy. *J. Phys. Chem.* **1995,** *99*, 17578-17585.

13. Vincent, V. M.; Wright, J. D., Photoconductivity and crystal structure of organic molecular complexes. *J. Chem. Soc. Farad. Trans. I* **1974,** *70*, 58-71.

14. Samoc, M.; Williams, D. F., Photoconductivity in crystals of charge-transfer complex anthracene-tetracyanobenzene. *J. Chem. Phys.* **1983,** *78*, 1924-1930.

15. Gunes, S.; Neugebauer, H.; Sariciftci, N. S., Conjugated polymer-based organic solar cells. *Chem. Rev.* **2007,** *107*, 1324-1338.

16. Hwang, I. W.; Moses, D.; Heeger, A. J., Photoinduced carrier generation in P3HT/PCBM bulk heterojunction materials. *J. Phys. Chem. C* **2008,** *112*, 4350-4354.

17. Colombo, D. P.; Bowman, R. M., Does interfacial charge transfer compete with charge carrier recombination? A femtosecond diffuse reflectance investigation of TiO2 nanoparticles. *J. Phys. Chem.* **1996,** *100*, 18445-18449.

18. Asahi, T.; Furube, A.; Fukumura, H.; Ichikawa, M.; Masuhara, H., Development of a femtosecond diffuse reflectance spectroscopic system, evaluation of its temporal resolution, and applications to organic powder systems. *Rev. Sci. Inst.* **1998,** *69*, 361-371.

19. Kamat, P. V.; Gevaert, M.; Vinodgopal, K., Photochemistry on semiconductor surfaces. Visible light induced oxidation of C60 on TiO2 nanoparticles. *J. Phys. Chem. B* **1997,** *101*, 4422-4427.

20. Hinatu, J.; Yoshida, F.; Masuhara, H.; Mataga, N., On the relationship between ionic photodissociation yield and electron donor-acceptor interaction of 1,2,4,5-tetracyanobenzene and pyromellitic dianhydride complexes. *Chem. Phys. Lett.* **1978,** *59*, 8083.

21. Yoshihara, K.; Inoue, A.; Nagakura, S., Effect of high density excitons on fluorescence of naphthalene-tetracyanobenzene complex crystal. *Chem. Phys. Lett.* **1972,** *13*, 459-462.

22. Kozmenko, M. V.; Kuzmin, M. G., Luminescence of crystalline complexes of tetracyanobenzene with aromatic hydrocarbons. *Zh. Prik. Spekt.* **1977,** *27*, 429-434.

23. Betz, E.; Port, H.; Schrof, W.; Wolf, H. C., Energy transfer and exciton self-trapping in the charge-transfer crystal naphthalene-tetracyanobenzene. *Chem. Phys.* **1988,** *128*, 73-81.

24. Kobayashi, T.; Nagakura, S., The biexcitonic quenching and excitation migration rate in aromatic crystals. *Mol. Phys.* **1972,** *24*, 695-704.

25. Kao, F. J.; Wang, Y. M.; Chen, J. C.; Cheng, P. C.; Chen, R. W.; Lin, B. L., Photobleaching under single photon and multi-photon excitation: chloroplasts in protoplasts from Arabidosis thanliana. *Opt. Comm.* **2002,** *201*, 85-91.

26. Eggeling, C.; Widengren, J.; Rigler, R.; Seidel, C. A. M., Photobleaching of fluorescent dyes under conditions used for single molecule detection: evidence for two step photolysis. *Anal. Chem.* **1998,** *70*, 2651-2659.

27. Kumakura, S.; Iwasaki, F.; Saito, Y., The crystal structure of the 1:1 complex of naphthalene with 1,2,4,5-tetracyanobenzene. *Bull. Chem. Soc. Japan* **1967,** *40*, 1826-1833.

28. Macfarlane, R. M.; Ushioda, S., Raman study of orientational disorder in the molecular charge-transfer crystals naphthalene-TCNB and naphthalene-PMDA. *J. Chem. Phys.* **1977,** *67*, 3214-3220.

29. Boeyens, J. C. A.; Levendis, D. C., Static disorder in crystals of anthracene-tetracyanobenzene charge transfer complex. *J. Chem. Phys.* **1984,** *80*, 2681-2688.

30. Muhle, W.; Krzystek, J.; Schutz, J. U. V.; Wolf, H. C.; Stigler, R. D.; Stezowski, J. J., The 1:1 charge-transfer crystal fluorene-1,2,4,5-tetracyanobenzene (F-TCNB): triplet excitons, optical and structural properties. *Chem. Phys.* **1986,** *108*, 1-13.

31. Chin, K. K.; natarajan, A.; Gard, M. N.; Campos, L. M.; Shepherd, H.; Johansson, E.; Garcia-Garibay, M. A., Pump-probe spectroscopy and circular dichroism of nanocrystalline benzophenone -- towards absolute kinetic measurements in solid state photochemical reactions. *Chem. Commun.* **2007**, 4266-4268.

32. Kuzmanich, G.; Gard, M. N.; Garcia-Garibay, M. A., Photonic amplification by a singlet-state quantum chain reaction in the photdecarbonylation of crystalline diarylcyclopropenone. *J. Am. Chem. Soc.* **2009,** *131*, 11606-11614.

Chapter 4: Time-Resolved Studies of Charge Recombination in the Pyrene:TCNQ Charge-Transfer Crystal: Evidence for Tunneling

4.1 Introduction

Charge transfer (CT) in organic solid-state materials underlies many of the technological applications of these materials, from light-emitting diodes to photovoltaic cells. Molecular CT cocrystals, composed of alternating donor and acceptor molecules, provide a structurally well-defined medium in which the fundamental aspects of the CT process can be studied. Organic CT cocrystals and nanocrystals are also candidates for applications ranging from diodes to fluorescent probes.[1-3] In this work, we are concerned with crystals where the ground state consists of neutral donor and acceptor molecules, and the CT only occurs in the excited state after absorption of a photon. These "nonionic" CT crystals (as classified by McConnell[4]) typically exhibit a relatively weak, redshifted CT absorption band in addition to the absorption bands of their neutral constituents. The dynamics of CT complexes in solution have been extensively studied[5-8], but there has been less work on their solid-state electron transfer properties. We recently became interested in molecular CT crystals as highly ordered analogs for the bulk heterojunction polymer materials currently used in organic photovoltaics. Masuhara and others have shown that for many different CT complexes, the forward electron transfer process occurs very rapidly, usually within a few hundred femtoseconds.[9-11] Early work by Kochi on crystalline powders composed of conjugated acene donor molecules and the electron acceptor tetracyanobenzene (TCNB) suggested that these initially formed CT states could dissociate into free carriers with high efficiencies.[12] Upon reexamination, however, it was found that the TCNB complexes were highly susceptible to both

mechanical damage (resulting from grinding the crystals into powders) and photodamage (resulting from the high laser fluences used in transient absorption experiments).[13] In chapter 3 we concluded that there was little evidence for rapid dissociation of the bound CT state formed after photoexcitation. For our further study of molecular CT crystals, we had two goals. First, we wanted to identify a more robust CT molecular crystal system, where mechanical and laser damage would have negligible effects on the kinetics. Second, we wanted to study the fate of the charge transfer state created by photoexcitation in more detail and gain insight into the physical mechanism of charge recombination.

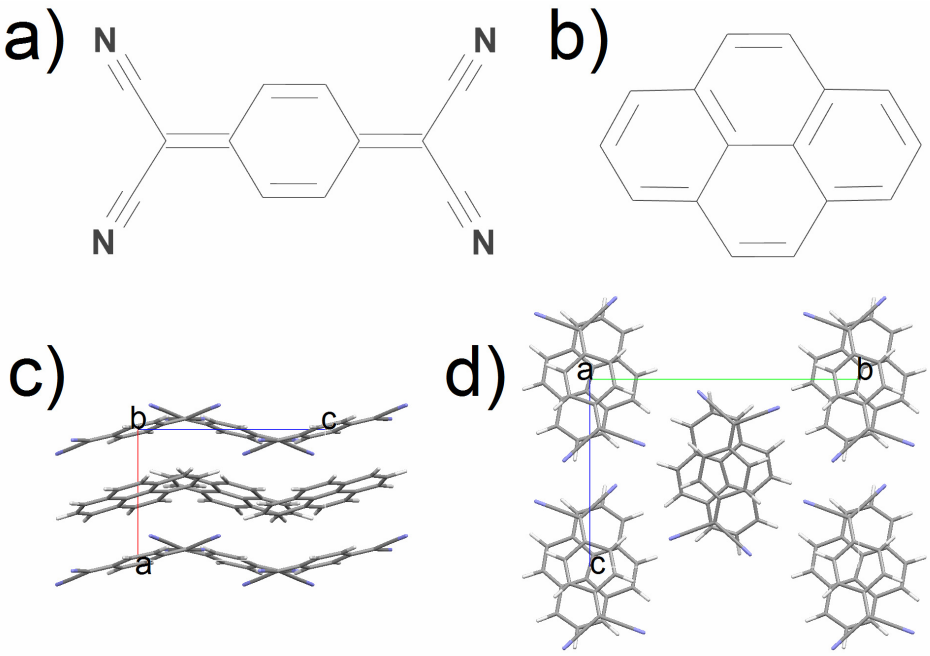

Figure 4.1: Chemical structures of **a)** TCNQ and **b)** pyrene, and the crystal structure of pyrene:TCNQ **c)** viewed from the side along the crystallographic *b* axis and **d)** viewed from the top of the stacks along the crystallographic *a* axis.

In order to achieve these two goals, we needed to identify a good model system. The previously identified problems with charge-transfer crystal stability were addressed by modifying the chemical system and preparation conditions. Rather than the fragile TCNB complexes, we turned to a different, higher molecular weight acceptor molecule, 7,7,8,8-tetracyanoquinodimethane (TCNQ). As our donor, we chose pyrene. The pyrene:TCNQ CT complex crystallizes in an alternating stacked geometry[14], as shown in Figure 4.1, and its optical properties have been measured.[15] More interestingly, this crystal has been shown to have high photoconductivity relative to other CT crystals, suggesting that it can produce free carriers after photoexcitation.[16] The growth of single crystals of this material is straightforward, but making powdered samples whose properties mirrored those of the single crystal proved difficult. Consistent data was obtained only for powders prepared using Teflon microbeads, rather than the usual $BaSO_4$ particles. We have characterized the absorption properties of the pyrene:TCNQ complex in both solution and in the crystalline state, showing that the CT absorbing state is similar in both. The solid-state luminescence decay is insensitive to both laser-induced photobleaching and to mechanical grinding, establishing this compound as being much more stable than its TCNB analog. The similar luminescence properties of the powder and crystal forms allow us to correlate time-resolved luminescence and pump-probe measurements. We find that the 290 ps luminescence decay is exactly mirrored by the decay of the TCNQ radical anion absorption and the recovery of the ground state bleach. Thus the fluorescence decay reflects the rate of charge recombination back into the neutral ground state. By performing temperature-dependent fluorescence lifetime

measurements, we find that this recombination is likely the result of an activated tunneling process involving a low frequency vibrational mode, possibly a crystal phonon. This rapid nonradiative recombination channel helps explain why the yield of dissociated charges from the initially excited radical cation-anion pair is so small. Such rapid recombination provides a reason, in addition to the interdigitated crystal structure, for why the photoconductivity of these donor-acceptor systems tends to be quite low relative to polymer bulk heterojunction systems.

4.2 Results and Discussion

4.2.1 Absorption Spectra and Calculation of the Absorption Coefficient of the CT Complex in Solution

When pyrene and TCNQ are mixed together in an organic solvent, they can associate to form a weakly bound complex with new absorption features that extend into the near infrared. Figure 4.2 shows the absorption spectra of the donor pyrene, the acceptor TCNQ, and the two new absorption bands at ~500 nm and 760 nm that arise from the CT absorption features of the donor-acceptor complex formed at high concentrations in $CHCl_3$ solution.

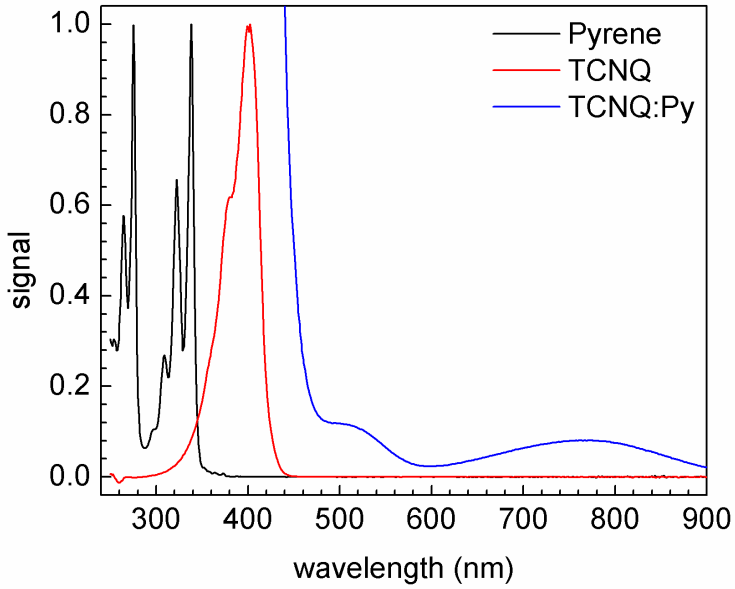

Figure 4.2: Steady-state absorption of monomeric pyrene (black), monomeric TCNQ (red), and a mixture of 0.37 mM TCNQ and 12 mM pyrene (blue) in $CHCl_3$. The plots for pyrene and TCNQ have been normalized to their peak emissions. In a mixed solution, the monomer absorptions dwarf that of the CT complex owing to its low epsilon and association constant.

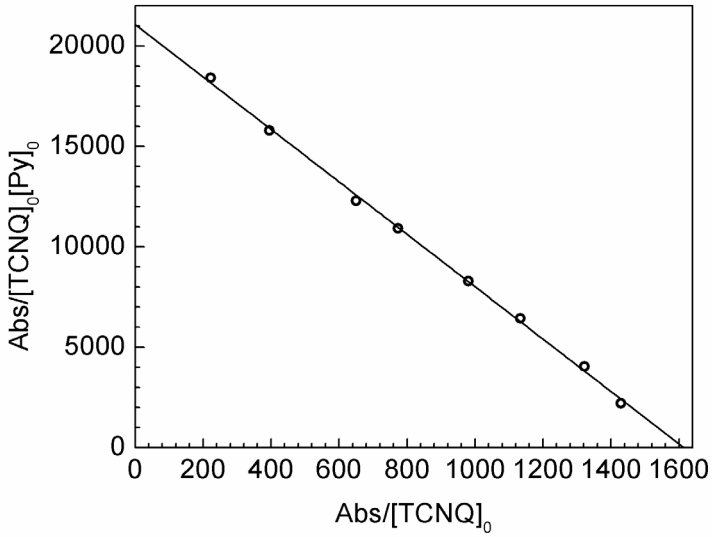

Figure 4.3: Scatchard plot for pyrene:TCNQ complex formation in $CHCl_3$. The relationship was linear over a saturation fraction range of 0.14 to 0.90, indicative of the exclusive formation of 1:1 complexes. From the slope and x-intercept of this graph, K and ε were determined to be 13.1 ± 0.2, and 1610 ± 30 L mol^{-1} cm^{-1} at 760 nm, respectively, as described in the text.

By varying the concentrations of the molecular components, both *K*, the equilibrium constant for CT complex formation, and its absorption coefficient $\varepsilon(\lambda_{CT})$ can be determined. As shown by previous workers, in the limit where the amount of CT formation is small relative to the monomer concentrations, but its absorbance $Abs(\lambda_{CT})$ is measurable, one can derive the following expression [20],

$$\frac{Abs(\lambda_{CT})}{[Py]_0[TCNQ]_0} = K\left(\varepsilon(\lambda_{CT}) - \frac{Abs(\lambda_{CT})}{[TCNQ]_0}\right) \tag{4.1}$$

where $[Py]_0$ and $[TCNQ]_0$ are the initial concentrations of the donor pyrene and acceptor TCNQ, respectively. A "Scatchard plot" of $\frac{Abs(\lambda_{CT})}{[Py]_0[TCNQ]_0}$ versus $\frac{Abs(\lambda_{CT})}{[TCNQ]_0}$ should result in a straight line where the slope is $-K$ and the y-intercept is $K\varepsilon(\lambda_{CT})$. By measuring the absorbance at 760 nm as a function of pyrene and TCNQ concentration, the data in Figure 4.3 is obtained, where K=13.1+/-0.2 and ε(760 nm) = 1610+/-30 $M^{-1}cm^{-1}$ are obtained. Our values differ slightly from those previously obtained by Ayad et al., who varied the TCNQ concentration over a more limited range.[21] To acquire data across a larger range of saturation fractions (the fraction of complexed species), we varied the pyrene concentration instead. We did not see any evidence of nonstoichiometric complexation in our absorption spectra, and the linearity of the Scatchard plot corroborated this.

4.2.2 Absorption and Fluorescence of the CT Crystals

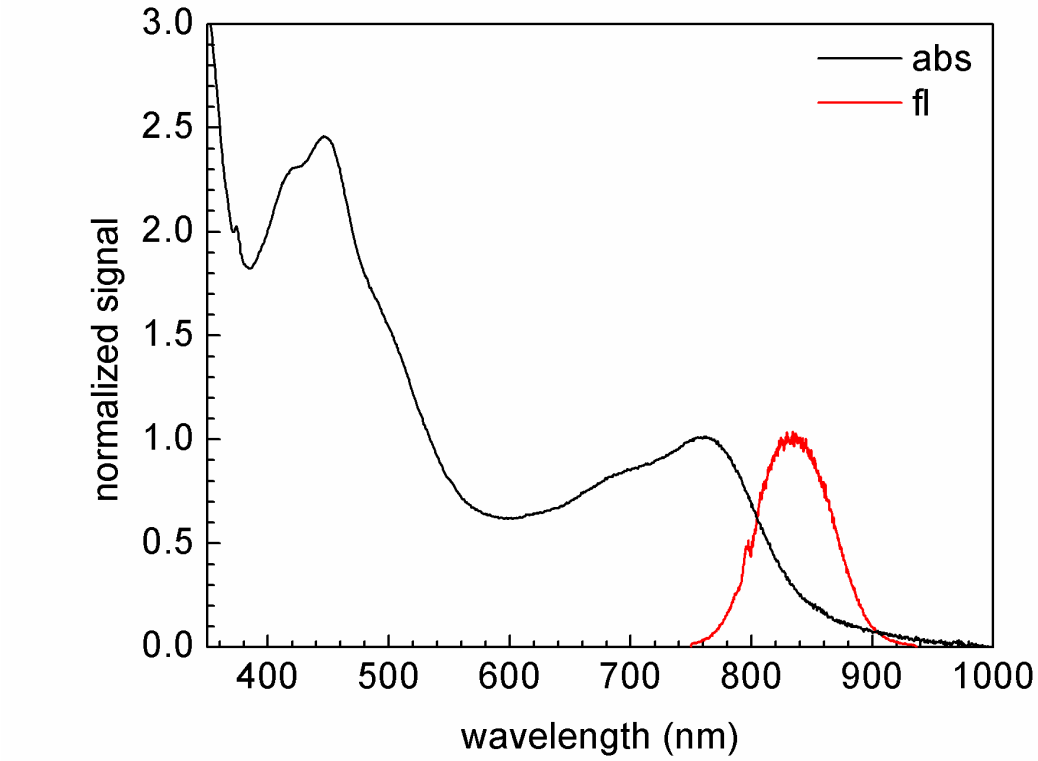

Figure 4.4. Absorption spectrum of a polycrystalline thin film and the fluorescence spectrum of a single crystal.

The solution absorption spectrum bears a close resemblance to that obtained for the CT crystal. Figure 4.4 shows the absorption spectrum of a film of pyrene:TCNQ microcrystals of pyrene:TCNQ, which shows the same broad bands at 500 nm and 760 nm as seen in the 1:1 solution complex. The location of these bands also agrees well with the absorption lineshape derived by Tanaka from a Kramers-Kronig analysis of the single crystal reflectance spectrum.[15] Due to their strong absorption that extends across the visible and into the near infrared, these crystals appear black. The major difference between the solution complex and the crystal is that the solid exhibits measurable

fluorescence. The luminescence spectrum of a pyrene:TCNQ crystal is also shown in Figure 4.4, centered at 840 nm. The broad, redshifted emission is characteristic of these CT compounds in the solid state. Note that no measurable fluorescence was observed for the pyrene:TCNQ complex in solution, where the absence of a rigid matrix appears to facilitate very rapid charge recombination and nonradiative relaxation, effectively quenching the fluorescence. Rapid charge recombination has been observed for CT complexes in liquid solutions[9], and this helps explain the absence of fluorescence, even for compounds that are emissive in the solid state. [22]

4.2.2 Effect of Photodamage and Mechanical Grinding on the Fluorescence

In order to investigate the mechanism of charge recombination in the solid-state, we wanted to use the fluorescence decay as a measure of the recombination rate. But to do this, we first had to investigate whether our pyrene:TCNQ samples demonstrated the same sensitivity to laser and mechanical damage as the previously studied TCNB complexes in chapter 3.[13] Figure 4.5a compares the normalized fluorescence decay of a pyrene:TCNQ single crystal before and after a 60 second laser exposure totaling 99 mJ/cm^2 at 400 nm. This fluence would have had a severe effect on the observed fluorescence decay of pyrene:TCNB, but has no effect on the decay rate of pyrene:TCNQ. The same resistance to photodamage was also observed in powders and microcrystals of pyrene:TCNQ. In all cases, the only effect of prolonged laser exposure was a decrease in overall signal level, but no change in the kinetics. The second question concerns the comparison of powder and single crystal spectroscopic data. Since transient absorption

experiments may only be performed on powdered samples due to the high optical density of single crystals, a comparison of luminescence decays with transient absorption dynamics requires that the two types of samples demonstrate the same behavior. When $BaSO_4$ was used as the inert filler, a non-exponential tail was observed in the fluorescence decay, in contrast to the purely single exponential decay seen in the neat crystals. When Teflon beads are used as the filler material, the tail was no longer present in the powder data. Figure 4.5b compares the decays obtained from the fluorescence of the single crystal and the powder sample in Teflon, both of which yield the same exponential relaxation time of 290 ps to within the experimental error. The results in Figures 5a and 5b establish that the kinetic results from the Teflon powdered crystal are applicable to the single crystal – mechanical grinding and photodamage do not induce new kinetic relaxation pathways, unlike in the TCNB CT crystals studied previously. A second advantage of the pyrene:TCNQ system is its single-exponential fluorescence decay and lack of spectral changes during the decay. The simple decay dynamics, indicative of a single excited state species, is in contrast to some TCNB crystals, where multiple emissive species can sometimes contribute to the decays.[13,23]

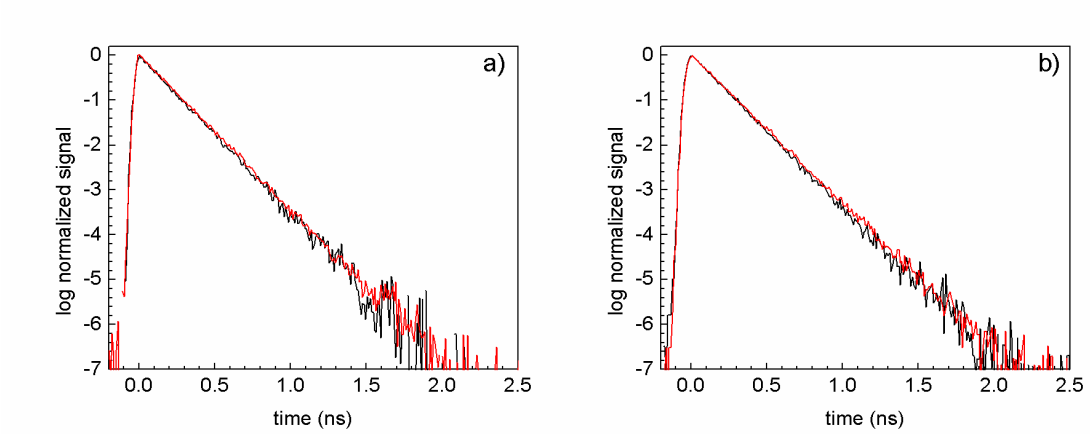

Figure 4.5. **a)** Fluorescence decay kinetics of a pyrene:TCNQ single crystal before (black) and after (red) a 60 s laser exposure of 99 μJ/cm^2. The signal level decreased, but the decay kinetics were unchanged. **b)** Comparison of the fluorescence decays for a single crystal (black) and a 2% by weight Teflon powder sample (red).

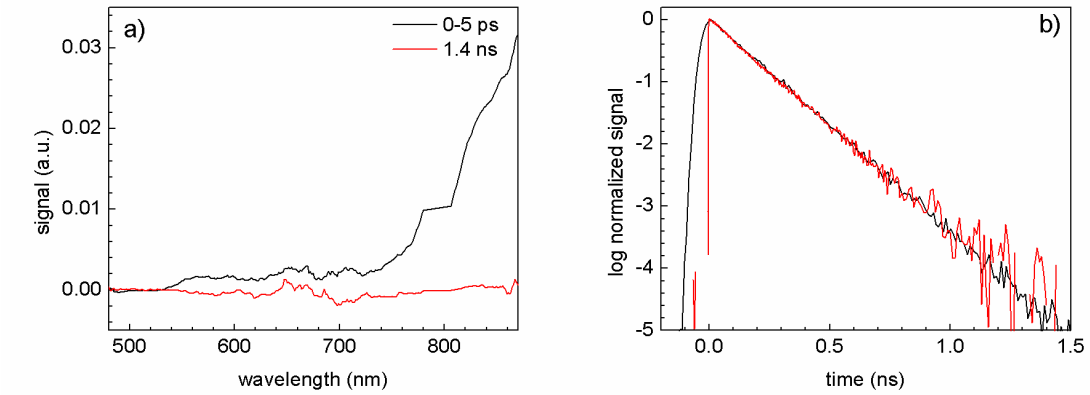

Figure 4.6. **a)** Transient absorption spectra of the powder sample at early (0-5 ps, black) and late (1.4 ns, red) delays. **b)** Comparison of the fluorescence decay of a single crystal (black) and the transient absorption decay at 820 nm of a powdered sample (red). Both signals decay with the same 290 ps time constant.

4.2.3 Transient Absorption

Transient absorption experiments were performed on the powdered CT sample in order to determine whether the fluorescence decay was due to relaxation back to the ground state, or into other types of long-lived excited states like triplets or separated charges. Such states are nonfluorescent but should manifest themselves in the TA experiment as long-lived induced absorption features or as a bleach of the CT absorption. In Figure 4.6a, the early (0-5 ps) and late (1400 ps) transient absorption spectra measured for the powdered sample is shown. Immediately after photoexcitation, there is an induced absorption that extends across the visible range but peaks past 800 nm. The strong absorption at longer wavelengths is consistent with the shape of the TCNQ radical anion absorption that has been observed in other experiments.[24-26] Although the 400 nm pump pulse would be expected to excite at least some neutral states, for example the TCNQ monomer, the formation of the CT state occurs within the time resolution of our measurement. We did not resolve any evolution of the TA spectrum within the 0-10 ps time window, other than the beginning of the slow decay. Rapid formation of the CT state after excitation of neutral states is consistent with results on other CT crystal systems.[9-11] Here we are more concerned with the rate of the reverse reaction, recombination of the separated charges. We can follow this process by monitoring the absorption feature at ~820 nm, which decays away completely by 1400 ps. After the absorption decays, there is no residual bleach or induced absorption that would indicate the presence of other species. When the decay of the anion TA signal at 820 nm is compared to that of the fluorescence, they overlap perfectly, as shown in Figure 4.6b. The

two different time-resolved experiments, fluorescence and transient absorption, give consistent results, indicating that the initially created CT state decays back to the neutral ground state via a single step process, without the measurable formation of long-lived intermediate or dark states like triplets or free carriers.

4.2.4 Fluorescence Temperature Dependence and Relaxation Mechanism

The data in Figure 4.6 establishes that the fluorescence decay of pyrene:TCNQ reflects relaxation from the CT state back to the neutral ground state, and that other relaxation channels play negligible roles. The last question we need to address is the mechanism of this relaxation. First, we fit the lowest energy CT absorption band in Figure 4.2 to a Gaussian lineshape function and use the Strickler-Berg relation[27] to estimate the radiative decay time τ_{rad}. Integration of $\varepsilon(\nu)$ from 600 nm to 900 nm yields τ_{rad}=220 ns. This value is almost 10^3 times larger than the observed τ_{fl}, indicating that the excited state relaxation is dominated by nonradiative charge recombination.

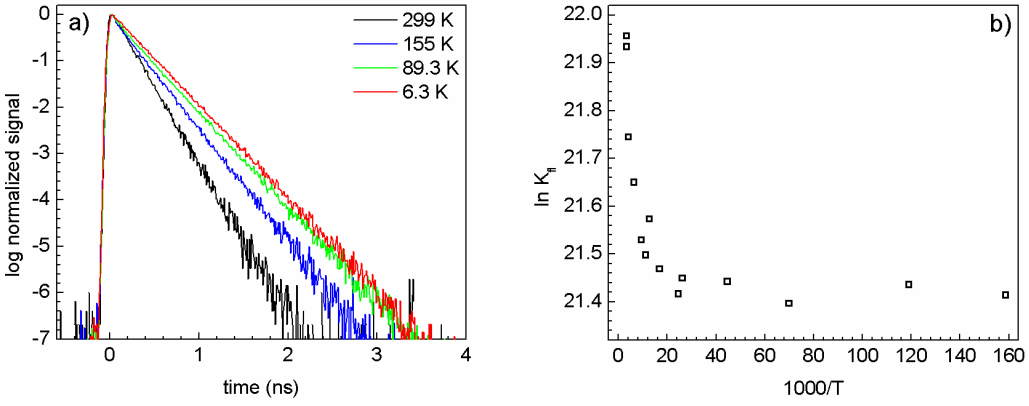

Figure 4.7. **a)** Crystal fluorescence decay at different temperatures. Below 60 K, the decay ceases to change. **b)** Arrhenius plot for the fluorescence decay rate k_{fl} versus inverse temperature, showing the cross-over from activated to tunneling regimes.

The fluorescence lifetime is only weakly dependent on temperature, as shown in Figure 4.7a, but remains single exponential at all temperatures. An Arrhenius plot of $\ln(k_{fl})$ versus 1000/T is shown in Figure 4.7b. At high temperatures, the linear slope of this curve indicates a thermally activated process, and in the range 300 K to 60 K we extract an activation energy of 0.2 kJ/mole. But after 60 K, the curve levels out and $k_{fl} = 3x10^9\ s^{-1}$ becomes independent of temperature. As mentioned above, this temperature-independent rate is orders of magnitude larger than the radiative decay rate. Non-Arrhenius behavior in electron-transfer systems can result from several different phenomena, including coupling to high-frequency vibrational modes [28-30], the influence of motions on widely separated timescales[31-32], and non-ergodic effects.[33] Distinguishing among these different but related mechanisms would require a detailed study, coupled with theoretical calculations, that is beyond the scope of this study. But this temperature-dependent behavior is very similar to what has been observed in other CT systems and attributed to tunneling.[34-39] Assuming that this is the case, then the transition between Arrhenius and non-Arrhenius behavior that occurs at T_{cross}~60 K can provide some clue as to the mechanism. If we use Buhks and Jortner's theory for the transition between the quantum and classical rate regimes [40-41], in the strong-coupling regime this cross-over should take place when

$$T_{cross} \sim \frac{\hbar\omega}{4k_B} \qquad (4.2)$$

where ω is the frequency of the generalized nuclear coordinate for the reaction and k_B is Boltzmann's constant. From this relation, we find ω~170 cm^{-1}. The nuclear coordinate

that is coupled to the charge recombination is unknown but probably involves the intermolecular separation of the donor and acceptor within the crystal lattice. Resonance Raman data for a closely related crystal system, perylene:TCNQ, indicates the presence of multiple intermolecular phonon modes in this frequency range.[42]

4.3 Conclusions

In this chapter we have extended our previous studies on the excited state relaxation in molecular CT crystals. Unlike the donor:TCNB cocrystals that we investigated in the previous chapter, the pyrene:TCNQ cocrystal shows simple kinetics that are robust with respect to both laser damage and mechanical perturbation. This material exhibits two CT transitions that extend its absorption into the near-infrared. Using a combination of picosecond photoluminescence and femtosecond transient absorption, we confirm that relaxation of the lowest energy CT state proceeds by nonradiative electron-hole recombination back to the neutral ground state. The recombination rate exhibits a transition from Arrhenius to non-Arrhenius behavior at 60 K. We interpret this temperature-dependence in terms of a thermally activated tunneling mechanism, and estimate that it is mediated by a vibration in the range of 170 cm^{-1}, consistent with the known phonon modes of similar crystals. Despite its low bandgap, pyrene:TCNQ is not a good analog for polymer bulk heterojunction systems, since it does not appear that the initially separated charges are able to diffuse away from each other. Instead, the charges recombine on a sub-nanosecond timescale in a process mediated by tunneling. It is possible that the pyrene:TCNQ cocrystal could provide a structurally

well-defined condensed phase system with which to test various theories of electron transfer. The positions of both donor and acceptor are well-defined, their electronic properties are well-studied, and the charge recombination rate can be measured unambiguously by spectroscopic means.

References

1. Wright, J. D. *Molecular Crystals*; 2nd ed.; Cambridge U. Press: Cambridge, 1995.

2. Hosaka, N.; Obata, M.; Suzuki, M.; Saiki, T.; Takeda, K.; Kuwata-Gonokami, M. *Appl. Phys. Lett.* **2008**, *92*, 113305/113301-113305/113303.

3. Al-Kaysi, R. O.; Muller, A. M.; Frisbee, R. J.; Bardeen, C. J. *Cryst. Growth Des.* **2009**, *9*, 1780-1785.

4. McConnell, H. H.; Hoffman, B. M.; Metzger, R. M. *Proc. Nat. Acad. Sci.* **1965**, *53*, 46-50.

5. Ojima, S.; Miyasaka, H.; Mataga, N. *J. Phys. Chem.* **1990**, *94*, 7534-7539.

6. Hubig, S. M.; Bockman, T. M.; Kochi, J. K. *J. Am. Chem. Soc.* **1996**, *118*, 3842-3851.

7. Nicolet, O.; Vauthey, E. *J. Phys. Chem. A* **2002**, *106*, 5553-5562.

8. Mohammed, O. F.; Vauthey, E. *J. Phys. Chem. A* **2008**, *112*, 5804-5809.

9. Fukazawa, N.; Fukamura, H.; Masuhara, H.; Prochorow, J. *Chem. Phys. Lett.* **1994**, *220*, 461-466.

10. Asahi, T.; Matsuo, Y.; Masuhara, H. *Chem. Phys. Lett.* **1996**, *256*, 525-530.

11. Asahi, T.; Matsuo, Y.; Masuhara, H.; Koshima, H. *J. Phys. Chem. A* **1997**, *101*, 612-616.

12. Hubig, S. M.; Kochi, J. K. *J. Phys. Chem.* **1995**, *99*, 17578-17585.

13. Dillon, R. J.; Bardeen, C. J. *J. Phys. Chem. A* **2011**, *115*, 1627-1633.

14. Prout, C. K.; Tickle, I. J.; Wright, J. D. *J. Chem. Soc. Perkin Trans. 2* **1973**, 528-530.

15. Tanaka, M. *Bull. Chem. Soc. Japan* **1978**, *51*, 1001-1008.

16. Vincent, V. M.; Wright, J. D. *J. Chem. Soc. Farad. Trans. I* **1974**, *70*, 58-71.

17. Asahi, T.; Furube, A.; Fukumura, H.; Ichikawa, M.; Masuhara, H. *Rev. Sci. Inst.* **1998**, *69*, 361-371.

18. Colombo, D. P.; Bowman, R. M. *J. Phys. Chem.* **1996**, *100*, 18445-18449.

19. Kamat, P. V.; Gevaert, M.; Vinodgopal, K. *J. Phys. Chem. B* **1997**, *101*, 4422-4427.

20. Deranleau, D. A. *J. Am. Chem. Soc.* **1969**, *91*, 4044-4049.

21. Ayad, M. M.; El-Daly, S. A. *Zeit. Physik. Chem.* **1995**, *190*, 211-221.

22. Short, G. D.; Parker, C. A. *Spectrochim. Acta A* **1967**, *23*, 2487-2489.

23. Betz, E.; Port, H.; Schrof, W.; Wolf, H. C. *Chem. Phys.* **1988**, *128*, 73-81.

24. Vandevyer, V.; Richard, J.; Barraud, A.; Ruaudel-Teixier, A.; Lequan, M.; Lequan, R. M. *J. Chem. Phys.* **1987**, *87*, 6754-6763.

25. Shida, T. *Electronic absorption spectra of radical ions*; Elsevier: New York, 1988.

26. Cho, K. S.; Nam, Y. S.; Kim, D.; Lee, W. H.; Choi, J. W. *Syn. Met.* **2002**, *129*, 157-163.

27. Strickler, S. J.; Berg, R. A. *J. Chem. Phys.* **1962**, *37*, 814-822.

28. Bixon, M.; Jortner, J. *J. Phys. Chem.* **1991**, *95*, 1941-1944.

29. Liang, N.; Miller, J. R.; Closs, G. L. *J. Am. Chem. Soc.* **1990**, *112*, 5353-5354.

30. Nan, G.; Wang, L.; Yang, X.; Shuai, Z.; Zhao, Y. *J. Chem. Phys.* **2009**, *130*, 024704/024701-024704/024708.

31. Cukier, R. I. *J. Chem. Phys.* **1988**, *88*, 5594-5605.

32. Dakhnovskii, Y.; Lubchenko, V.; Wolynes, P. *J. Chem. Phys.* **1996**, *104*, 1875-1885.

33. Matyushov, D. V. *Acc. Chem. Res.* **2007**, *40*, 294-301.

34. Barbara, P. F.; Meyer, T. J.; Ratner, M. A. *J. Phys. Chem.* **1996**, *100*, 13148-13168.

35. Asahi, T.; Ohkohchi, M.; Matsusaka, R.; Mataga, N.; Zhang, R. P.; Osuka, A.; Maruyama, K. *J. Am. Chem. Soc.* **1993**, *115*, 5665-5674.

36. Delaney, J. K.; Mauzerall, D. C.; Lindsey, J. S. *J. Am. Chem. Soc.* **1990**, *112*, 957-963.

37. Kroon, J.; Oevering, H.; Verhoeven, J. W.; Warman, J. M.; Oliver, A. M.; Paddon-Row, M. N. *J. Phys. Chem.* **1993**, *97*, 5065-5069.

38. Kuciauskas, D.; Liddell, P. A.; Lin, S.; Stone, S. G.; Moore, A. L.; Moore, T. A.; Gust, D. *J. Phys. Chem. B* **2000**, *104*, 4307-4321.

39. Lemmetyinen, H.; Tkachenko, N. V.; Efimov, A.; Niemi, M. *J. Phys. Chem. C* **2009**, *113*, 11475-11483.

40. Buhks, E.; Jortner, J. *J. Phys. Chem.* **1980**, *84*, 3370-3371.

41. Milosavljevic, B. H.; Thomas, J. K. *J. Am. Chem. Soc.* **1986**, *108*, 2513-2517.

42. Bandrauk, A. D.; Truong, K. D.; Carlone, C. *Can. J. Chem.* **1982**, *60*, 588-595.

Chapter 5: Correlating the Excited State Relaxation Dynamics as Measured by Photoluminescence and Transient Absorption with the Photocatalytic Activity of Au@TiO2 Core-shell Nanostructures

5.1 Introduction

Hydrogen is an attractive energy source, but commercial production of H_2 relies on a process that releases CO_2, negating the possible advantages of this fuel from the perspective of global warming.[1-2] The production of H_2 from H_2O using solar energy is a promising alternative, and currently there is much interest in developing photocatalytic materials that can absorb solar photons and drive the water splitting reaction $H_2O \rightarrow H_2 + \frac{1}{2} O_2$.[3-5] TiO_2 is the prototypical photocatalyst for solar water splitting, and its complex photochemistry has been studied for decades.[6-10] The photocatalytic properties of TiO_2 depend strongly on sample preparation conditions, crystal phase, and the presence of additional components, like metal particles, that are used to enhance the catalytic response. Considerable effort has been devoted to making new types of nanostructured colloidal TiO_2 photocatalysts, but in many cases their performance does not exceed that of commercially available P25 powder. Moreover, the ill-characterized nature of most photocatalysts hampers our ability to correlate photocatalytic behavior with specific photophysical behavior.

Over the last two years, the Yin group has developed the ability to tailor the properties of TiO_2 core-shell nanostructures, and to encapsulate gold nanoparticles inside titania shells to create Au@TiO_2 yolk-shell nanostructures in a controlled fashion.[7] The well-defined structural properties and high activity make these attractive materials for the

study of photocatalysis. Recent results have demonstrated that the crystallinity of the TiO_2 shell can be controlled by the etching and calcination conditions during preparation, and that the degree of crystallinity affects the TiO_2's capacity for photodegradation of organic dyes in aqueous solution.[11-12] The encapsulation of a gold nanoparticle inside the shell also enables these nanostructures to generate H_2 photocatalytically in the presence of a sacrificial electron donor like methanol.[13-17] The optimization of TiO_2 nanomaterials could be aided by the use of complementary spectroscopic measurements to probe the dynamics of the electron-hole pairs that drive the surface redox chemistry.

The question that we wish to address in this chapter is what spectroscopic measurables correlate with the photocatalytic properties of these core-shell materials. Time-resolved spectroscopy measurements have been used to follow the dynamics of the electron and hole created by photoexcitation, but there are no general rules that connect spectroscopic observables to catalysis figures-of-merit like H_2 production rates. This chapter reports an investigation of how changes in TiO_2 crystallinity affect the photophysical properties of these Au@TiO_2 yolk-shell structures. To probe how these changes affect the spectroscopic properties of the samples, we have measured both photoluminescence (PL) lifetimes and transient absorption (TA) kinetics. In parallel, we have used the H_2 production rate as a measure of catalytic activity. We find that while the H_2 output increases with increasing crystallinity, there is little or no change in either the TA kinetics or the PL lifetime for long wavelength (350 nm and 430 nm) photoexcitation. The only spectroscopic quantity that changes significantly with the nature of the sample is the lifetime of the PL after excitation at wavelengths well above

the TiO_2 bandgap (266 nm and 300 nm). The PL decays obey a stretched exponential decay in this heterogeneous material, and their characteristic lifetimes correlate well with the H_2 production rate. We hypothesize that carriers formed with excess energy are able to access various types of high-energy surface sites that can give rise to either PL and surface reactivity. The lifetimes of the PL emitting sites accessed by high-energy photoexcitation parallel those of the reactive sites, and thus provide an indicator for photocatalytic activity. Our results show that it is possible to find spectroscopic properties in these samples that correlate well with catalytic activity, but that care must be taken to define both the excitation conditions and the observable.

5.2 Results and Discussion

5.2.1 Sample Crystallinity

Different sample preparations led to clear differences in the TiO_2 shell crystallinity, as observed previously. Figure 5.1a shows representative TEM images for the four different samples used, labeled **A**, **B**, **C** and **D**. In these images, a single 20 nm diameter Au particle can be discerned in the interior of the each TiO_2 shell in all samples. In addition, it is clear that, as the etching and calcination conditions are varied, the shell granularity changes: Samples **A** and **B** appear similar, with shells that consist of sub-10 nm particles with random shapes, whereas Samples **C** and **D**, which were calcined at higher temperatures, display shells consisting of larger TiO_2 particles. In fact, crystal facets are visible on the largest particles of sample **D** in Figure 5.1a. Powder x-ray diffraction measurements show that the morphology changes visible in Figure 5.1a are

accompanied by the growth and sharpening of diffraction peaks that correspond to the anatase crystal phase. The increase in crystallinity can be assessed quantitatively from the increase in crystal grain size as calculated from the powder x-ray peakwidth using the Scherrer equation. The average grain size increases from 4 to 10 nm in samples **A**-**D**, as shown in Figure 5.1b.

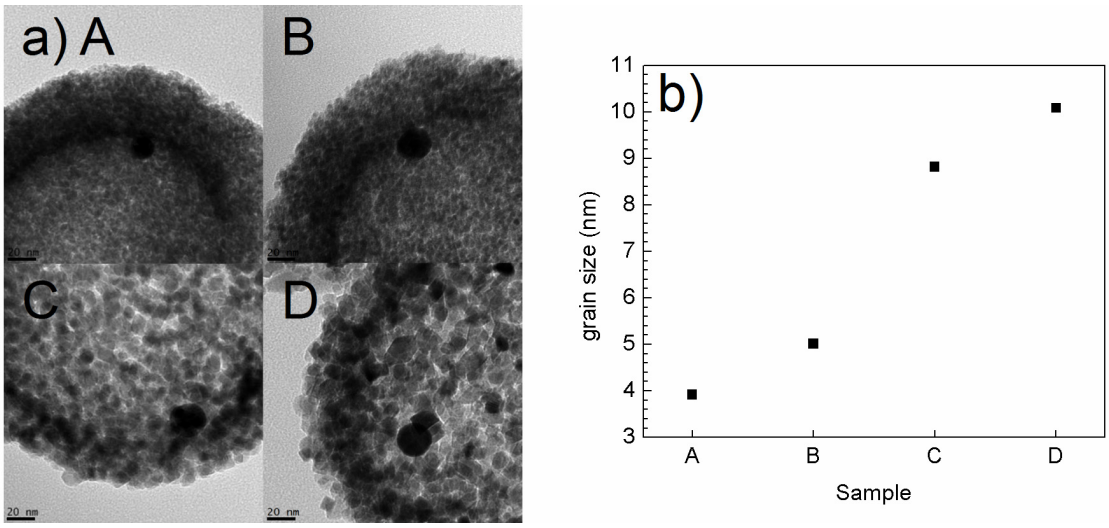

Figure 5.1: a) TEM images of the Au@TiO_2 samples used in this study. Each hollow nanosphere contains one 20 nm gold particle encased in a TiO_2 shell of ~40 nm thickness and ~200 nm overall diameter. Different silica etching and calcination conditions were used to systematically vary the crystalline grain sizes seen in these images. b) The average grain size for samples **A**-**D** calculated from powder x-ray diffraction data.

5.2.2 Photoluminescence

The electronic properties and catalytic performance of TiO_2 are sensitive to its crystallinity and preparation conditions. In seeking a spectroscopic observable that will be sensitive to the photocatalytic properties, the PL lifetime was monitored;

measurements in our lab and others, with other types of samples, have showed that longer PL lifetimes tend to correlate with better catalytic performance.[23-25] Although true band-edge PL from the TiO_2 conduction band has been observed around 400 nm,[26] in our samples the PL output is dominated by a broad emission centered around 500 nm. This emission has been attributed to either self-trapped excitons at intrinsic TiO_6 octahedral sites in the TiO_2 lattice,[27-29] or to surface defects, most likely oxygen vacancies.[30-35] Since it has been suggested that the luminescent surface site described above may play a role in electron trapping,[32] it is reasonable to expect that the dynamics of electron-hole recombination, as reflected in its PL lifetimes, may be relevant for its catalytic behavior.

We first note that the PL and TA dynamics for TiO_2 shells without the Au particles were virtually identical to the Au@TiO_2 structures, indicating that the small amount (<0.5% by weight) of Au that exists in these structures has a negligible effect on the electron-hole dynamics. Although the plasmon resonance of the Au particle at around 520 nm is clearly visible in the absorption spectra of the samples, its presence had no measurable effect on the shape of the PL decays, indicating that there was negligible quenching by this species. The Au particle plays an important role in photocatalysis, but it does not appear to influence the TiO_2 luminescence in a significant way. Since the presence of the gold is necessary for H_2 production, all the measurements described in this chapter were made on the Au@TiO_2 samples.

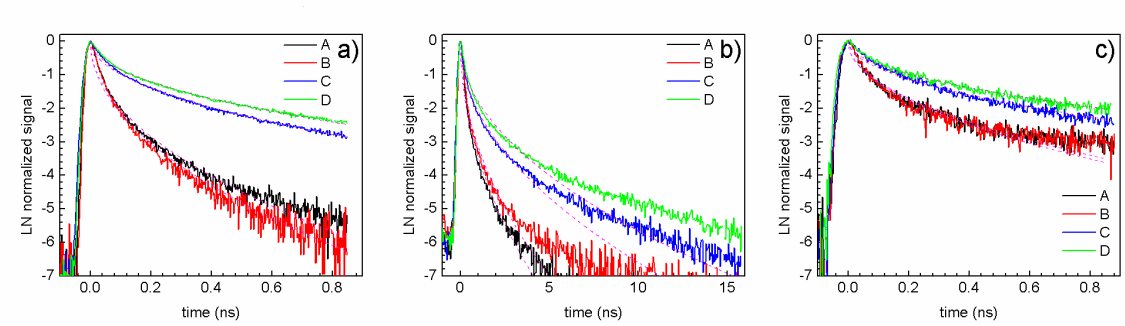

Figure 5.2: Photoluminescence lifetime of samples **A**-**D** using 266 nm excitation. Data taken under vacuum are shown in two different time windows: 1 ns (a) and 20 ns (b). Data taken in 10% MeOH solution are shown in (c), in a 1 ns time window. Also shown as dashed lines are fits to the data using the stretched exponential function given in Equation (1). The lifetimes are given in Table 5.1. The most crystalline sample, **D**, was also the longest-lived, with fluorescence lifetime values of τ_{PL}^{1ns} =140 ps (vacuum) and τ_{PL}^{1ns} =210 ps (10% MeOH) in the 1 ns time window.

In Figure 5.2, the PL dynamics are compared for the four samples used in our work, ranging from the most amorphous sample **A** to the most crystalline sample **D**, after excitation at 266 nm. Two time regimes are shown, a short time window (1 ns, Figure 5.2a) and a long time window (20 ns, Figure 5.2b). Perhaps the most important qualitative observation that can be derived from these data is that, in both windows, the decay of the PL of **A**, the most amorphous sample, is considerably more rapid than that of **D**, the most crystalline sample. Also, all the signal decays are highly nonexponential, which here were fitted (in both time windows) to a stretched exponential function of the form

$$S_{PL}(t) = S_{PL}(0)\exp\left[-\left(\frac{t}{\tau_{PL}}\right)^{1/2}\right] \qquad (1).$$

The choice of the nonexponential function and of the $t^{1/2}$ dependence is suggested by previous work, which shows that electron-hole recombination in these materials can be

satisfactorily described using such a stretched exponential function with an exponent of ~0.5.[36-37] Table 5.1 provides the fluorescence lifetimes (τ_{PL}) obtained for all four samples in both the 1 ns and 20 ns time windows for 266 nm excitation. Note that the τ_{PL} values for the 20 ns windows are slightly longer than those for the 1 ns windows. We were unable to fit the PL decay in both time windows with a single stretched exponential function, a fact that indicates that the PL dynamics are more complicated than that expected from a single type of heterogeneous process.

Sample	266 nm	300 nm	350 nm	430 nm	266 nm (10% MeOH)	266 nm (20ns window)
A	0.025	0.047	0.056	0.17	0.069	0.084
B	0.022	0.043	0.037	0.15	0.065	0.10
C	0.10	0.15	0.079	0.19	0.16	0.23
D	0.14	0.19	0.066	0.20	0.21	0.31

Table 5.1: Fluorescence lifetime (ns) of each sample vs. excitation wavelength. The lifetime (τ_{PL}) was calculated by fitting the data to equation (1). Data taken under vacuum with 1 ns time windows was used unless otherwise indicated.

Since the PL experiments described above were all done on dry samples under vacuum, we decided to see whether the same trend in PL lifetimes persisted when the samples were immersed in the same 10% methanol:water solution used in the photocatalysis experiments. In Figure 5.2c we show the PL decays for wet samples **A**-**D** in the 1 ns window, which can be compared to the decays for the dry samples in Figure 5.2a. For all samples, the decays are slower for the wet samples, but the overall trend of more crystalline samples having slower PL decays is the same. The slower decays are

consistent with other studies[35, 38] where band-bending due to the adsorption of donor/acceptor molecules at the surface suppresses electron-hole recombination, leading to increased steady-state PL intensities and longer lifetimes. Even though the absolute values of τ_{PL} lengthen by up to a factor of 2.5, as shown in Table 5.1, the wet and dry samples follow similar trends with sample crystallinity. Most of the experiments described in this chapter are done on dry samples, but the data in Figure 5.2 show that similar trends can be expected for wet samples as well.

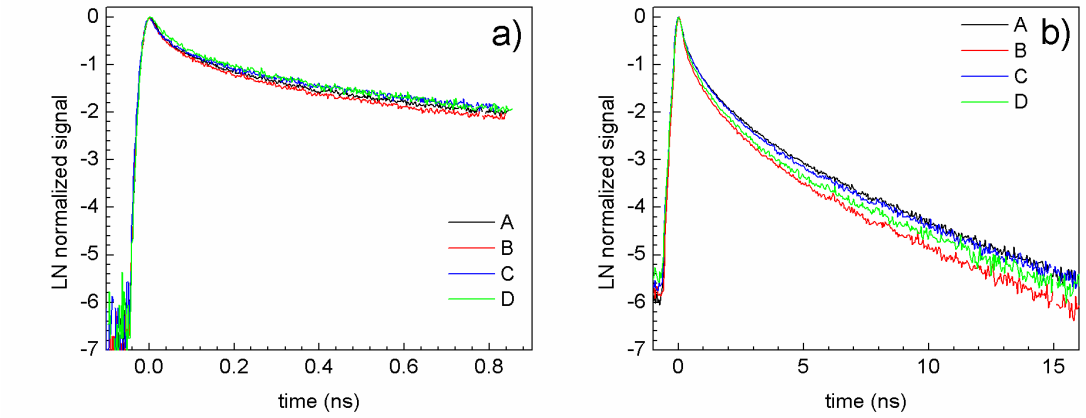

Figure 5.3: Fluorescence lifetime of samples **A-D** using 430 nm excitation in the short (a) and long (b) time windows. No significant changes in fluorescence lifetime with titania crystallinity are seen at this wavelength excitation.

The energy of 266 nm radiation is at least 1 eV above the TiO_2 band edge. In order to probe the dependence of titania photophysics on the wavelength of the radiation used, PL decays were also measured for excitation at 300 nm and 350 nm, and also at 430 nm, where only intragap states can be excited. It was found that the pronounced differences between samples **A-D** gradually diminished as the excitation was tuned to

lower energies. Figures 3a and 3b show the PL decays for samples **A** and **D** after excitation at 430 nm. When the data in Figure 5.3 are compared to that in Figure 5.2, two conclusions can be reached. First, the PL after excitation with 430 nm radiation is longer lived than that with 266 nm radiation. The systematic lengthening of the PL decay times as the excitation wavelength shifts to the red is summarized by the stretched exponential times given in Table 5.1 for the four wavelengths used. The second point is that samples **A** and **D** have very different decay dynamics for 266 nm excitation, but almost identical PL decays when excited at 430 nm.

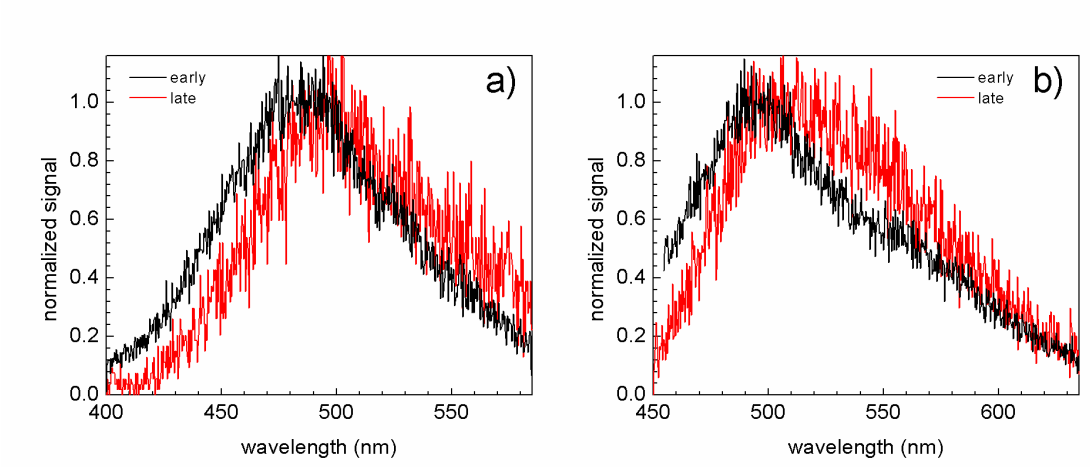

Figure 5.4: Fluorescence spectra of sample **D** at early (first 140 ps, 1 ns time window) and late time (5-20 ns time window) after 266 nm (a) and 430 nm (b) excitation. The only noticeable change in these experiments is a red shift in the maximum wavelength with time, but the same behavior was observed with all samples.

Next, the origins of the nonexponential PL decays were investigated by examining the PL spectra at different times during the decay. If the different time components reflect different chemical species, different spectra should be seen in

different time windows. However, no large shape changes were ever observed during the course of the PL decay: only a slight redshift of the PL spectrum with time was detected in all samples. An example of this redshift is provided in Figure 5.4 for the highly crystalline sample **D** in the form of the fluorescence spectra obtained after early (black traces) and late (red traces) times following excitation with 266 (Figure 5.4a) and 430 (Figure 5.4b) nm radiation. For 300 nm excitation the emission spectra resembled those in Figure 5.4, but excitation at 350 nm resulted in a blue-shifted emission, to a new spectrum centered at 460 nm. We do not have a good explanation for why the emission wavelength maximum varies with excitation energy, but this behavior has also been observed in other TiO_2 samples.[36] The important point is that the spectra are very similar among all the samples, regardless of their degree of crystallinity, as long as they are excited at the same wavelength. This suggests that similar emitting species are responsible for the PL signal in all samples. It is only the kinetics of the PL decay that change in a systematic way with TiO_2 morphology, and even then only when the excitation occurs well above the bandgap of the titania.

5.2.3 Transient Absorption

Given the variation observed in the PL lifetimes with titania shell crystallinity, transient absorption (TA) experiments were performed to determine if this observable is also affected by sample morphology. Previous work has shown that the picosecond TA decay rate may indeed be sensitive to the structure of the catalyst.[39] A pump pulse centered at 300 nm was chosen for these studies, because the PL behavior displayed

significant variations when excited at this wavelength. In our experiments, the TA showed a broad induced absorption after excitation that extended across the visible and near-infrared regions, a behavior characteristic of photoexcited TiO_2.[40] Even though the 300 nm pump wavelength excites mainly the TiO_2, we also observed a negative signal in the 500-600 nm wavelength region that appeared instantaneously and decayed within 10 ps. This negative signal was not observed in TiO_2 samples without Au particles, and we attributed this signal to bleaching of the Au plasmon band. The bleach was centered at 530 nm, the peak of the Au plasmon absorption, and the timescale of its decay is consistent with observations made by previous workers for both Au/TiO_2 systems[41-42] and Au particles in other media.[43] To avoid this interfering signal and observe dynamics due to the TiO_2 only, we monitored wavelengths well to the red of the Au plasmon band. Figure 5.5 shows traces of the TA signal at 820 nm, which should reflect the dynamics of both free and trapped electrons,[44] versus time for samples **A-D**; decays measured at other wavelengths showed similar time behavior. When compared to the PL decays obtained for the same samples, several important aspects of the TA data can be identified. First, both the PL and TA data show rapid initial decays on a similar timescale, in the first 0.1 ns. However, while almost the entire PL signal decays after 1 ns, the TA signal decreases by only ~50% in the same time frame. After this initial rapid decay, a large, long-lived component follows that extends past 1.5 ns.

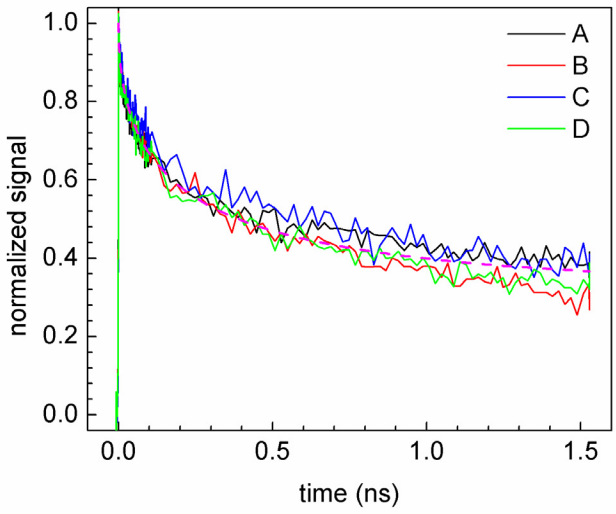

Figure 5.5: Decay of the induced absorption in Au@TiO_2 at 820 nm where the pump excitation is 300 nm. The transient absorption kinetics are very similar for all samples, regardless of crystallinity or photocatalytic activity. A calculated curve that reproduces the data using Equation (2) with values of τ_{TA}=230 ps, A=0.68, and B=0.32 is also shown.

Importantly, the time-resolved TA behavior reported above is similar in all four samples – there is no sign of the large changes observed in the PL for the different samples. The TA decays measured here are also similar to those seen in other types of TiO_2 samples, which have been attributed to electron-hole recombination.[40, 45-46] These bulk dynamics appear to be largely unaffected by the changes in sample crystallinity, unlike the 300 nm PL signals. The TA signal were fitted to an offset stretched exponential decay of the form

$$S_{TA}(t) = S_{TA}(0)\left[A\exp\left[-\left(\frac{t}{\tau_{TA}}\right)^{1/2}\right] + B\right] \qquad (2).$$

For all four samples, the data could be reproduced to within the signal-to-noise using values of τ_{TA}=230 ps, A=0.68, and B=0.32. There were slight variation in the long-time

offsets estimated from our fits between samples, but no systematic trend could be identified, and as shown in Figure 5.6, the fixed A and B values reported here gave adequate fits to all four data sets. Also to note is the fact that the value obtained for τ_{TA} is longer than those estimated for τ_{PL} in the 1 ns window, suggesting that these two experiments probe the photophysics of different species.

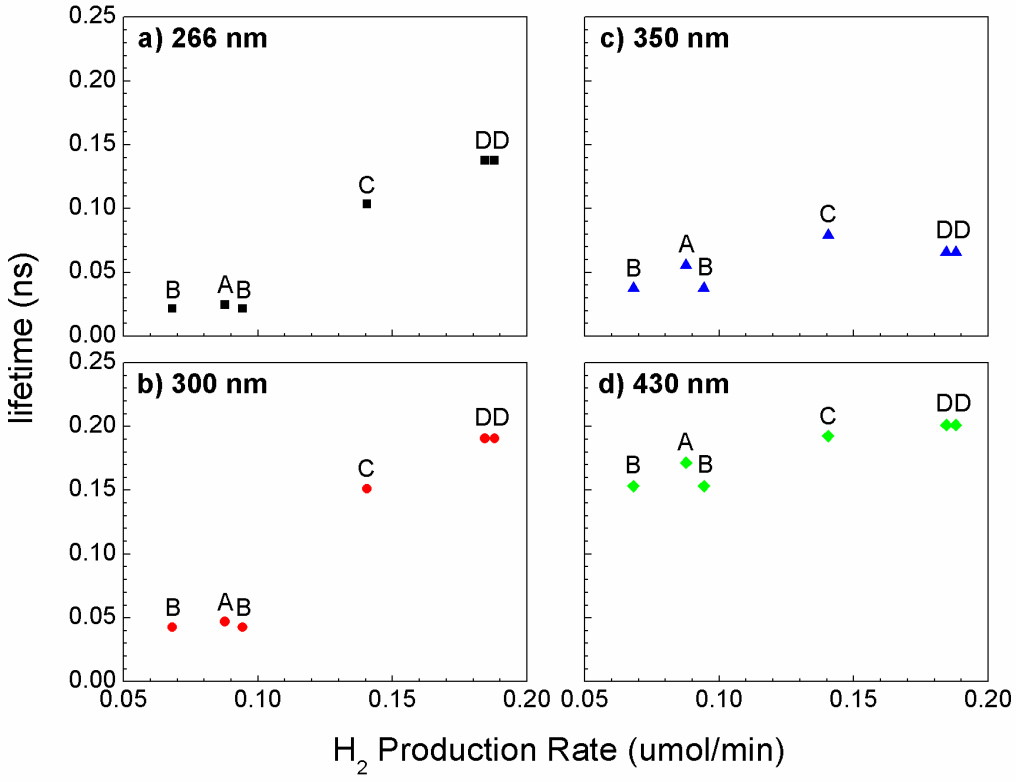

Figure 5.6: Correlations between fluorescence lifetimes and photocatalytic activity. Data are reported for four different excitation wavelengths: (a) 266 nm; (b) 300 nm; (c) 350 nm; and (d) 430 nm. The calculated lifetimes were obtained by fitting of the first nanosecond (short time window) of the decays to a stretched exponential decay function, as described in the text. Clear correlations are identified with the fluorescence induced by 266 and 300 nm excitation but are weaker for 350 and 430 nm excitation.

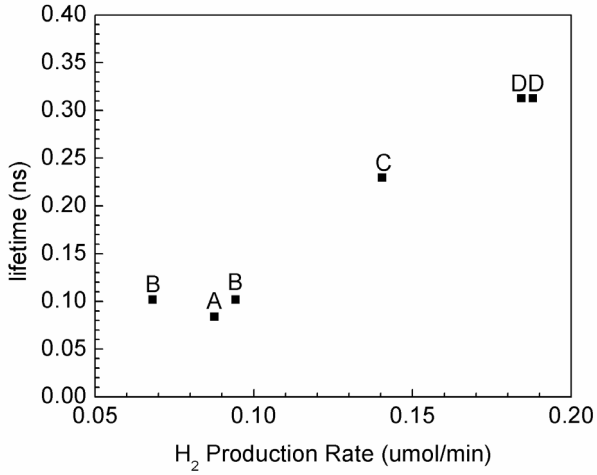

Figure 5.7: Correlation between photoluminescence lifetime extracted from fits to data in a 20 ns time window and the photocatalytic activity. The photoluminescence excitation wavelength was 266 nm. The fluorescence decays in this longer time window show a correlation with H_2 production similar to those in the 1 ns time window shown in Figure 5.6a.

5.2.4 Photocatalytic Activity

As mentioned earlier, the photocatalytic activity of TiO_2 is known to depend on sample crystallinity. In order to correlate the photophysics and photocatalytic properties of our samples, the rate of H_2 production from 1% by weight suspensions of the Au@TiO_2 yolk-shell particles was measured under ultraviolet radiation. Figure 5.6 shows the plots of the τ_{PL} extracted from the PL decays in the 1 ns time window for four excitation wavelengths versus the H_2 production rate. Note that two different samples corresponding to preparations **B** and **D** were measured, both of which are shown in Figures 6 and 7. The multiple measurements provide an indication of the sample-to-sample reproducibility of our results. The PL lifetimes extracted after excitation at 266 nm and 300 nm show a clear correlation with photocatalytic activity, as can be seen from the data in Figures 6a and 6b. For lower energy excitations, 350 nm and 430 nm, no

strong dependence of τ_{PL} on the nature of the sample was observed, and thus no obvious correlation with H_2 production could be derived (Figures 6c and 6d). Similarly, no correlation between the initial TA decay time τ_{TA} and H_2 production could be obtained, since this time was the same to within the error for all four samples.

In summary, the data in Figure 5.6 show that only a certain subset of TiO_2 PL decays are reflective of the physical changes that control the photocatalytic activity of the nanoparticles, and that the PL decays on the 1 ns timescale obtained after high-energy excitation appear to provide a good indication of physical changes that affect the photocatalysis. This is also true for the PL decays in the longer time windows as long as the excitation is well above the bandgap. Figure 5.7 shows a plot of the characteristic PL lifetime from the 20 ns time window, τ_{PL}^{20ns}, versus H_2 production rate. Higher crystallinity results in longer lifetimes for both the short- and long-lived species, and thus the correlation with photocatalytic activity extends to longer timescales as well.

5.2.5 Discussion

The goal of this chapter is to better understand the underlying physics of the photoexcitation and their role in the subsequent chemistry of the catalyst. In this context, an important result is that the PL lifetimes depend on crystallinity and are correlated with the H_2 production rate. It was also determined that the extent of this correlation increases with increasing excitation energy, well above the energy of the bandgap. Previous measurements of the catalytic action spectrum for TiO_2 have shown that both H_2 production[47] and its photo-oxidation reactivity[48-50] depend on the photon energy even

above the bandgap, with higher energy photons leading to greater reactivity. This fact suggests that different types of surface sites are accessed by different photon energies, and that only electron-hole pairs created with significant excess energy can drive H_2 production. If we assume that there are different types of emissive sites as well, then only the sites populated by high energy photoexcitation appear to be sensitive to the TiO_2 crystallinity. It is reasonable to ask whether the PL and reactivity originate from the same sites. For several reasons, we think that the emissive species are probably not directly involved in the catalysis. First, their emission is not quenched in the presence of methanol/water mixtures but instead increases in intensity. This is the opposite of what would be expected if the emitting states could rapidly react with molelcules bound to the surface. Second, although the data in Figure 5.6 are too sparse to derive a equation that quantitatively predicts the H_2 production rate based on the PL lifetime, this curve does suggest that H_2 production and PL originate from distinct states. If a linear relation is assumed, then we can extrapolate from the data that the PL lifetime would go to zero before the H_2 production rate would (i.e. a line through the data would not pass through the origin). This fact reinforces the idea that while the PL sites and reactive sites may be created by the same photons, they are chemically distinct. A linear fit to the data in Figure 5.6 would predict that it is possible to have dark states that generate H_2 in the absence of any PL excited at 266 nm, for example.

Now that we have established that the PL from sites excited by high energy photons correlates with photocatalytic activity, we now turn to the physical origin of this correlation. One possible origin of changes in the reactivity between samples **A-D** is

suggested by the TEM images in Figure 5.1a that show how the size of the nanoparticles that make up the TiO_2 shell increases for the higher temperature calcination conditions. The increased grain size would lower the surface/volume ratio and possibly decrease the photocatalytic activity, but experimentally we observe the opposite trend, with larger grains having higher photocatalytic activity. Thus we believe that changes in the nanoparticle size play a secondary role in the photoreactivity of the core-shell structures, and that the crystallinity of the constituent particles is more important.[12] Improved TiO_2 crystallinity can enhance photocatalytic performance through a lower density of the defect sites that facilitate electron-hole recombination.[51] Indeed, the electron-hole recombination time is much slower in bulk single crystals.[52-53] It is likely that both reactive and luminescent states are subject to recombination processes mediated by the presence of defects and charge diffusion across a disordered interfacial region. In this interpretation, more rapid recombination in the less crystalline samples is expected to lead to both less PL from the emitting sites and less H_2 production from the reactive sites. In effect, it appears that the emissive species formed by high-energy photoexcitation are good surrogates for the surface reactive species. It is important to point out that this is not the case for the electron-hole pairs probed by the TA experiments or the emissive species created by lower energy photons.

The main conclusion from our work is that it is possible to identify clear correlations between the PL lifetimes after high-energy (wavelength $\leq$ 300 nm) excitation and the rates of hydrogen production rates in our well-defined Au@TiO_2 yolk-shell samples. Both those parameters increase with the degree of crystallinity of the titania.

Based on these observations, it can be concluded that the PL behavior may be used to evaluate the potential performance of this class of photocatalysts. These correlations also suggest that the two properties, PL and H_2 production, depend on the same underlying physical phenomenon, presumably the generation of charge-separated states on the titania surface after photoexcitation. Our results are consistent with those of Anpo and coworkers, who explored the connection between PL and catalytic activity in TiO_2 particles, concluding that both processes are related to surface states.[38, 54]

5.3 Conclusions

In this chapter, we have characterized a series of Au@TiO_2 yolk-shell nanostructures whose crystallinity was varied by changing the etching and calcination conditions. Parallel measurements were carried out for both the spectroscopic and the photocatalytic properties of those samples, allowing us to search for correlations between the two behaviors. It was found that the crystallinity of the titania shells exerts a strong effect exerted on both the H_2 production rate and the stretched exponential lifetime of the PL created by short-wavelength photoexcitation. On the other hand, there was no discernible effect of crystallinity on long-wavelength excited PL, or on the dynamics of the bulk electrons as measured by femtosecond TA. We hypothesize that the high-energy photons create both reactive and emissive charge-separated states in parallel, and that both species are subject to similar recombination processes that decrease their lifetimes and thus both the PL output and the H_2 production rate. In order to generate a quantitative connection between the two quantities, a kinetic model would need to be

developed and tested that describes both types of processes. Such a model is beyond the scope of the current study, but the results described here suggest that it is a reasonable goal. While our results have been obtained on a series of specific Au@TiO_2 nanostructures, it is hoped that the conclusions reached may be applicable to other TiO_2 morphologies. The important result of this work is that, by using a structurally well-defined system, it has been possible to identify a spectroscopic observable, the PL lifetime after high energy photoexcitation, that correlates well with photocatalytic activity.

References

1. Rostrup-Nielsen, J. R., Fuels and energy for the future: The role of catalysis. *Catal. Rev. Sci. Eng.* **2004,** *46*, 247-270.

2. Navarro, R. M.; Pena, M. A.; Fierro, J. L. G., Hydrogen production reactions from carbon feedstocks: fossil fuels and biomass. *Chem. Rev.* **2007,** *107*, 3952-3991.

3. Osterloh, F. E., Inorganic materials as catalysts for photochemical splitting of water. *Chem. Mater.* **2008,** *20*, 35-54.

4. Maeda, K.; Domen, K., Photocatalytic water splitting: recent progress and future challenges. *J. Phys. Chem. Lett.* **2010,** *1*, 2655-2661.

5. Xing, J.; Fang, W. Q.; Zhao, H. J.; Yang, H. G., Inorganic photocatalysts for overall water splitting. *Chemistry -- An Asian Journal* **2012,** *7*, 642-657.

6. Fujishima, A.; Honda, K., Electrochemical photolysis of water at a semiconductor electrode. *Nature* **1972,** *238*, 37-38.

7. Thompson, T. L.; Yates, J. T., TiO_2-based photocatalysis: surface defects, oxygen and charge transfer. *Topics Catal.* **2005,** *35*, 197-210.

8. Ni, M.; Leung, M. K. H.; Leung, D. Y. C.; Sumathy, K., A review and recent developments in photocatalytic water splitting using TiO_2 for hydrogen production. *Renew. Sustain. Energy Rev.* **2007,** *11*, 401-425.

9. Fujishima, A.; Zhang, X.; Tryk, D. A., TiO_2 photocatalysis and related surface phenomena. *Surf. Sci. Rep.* **2008,** *63*, 515-582.

10. Henderson, M. A., A surface science perspective on photocatalysis. *Surf. Sci. Rep.* **2011,** *66*, 185-297.

11. Joo, J. B.; Zhang, Q.; Lee, I.; Dahl, M.; Zaera, F.; Yin, Y., Mesoporous anatase titania hollow nanostructures through silica-protected calcination. *Adv. Funct. Mater.* **2012,** *22*, 166-174.

12. Joo, J. B.; Zhang, Q.; Dahl, M.; Lee, I.; Goebl, J.; Zaera, F.; Yin, Y., Control of the nanoscale crystallinity in mesoporous TiO_2 shells for enhanced photocatalytic activity. *Energy Environ. Sci.* **2012,** *5*, 6321.

13. Kamat, P. V., Photophysical, photochemical, and photocatalytic aspects of metal nanoparticles. *J. Phys. Chem. B* **2002,** *106*, 7729-7744.

14. Bamwenda, G. R.; Tsubota, S.; Nakamura, T.; Haruta, M., Photoassisted hydrogen production from a water-ethanol solution: a comparison of activities of Au-TiO_2 and Pt-TiO_2. *J. Photochem. Photobio. A* **1995,** *89*, 177-189.

15. Chiarello, G. L.; Selli, E.; Forni, L., Photocatalytic hydrogen production over flame spray pyrolysis-synthesized TiO_2 and Au/TiO_2. *Appl. Catal. B* **2008,** *84*, 332-339.

16. Rosseler, O.; Shankar, M. V.; Du, M. K.-L.; Schmidlin, L.; Keller, N.; Keller, V., Solar light photocatalytic hydrogen production from water over Pt andAu/TiO_2 (anatase/rutile) photocatalysts: influence of noble metal and porogen production. *J. Catalysis* **2010,** *269*, 179-190.

17. Silva, C. G.; Juarez, R.; Marino, T.; Molinari, R.; Garcia, H., Influence of excitation wavelength (UV or visible light) on the photocatalytic activity of titania containing gold nanoparticles for the generation of hydrogen or oxygen from water. *J. Am. Chem. Soc.* **2011,** *133*, 595-602.

18. Lee, I.; Joo, J. B.; Yin, Y.; Zaera, F., A yolk@shell nanoarchitecture for Au/TiO_2 catalysts. *Angew. Chem. Int. Ed.* **2011,** *50*, 10208-10211.

19. Colombo, D. P.; Bowman, R. M., Femtosecond diffuse reflectance spectroscopy of TiO_2 powders. *J. Phys. Chem.* **1995,** *99*, 11572-11576.

20. Kamat, P. V.; Gevaert, M.; Vinodgopal, K., Photochemistry on semiconductor surfaces. Visible light induced oxidation of C60 on TiO_2 nanoparticles. *J. Phys. Chem. B* **1997,** *101*, 4422-4427.

21. Asahi, T.; Furube, A.; Fukumura, H.; Ichikawa, M.; Masuhara, H., Development of a femtosecond diffuse reflectance spectroscopic system, evaluation of its temporal resolution, and applications to organic powder systems. *Rev. Sci. Inst.* **1998,** *69*, 361-371.

22. Tamaki, Y.; Furube, A.; Murai, M.; Hara, K.; Katoh, R.; Tachiya, M., Dynamics of efficient electron-hole separation in TiO_2 nanoparticles revealed by femtosecond transient absorption spectroscopy under the weak excitation condition. *Phys. Chem. Chem. Phys.* **2007,** *9*, 1453-1460.

23. Zhang, Z.; Lin, Q.; Kurunthu, D.; Zuo, F.; Zheng, S.-T.; Bardeen, C. J.; Feng, P., Synthesis and Photocatalytic Properties of a Novel Heteropolyniobate Compound: $K_{10}[Nb_2O_2(H_2O)_2][SiNb_{12}O_{40}].12H_2O$. *J. Am. Chem. Soc.* **2011,** *133*, 6934-6937.

24. Zuo, F.; Bozhilov, K.; Dillon, R. J.; Wang, L.; Smith, P.; Zhao, X.; Bardeen, C.; Feng, P., Active facets on titantium(III)-doped TiO_2: an effective strategy to improve the visible-light photocatalytic activity. *Angew. Chem. Int. Ed.* **2012,** *124*, 6327-6330.

25. Harada, N.; Goto, M.; Ijima, K.; Sakama, H.; Ichikawa, N.; Kunugita, H.; Ema, K., Time-resolved luminescence of TiO_2 powders with different crystal structures. *Jap. J. Appl. Phys.* **2007,** *46*, 4170-4171.

26. Serpone, N.; Lawless, D.; Khairutdinov, R., Size effects on the photophysical properties of colloidal anatase TiO_2 particles: size quantization or direct transitions in this indirect semiconductor? *J. Phys. Chem.* **1995,** *99*, 16646-16654.

27. Tang, H.; Berger, H.; Schmid, P. E.; Levy, F., Photoluminescence in TiO_2 anatase single crystals. *Sol. State Comm.* **1993,** *87*, 847-850.

28. Hosaka, N.; Sekiya, T.; Kurita, S., Excitonic state in anatase TiO_2 single crystal. *J. Lumin.* **1997,** *72-74*, 874-875.

29. Watanabe, M.; Sasaki, S.; Hayashi, T., Time-resolved study of photoluminescence in anatase TiO_2. *J. Lumin.* **2000,** *87-89*, 1234-1236.

30. Forss, L.; Schubnell, M., Temperature dependence of the luminescence in TiO_2 powder. *Appl. Phys. B* **1993,** *56*, 363-366.

31. Mochizuki, S.; Shimizu, T.; Fujishiro, F., Photoluminescence study on defects in pristine anatase and anatase-based composites. *Physica B* **2003,** *340-342*, 956-959.

32. Shi, J.; Chen, J.; Feng, Z.; Chen, T.; Lian, Y.; Wang, X.; Li, C., Photoluminescence characteristics of TiO_2 and their relationship to the photoassisted reaction of water/methanol mixture. *J. Phys. Chem. C* **2007,** *111*, 693-699.

33. Knorr, F. J.; Zhang, D.; McHale, J. L., Influence of $TiCl_4$ treatment on surface defect photoluminescence in pur and mixed-phase nanocrystalline TiO_2. *Langmuir* **2007,** *23*, 8686-8690.

34. Mercado, C. C.; Knorr, F. J.; McHale, J. L.; Usmani, S. M.; Ichimura, A. S.; Saraf, L. V., Location of hole and electron traps on nanocrystalline anatase TiO_2. *J. Phys. Chem. C* **2012,** *116*, 10796-10804.

35. Stevanovic, A.; Buttner, M.; Zhang, Z.; Yates, J. T., Photoluminescence of TiO_2: effect of UV light and adsorbed molecules on surface band structure. *J. Am. Chem. Soc.* **2012,** *134*, 324-332.

36. Fujihara, K.; Izumi, S.; Ohno, T.; Matsumura, M., Time-resolved photoluminescence of particulate TiO_2 photocatalysts suspended in aqueous solutions. *J. Photochem. Photobio. A* **2000,** *132*, 99-104.

37. Katoh, R.; Furube, A., Tunneling-type charge recombination in nanocrystalline TiO_2 films at low temperature. *J. Phys. Chem. Lett.* **2011,** *2*, 1888-1891.

38. Anpo, M.; Tomonari, M.; Fox, M. A., In situ photoluminescence of TiO_2 as a probe of photocatalytic reactions. *J. Am. Chem. Soc.* **1989,** *93*, 7300-7302.

39. Furube, A.; Asahi, T.; Masuhara, H.; Yamashita, H.; Anpo, M., Charge-carrier dynamics of standard TiO_2 catalysts revealed by femtosecond diffuse reflectance spectroscopy. *J. Phys. Chem. B* **1999,** *103*, 3120-3127.

40. Tachikawa, T.; Fujitsuka, M.; Majima, T., Mechanistic insight into the TiO_2 photocatalytic reactions: design of new photocatalysts. *J. Phys. Chem. C* **2007,** *111*, 5259-5275.

41. Furube, A.; Du, L.; Hara, K.; Katoh, R.; Tachiya, M., Ultrafast plasmon-induced electron transfer from gold nanodots into TiO_2 nanoparticles. *J. Am. Chem. Soc.* **2007,** *129*, 14852-14853.

42. Zhang, C.; Liu, Y.; You, G.; Li, B.; Shi, J.; Qian, S., Ultrafast nonlinear optical response of Au:TiO_2 composite nanoparticle films. *Physica B* **2005,** *357*, 334-339.

43. Link, S.; Furube, A.; Mohamed, M. B.; Asahi, T.; Masuhara, H.; El-Sayed, M. A., Hot electron relaxation dynamics of gold nanoparticles embedded in MgSO4 powder compared to solution: the effect of the surrounding medium. *J. Phys. Chem. B* **2002,** *106*, 945-955.

44. Yoshihara, T.; Katoh, R.; Furube, A.; Tamaki, Y.; Murai, M.; Hara, K.; Murata, S.; Arakawa, H.; Tachiya, M., Identification of reactive species in photoexcited TiO_2 films by wide-wavelength range (400-2500 nm) transient absorption spectroscopy. *J. Phys. Chem. B* **2004,** *108*, 3817-3823.

45. Colombo, D. P.; Bowman, R. M., Does interfacial charge transfer compete with charge carrier recombination? A femtosecond diffuse reflectance investigation of TiO_2 nanoparticles. *J. Phys. Chem.* **1996,** *100*, 18445-18449.

46. Tamaki, Y.; Furube, A.; Murai, M.; Hara, K.; Katoh, R.; Tachiya, M., Direct observation of reactive trapped holes in TiO_2 undergoing photocatalytic oxidation of adsorbed alcohols: evaluation of the reaction rates and yields. *J. Am. Chem. Soc.* **2006,** *128*, 416-417.

47. Torimoto, T.; Aburakawa, Y.; Kawahara, Y.; Ikeda, S.; Ohtani, B., Light intensity dependence of the action spectra of photocatalytic reactions with anatase titanium(IV) oxide. *Chem. Phys. Lett.* **2004,** *392*, 220-224.

48. Driessen, M. D.; Grassian, V. H., Photooxidation of trichloroethylene on Pt/TiO_2. *J. Phys. Chem. B* **1998,** *102*, 1418-1423.

49. Grela, M. A.; Colussi, A. J., Photon energy and photon intermittence effects on the quantum efficiency of photoinduced oxidations in crystalline and metastable TiO_2 colloidal nanoparticles. *J. Phys. Chem. B* **1999,** *103*, 2614-2619.

50. Emeline, A.; Salinaro, A.; Serpone, N., Spectral dependence and wavelength selectivity in heterogeneous photocatalysis. I. Experimental evidence from the photocatalyzed transformation of phenols. *J. Phys. Chem. B* **2000,** *104*, 11202-11210.

51. Ikeda, S.; Sugiyama, N.; Murakami, S.; Kominami, H.; Kera, Y.; Noguchi, H.; Uosaki, K.; Torimoto, T.; Ohtani, B., Quantitative analysis of defective sites in titanium(IV) oxide photocatalyst powders. *Phys. Chem. Chem. Phys.* **2003,** *5*, 778-783.

52. Katoh, R.; Murai, M.; Furube, A., Electron-hole recombination in the bulk of a rutile TiO_2 single crystal studied by sub-nanosecond transient absorption spectroscopy. *Chem. Phys. Lett.* **2008,** *461*, 238-241.

53. Wakabayashi, K.; Yamaguchi, Y.; Sekiya, T.; Kurita, S., Time-resolved luminescence spectra in colorless anatase TiO_2 single crystal. *J. Lumin.* **2005,** *112*, 50-53.

54. Jung, K. Y.; Park, S. B.; Anpo, M., Photoluminescence and photoactivity of titania particles prepared by the sol-gel technique: effect of calcination temperature. *J. Photochem. Photobio. A* **2005,** *170*, 247-252.

Chapter 6: Conclusions

We have used time-resolved spectroscopy techniques to study two different systems: organic charge-transfer complexes and TiO_2 photocatalysts. In each case we show that spectroscopic observables give insight into the action of the electrons and holes responsible for their function.

6.1: Charge-Transfer Complexes

In chapter 3 we reexamined a series of donor:TCNB complexes previously studied by Hubig and Kochi, who primarily used diffuse reflectance transient absorption.[1] Our time-resolved fluorescence measurements on single crystals yielded simple monoexponential decay kinetics with lifetimes lasting several nanoseconds for nearly all of the samples studied. By comparing the fluorescence of the single crystals before and after pulverization and dilution with $BaSO_4$ we found that the photophysics of the samples changed. Furthermore, we found that laser exposure also aversely affected the crystals and powders. In both of these cases, mechanical damage and photodamage resulted in shorter multicomponent fluorescent lifetimes than what was observed for single crystals. The process of photodamage was characterized as a single-photon process and we calculated large photobleaching yields on the order of 10^{-4} to 10^{-5}. Diffuse reflectance transient absorption experiments, which require higher laser fluence than fluorescence measurements, on these samples were difficult owing to their high-susceptibility to undergo photodamage that changed their decay kinetics. Using fast low power scans we were able to obtain decay kinetics that mirrored the fluorescence kinetics

to the extent that we could measure them, i.e. the first nanosecond. On a pristine sample there were no fast components in the decay. Subsequent scans on the same sample showed a fast decay growing in as the sample became photodamaged, yielding erroneous kinetics similar to those reported by Hubig and Kochi.

In chapter 4 we were able to obtain a more complete picture of what occurred after photoexcitation of a CT complex by studying pyrene:TCNQ. This complex did not suffer from the photo and mechanical damage problems that plagued the TCNB compounds. It also had a short monoexponential fluorescence lifetime of just 290 ps, a value that was well within our ability to also measure via transient absorption. We show that after photoexcitation, only one state, a tightly bound electron-hole pair, was made, and its induced absorption decayed at the same rate as that of the fluorescence. The result indicates the material probably would not work as a stand-alone photovoltaic system, and has important implications for attempting to use CT interactions to extend the visible absorption of other photovoltaics. When the donor and acceptor are in direct contact with each other, like these systems of small molecules, it is unlikely anything other than recombination will occur. On the other hand, work with block co-polymers by the Friend group has shown charge separation can occur in CT systems, if large bandgap spacers are engineered between donor and acceptor.[2] Future work with these small molecule systems might be the identification of donors and acceptors that crystallize as CT complexes in such a way that lead to electron-hole pairs that are as not as tightly bound as those studied here. Or ones that undergo subtle geometry changes that make recombination less favorable after charge transfer occurs.

6.2: Au@TiO_2 Yolk-Shell Photocatalysts

Chapter 5 uses the spectroscopic techniques developed to study the CT complexes to look at a set of systematically varied Au@TiO_2 yolk-shell photocatalysts. As the crystallinity of the TiO_2 shell was increased, the photocatalytic activity and photoluminescence lifetime also increased, but the transient absorption kinetics remained the same. In this study we find the photoluminescence is strongly correlated with the surface environment of the catalyst, and therefore one of the most insightful tools in evaluating these materials. Furthermore, the photoluminescence decay rate was also shown to be dependent on the excitation wavelength. When low energy photons, $\lambda > 300$ nm, were used, the large differences in photoluminescence lifetime vanished. In this we establish the necessity of high energy photons to make meaningful comparisons in this class of materials. Two other important observations lead us to conclude emissive and catalytically active sites are different from one another but affected by the same electron-hole recombination processes: one, the emission wavelength is the same for each sample indicating the emissive sites have similar energies. Two, the plot correlating photocatalytic activity and lifetime does not go through the origin, indicating there are always some emissive sites when there may be few or no catalytic sites.

Having established the criteria to obtain good correlation between PL lifetime and catalytic activity, future work on the Au@TiO_2 system aims to use spectroscopy to attempt to gain insight into the actual photocatalytic mechanism occurring in the TiO_2 water-splitting system. While the gold nanoparticle was necessary for H_2 production in the yolk-shell samples, it did not seem to have much effect on the photophysics. Current

literature suggests the photoexcited semiconductor injects an electron into the noble metal, where reduction of $2H^+$ to H_2 then takes place.[3] The lack of differences in the photophysics for TiO_2 with and without gold studied in chapter 5 seems to challenge conventional thinking. On the other hand, steady-state spectroscopy on TiO_2 samples incorporating plasmonic metals, shows the plasmon band of the metal shifts with exposure to UV light. This has been interpreted as the result of the transfer of the electron from the semiconductor to the metal.[4] One alternative model is that the reduction occurs on the TiO_2 surface, and then the reduced species migrates to the metal where the final product is formed. To test this hypothesis, commercial TiO_2 has been blended with gold and silica coated gold. With the silica coated gold, provided the silica is thin enough, the catalysis should still occur as the reduced hydrogen would still be able to migrate to the gold through the porous silica, but electron injection into gold should be blocked. Preliminary results on the silica coated gold-TiO_2 system have been inconclusive so far. The samples exhibited about 10% of the catalytic activity of non-SiO_2 samples, but it's unclear whether a ~10% shift in the plasmon band could even be detected.

Another interesting avenue of research for these samples would be the investigation of the wavelength dependence of the photocatalysis. It is clear from the PL results that different excitation wavelengths excite different states within the TiO_2. Perhaps one of the most intriguing observation was that the 350 nm excitation didn't yield PL decays with any correlation to the catalysis. The main UV output of the lamp used to do the photocatalysis is actually ~350 nm, and the band edge of anatase TiO_2 is about 380 nm. Comparison of PL lifetime vs. catalytic activity for different excitation wavelenghts

might give further insight into the states responsible for PL and those responsible for the catalysis.

References

1. Hubig, S. M.; Kochi, J. K. *Journal of Physical Chemistry* **1995**, *99*, 17578–17585.

2. Johnson, K.; Huang, Y.-S.; Huettner, S.; Sommer, M.; Brinkmann, M.; Mulherin, R.; Niedzialek, D.; Beljonne, D.; Clark, J.; Huck, W. T. S.; Friend, R. H. *Journal of the American Chemical Society* **2013**, *135*, 5074–5083.

3. Fox, M. A.; Dulay, M. T. *Chemical Reviews* **1993**, *93*, 341–357.

4. Hirakawa, T.; Kamat, P. V *Journal of the American Chemical Society* **2005**, *127*, 3928–34.

Appendix I: Palitra Operation and Repair

A1.1 Operation

Daily operation of the Palitra is not complicated and should not involve any tampering with internal alignment. Prior to usage, when there is no input beam, the lid is opened and three beam blocks (cut up business cards) are inserted at I4, M5+6, and D2, and I3 should be closed slightly (see Figure A1.1). The baseplate of the Palitra is not secured to the bottom of the unit with screws or any type of fastener but rather rests on a tripod; while working inside, care should be taken not to press down on it too hard as this can ruin the external alignment of the laser into the Palitra. The 800 nm laser should then be unblocked (from outside of the Palitra) and let into the unit. The first point to check/optimize is the quality of the continuum which will be seen on the card at I4. If I3 has been closed too much there might not be any continuum present; I3 should be opened slowly until a satisfactory continuum is present on the card. Typically, "good" continuum on the card is generated by opening I3 until just before double filamentation of the continuum occurs (a small white spot that appears in the center). At present, opening I3 presents the following sequence of colors leading up to usable continuum: yellow/green spot, smaller gold/yellow spot, ~2 mm yellow/red spot, orange/red spot (used). After satisfactory continuum is generated, I2 is closed slightly, but not so much as to affect the continuum at I4. Once I2 is closed slightly, the beam block at M5+6 is removed, allowing the 1st stage pump to hit the BiBO crystal X1. Closing down I2 ahead of time is intended to protect the crystal from the pump in the event that it is too intense. While the power is low (because I2 is closed down), the card at I4 will have a continuum spot and a smaller

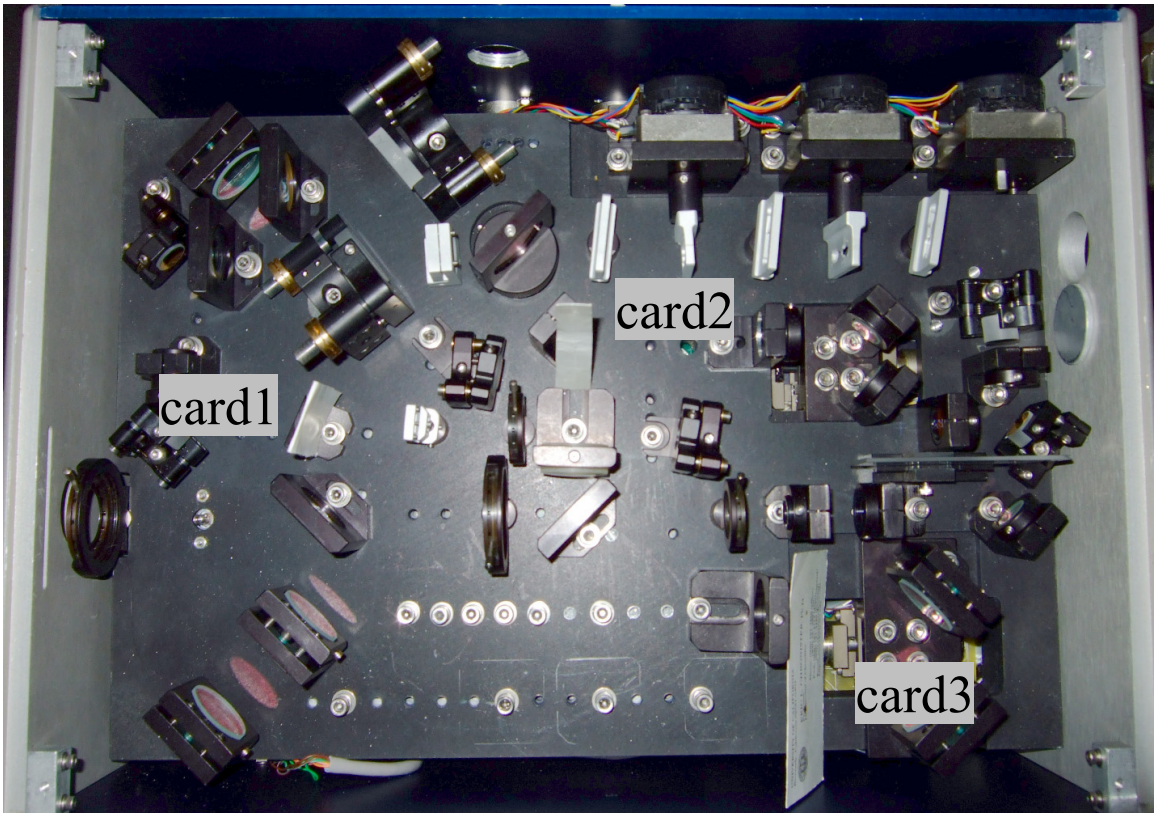

Figure A1.1: Picture of the Palitra with cut business cards in the three positions needed to begin operation of the instrument. "card1" consists of a folded card that tucks into the gap between aperture I4 and its set screw. "card2" is a long card that leans up against mirror M5+6. "card3" consists of a full size business card that leans up against lens L6 (see Figure A1.2 for complete identification key of all optics). When setting up the instrument, all three cards are put into place. The quality of the continuum is checked by looking at it on card1. Then card2 is removed, this lets the first stage pump go through the 1st stage amplification crystal, X1, and then onto card1. The user again looks at the beam spots on card1 to evaluate the amplification in the first stage crystal. Finally, card1 and then card3 are removed allowing full function of the unit. Also noticeable in this picture is the black baseplate, it is not screwed down at all, and clearly does not sit squarely in the enclosure; care must be taken not to perturb it.

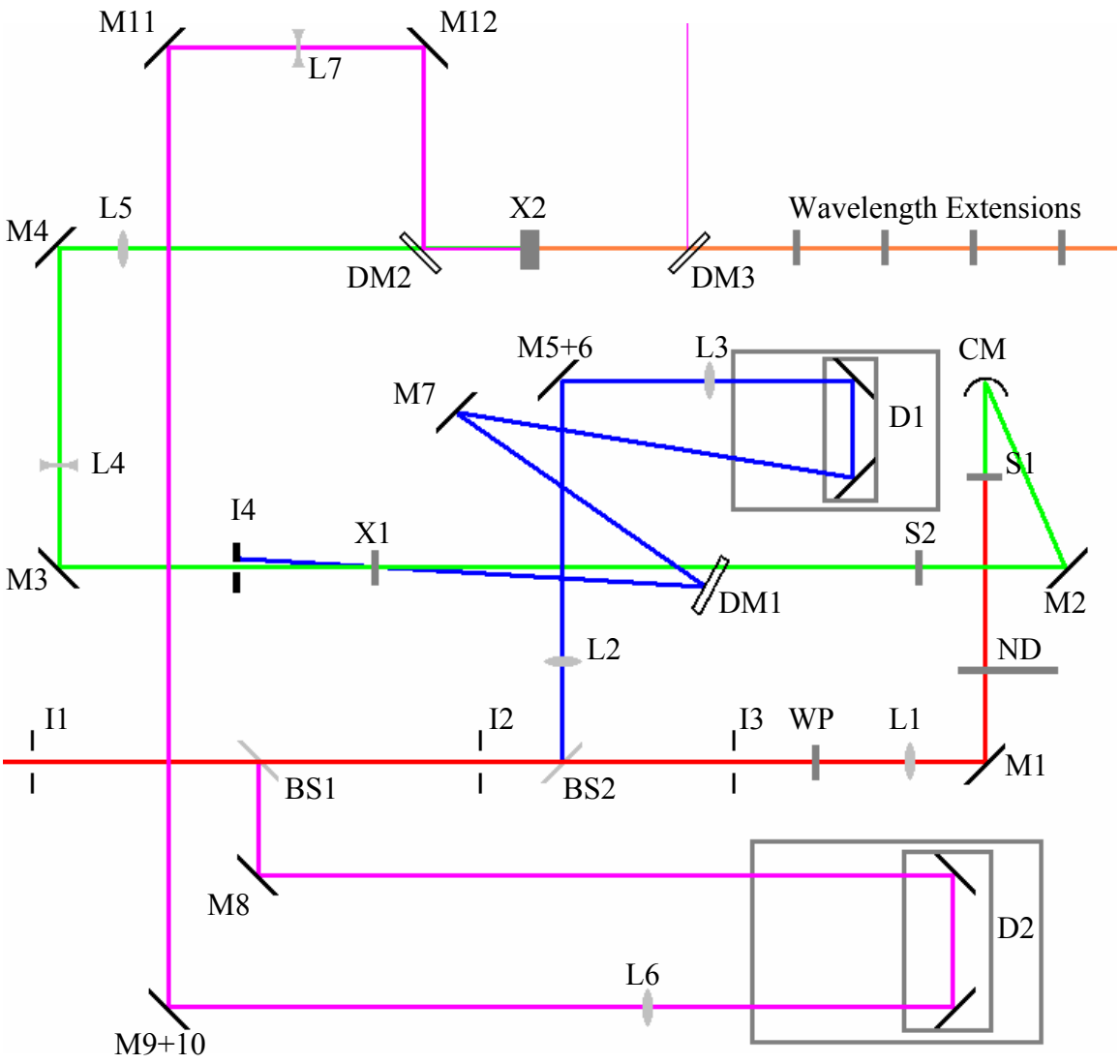

Figure A1.2: Optical layout of the Palitra FS OPA. Key: I - iris, M - mirror, BS - beamsplitter, WP - waveplate, L - lens, ND - graduated neutral density slide, S1 - sapphire, CM - curved mirror, S2 - stretcher, X - BiBO crystal, DM - dichroic mirror, D - delay stage. Beam color key: 800 nm input - red, continuum - green, 800 nm 2nd stage pump - purple, 800 nm 1st stage pump - blue, output - orange. Some mirrors are labeled with two numbers (ex. "M5+6") where in the operational manual there are two mirrors, but only one is present in this version of the Palitra.

red spot from the pump on it. I2 should then be opened slowly while watching the card at I4. As the pump power increases, the threshold for amplification will (hopefully) be passed and two additional spots, the signal and idler, will be seen on the card. The color of these spots will vary depending on the chosen output wavelength, often one is a green/blue spot and the other a pale red. I2 should continue to be opened until just before any flickering occurs, indicating the onset of parametric fluorescence from the crystal. Once the continuum and 1st stage amplification are optimized, the card at I4 is removed permitting the amplified seed to reach X2. Then the card at D2 is removed as well, and the unit should now be outputting the desired wavelength.

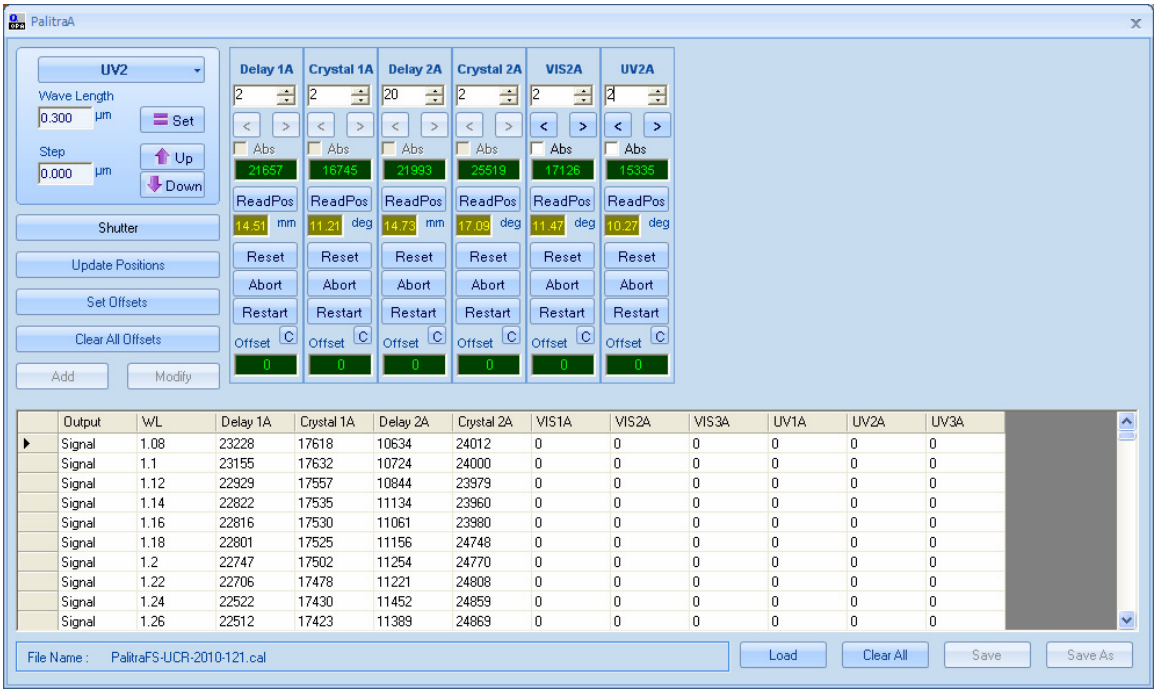

Figure A1.3: Palitra Commander motor control settings.

A1.2 Output Wavelength Selection

Wavelength selection on the Palitra is almost entirely computer controlled with the Quantronix Palitra Commander software. The motor control settings part of the software, Figure A1.3, is where all of the useful parameters can be set. Traditionally, the wavelength selection process is as follows: laser input into the Palitra is blocked, the correct wavelength extension crystal is chosen from the top-left menu in the program (currently "UV2", in Figure A1.3), and the exact wavelength for that range is entered into the wavelength box in μm. Pressing the "= Set" button right next to the box starts an automated process that moves D1 and D2 and rotates X1, X2, and the wavelength extension crystals to the positions and angles that will generate the desired wavelength. The settings of each wavelength are stored in a calibration file. And finally, the correct periscope shaped output filters are placed outside of the Palitra to remove unwanted wavelengths (ex. a wavelength setting of 350 nm will also have a substantial amount of undoubled 700 nm light with it).

After the Palitra's repair and reconfiguration for use with the Libra laser system, the calibration file is no longer accurate. The crystal angles are still pretty close, but the delays are all quite wrong. The following section covers setting the desired output wavelength without relying on the calibration file. One important consideration is: BEFORE CHANGING ANYTHING, THE CURRENT WORKING SETTINGS FOR THE CURRENT WAVELENGTH SHOULD BE RECORDED. Before changing any of the settings, the laser input into the Palitra should be blocked. While its delays are wrong, the calibration file can still be used indirectly to get a rough guess of what they should be.

Shown in Figure A1.3, the calibration file is constantly open at the bottom of the program; if possible, find the current wavelength in use and compare the values for the delays in the file with the current working values for that wavelength. Record the difference for both delays. If the desired wavelength requires a different wavelength extension crystal, select it from the dropdown menu (top-left in Figure A1.3), then type in the wavelength in the box, and hit the "= Set" button. The software will set the delays and angles using the calibration file, the angles will likely be close, but the delays will be incorrect. The difference in the delay values for the previous wavelength and the calibration settings for that wavelength can now be used to set the delays close to what they need to be for the new wavelength. In Figure A1.3, with the "UV2" crystal selected, there are six columns, one for each optic involved in generating the desired wavelength. However, due to a limitation in the program, to change the delays, the user must select "Signal" from the drop down menu (instead of UV2) to change the first four columns (Delay 1A, Crystal 1A, Delay 2A, and Crystal 2A). The last two columns correspond solely to the angles of the wavelength extension crystals, these should be changed last, if at all. Having set the drop down menu to "Signal," the delays may now be changed. The box directly below the column title is the step size and right below that are left and right arrows for increasing/decreasing the delay/angle by the above value. The current value for the delay/angle is given in two formats: a green box with a number from 0 to 30000 steps, and below it a number in mm or degrees. Set the values for Delay 1A and 2A based on the previous wavelengths deviation from the calibration file, briefly allow the laser into the Palitra and see if there is any output (if there is output, of the desired wavelength of

course - not continuum generation!, skip to the next section: "Fine Tuning"). Probably there will not be any output and the some hunting for the delays will be needed. At this point, the lid of the Palitra should be opened, cards should be placed at I4 and D2, and the laser input into the Palitra should be enabled. If the continuum is not already optimized, put an additional card in at M5+6 and optimize it according to the above section - remember to remove the card at M5+6 when done. The card at I4 will have (at least) two spots on it, the continuum and the 1st stage pump (if it has more than these, then the delay is close). While watching the card I4, Delay 1A should be changed. The step size should be fairly large 50 - 200 steps, and the negative direction should be scanned first (the motors should never be set above 30000 steps). When the delay is correct, there will be a small often subtle flash of light and the signal and/or idler spots should appear as well. It's sometimes easier to do this with a partner, one scanning the delays and one watching the card. These nonlinear effects should vanish if either the continuum or 1st stage pump are blocked (if they persist otherwise then something other than amplification is occurring - possibly damaging the crystal!). Once evidence of amplification occurring is observed, the step size for the delay should be decreased, and the delay changed in medium steps until the intensity of the signal/idler are maximized by eye. Fine tuning will be performed later. The card at I4 is then removed, as well as the card at D2. When the amplified continuum and the 2nd stage pump are not synced, the 2nd stage pump will typically generate continuum in the second BiBO. Prolonged exposure of the 2nd stage pump to the crystal without proper seeding can damage it, so care must be taken to attempt to figure out the correct value for Delay 2A in a timely manner. DM3 can also be

damaged in this manner from the residual pump beam. Delay 2A is to some extent easier to optimize than Delay 1A; when the timing is correct the beam can be very bright. The best way to optimize it is to observe a sheet of paper placed outside of the Palitra in the path of the beam and scan the delay with large steps (in the negative direction first), taking care not to exceed 30000. When the correct delay is met, the flash should be quite noticeable and should be the correct wavelength (or close to it) as well. The amount of continuum the crystal generates will decrease as well as the seed promotes efficient generation of the desired wavelength. Once this has occurred, the correct periscope output filter should be attached.

A1.3 Fine Tuning

Day to day fine tuning of the Palitra output is performed with an Ocean Optics USB4000 spectrometer operated with Overture software. The output of the Palitra is scattered with a beam block and the spectrometer is placed close to it so that some of the scatter is detected. It is important that the beam block and spectrometer are firmly in place; a business card beam block will move around due to air currents and make the laser appear less stable than it really is. Once the spectrum and intensity are visible in Overture, the Palitra Commander's motor control settings can be adjusted. If the wavelength is correct, then typically only Delay 1A and Delay 2A need to be optimized (remember to select "Signal" in the drop down menu to be able to change these). Changing the crystal angles can affect the power output, but they also affect the wavelength of the output, so care should be taken. The angles for the crystals in use,

Vis2A and UV2A in Figure A1.3 for example, will have the most impact on the wavelength. Specifically the last crystal, UV2A in this example, changes the wavelength significantly. The following is an example for tuning the Palitra to 350 nm using the UV2A crystal: First "Signal" is selected and Delay 1A and Delay 2A are set to maximize the signal in Overture. With the signal maximized just by changing these two delays, "Clear all offsets" should be clicked. The Palitra Commander Software records changes at the bottom of each column, clearing all the offsets enables the user to be aware of how far he is from his start point. "UV2" should then be selected from the drop down menu and UV2A is adjusted slightly. Moving it too far will result in total loss of output which should be avoided, it should only be moved a few steps at a time. Watching the spectrum in Overture, it will become apparent very quickly if the angle should be increased or decreased to reach the desired wavelength. The effect of Vis2A usually just increases/decreases the signal or changes its shape, it should not have to change much. Having adjusted UV2A and moved the output wavelength a little bit closer to the desired wavelength, "Signal" should again be selected from the drop down menu. This time the delays and the angles should be adjusted to maximize signal. The process from here on repeats itself, "UV2" is reselected and the UV2A angle is changed a little bit more to move the output closer to the desired wavelength, and so forth. It is important that small steps are taken and the output is "walked" over to the correct wavelength. As there are six different variables in this case, changing one by a large amount and losing all output will only complicate the process and potentially damage the crystals due to the loss of seeding. Each time the Pailtra is used, the settings should be checked with the Ocean Optics

spectrometer. Finally, note that placing the spectrometer in a way such that the scatter enters it at an odd angle can distort the spectrum or shift the detected wavelength.

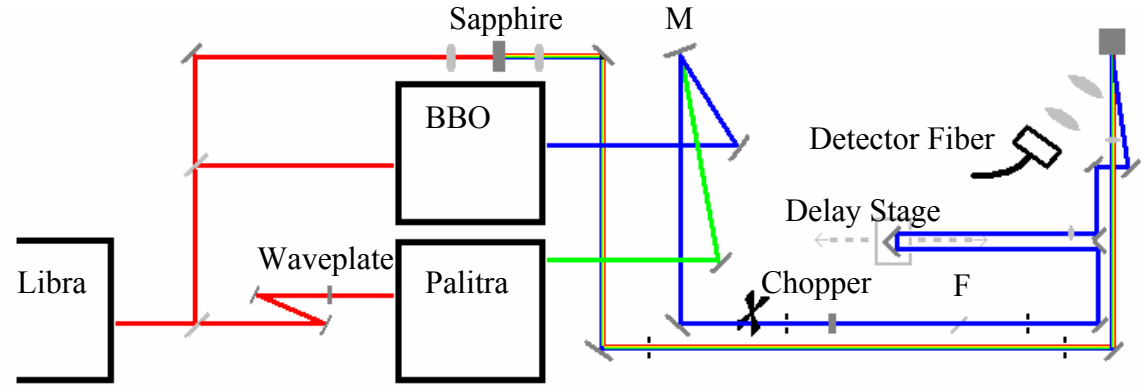

Figure A1.4: Layout for the Libra laser system.

A1.4 General Troubleshooting

Troubleshooting the Palitra is a complicated process and all care should be taken to determine if the problem really resides in the Palitra or is the result of something external to it. As shown in Figure A1.2, the beam going into the instrument is split into three parts which makes the input alignment extremely critical as all of these beams at one point or another must precisely recombine with each other later on to generate the nonlinear processes that make the amplifier work. At the same time, it is also very difficult to determine where and what the exact problem is with the system. This section assumes the user has already attempted to "fix" the Palitra exclusively by changing

delays and angles with the Palitra Commander software, and that the delays and angles that previously worked for various wavelengths (which are all in the Palitra logbook) are no longer working. Before attempting to further fix the Palitra, it should be set to a wavelength that previously worked. Also at this time, when setting it the previous values, the user should watch each crystal and delay stage while moving them to make sure the motors are not stuck (if a motor is not working, see the section "Device Failure"). In the event of loss of Palitra function, the two easiest external factors possibly responsible are the input power and pulse compression.

At present, with the Libra running at 3.8 W, the input power to the Palitra is about 0.90 W. If the Palitra stops working and it is determined that the Libra power has dropped, then more than likely the problem isn't the Palitra and all effort should be made to restore the Libra power or if necessary change the beamsplitters directly outside of it (see Figure A1.4) to pass more power into the Palitra. In the event that the beamsplitter must be changed, because alignment into the Palitra is so critical, it's a good idea to put in temporarily an extra mirror or two (before the Palitra!) and some irises and beam the signal through them prior to changing the beamsplitter, then after changing it, adjusting it to make the signal travel through them again. As noted later in this section, the internal irises of the Palitra are insufficient to properly align the beam going into it.

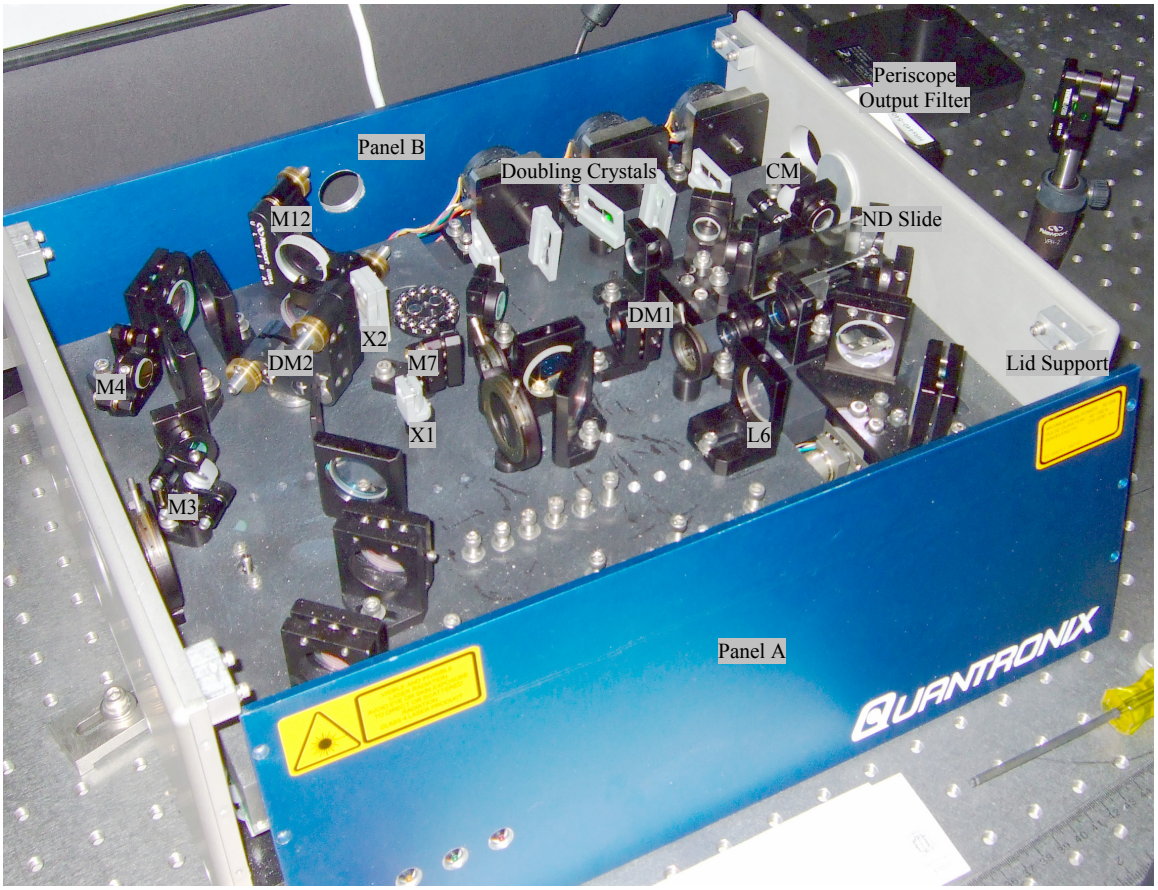

Figure A1.5: Photo of Palitra maintenance. The labeled optics are the ones primarily used in the troubleshooting and alignment process. The ring of magnetic ball bearings next to X2 is where DM3 is placed in the Palitra.

If the laser power is good but the grating for pulse compression is not optimized, the problem will be most evident in the visual appearance of the continuum inside the Palitra being different from normal - regardless of how much I3 is opened or closed. The best way to fix this problem is to observe the much larger continuum from the transient absorption setup and optimize the grating with it. When the pulse compression is best, the required input power the generate continuum is at a minimum. The optimization

procedure for this is to reduce the input power by simply closing the iris before the sapphire until the continuum is barely flickering, the grating stage is then moved forwards or backwards, whichever results in a stronger continuum, and then the iris is closed a little more and the process repeated until the point at which the continuum cannot be optimized any further.

Assuming the power is the same and the pulse is optimized, the next probable source for Palitra failure is the laser alignment going into it. As seen in Figure A1.4, the laser table has only a few optics prior to input into the Palitra, two mirrors and a waveplate, all of which should not be moved or adjusted for day to day use. Irises I1 and I3 (Figure A1.2) are intended to serve as guides for the input into the Palitra, however, they are so close to each other that they are insufficient to optimize the laser input to the Palitra. In this one case the large size of the laser mode on the Libra becomes a burden and makes it difficult to tell if the beam is centered as the edges of it are chopped off by the waveplate just outside of the Palitra (important note: the Palitra should never be operated with the waveplate removed, removal of the waveplate changes the beams polarization and subsequently the transmission/reflection ratio of the beamsplitters inside the Palitra, resulting in too much power going to the 1st stage crystal and sapphire, potentially damaging them!). Instead of aligning to the irises, ensuring that the delays and crystal angles are set to an output wavelength that was working previously, the best way to optimize the alignment into the instrument is to make small adjustments to the two alignment mirrors outside the Palitra and watch for output. Prior to making any changes the first step is to observe all the details of the current setup as much as possible, and to

read this entire section too. While working on the Palitra and making changes, it is often vital to be able to compare or go back to the previous conditions, reading the entire troubleshooting procedure will give the user insight as to which settings are the most important to keep track of. The positions of the mirrors should be noted, and in general it's a good idea to familiarize oneself with the relative location and appearance of all the beams inside the Palitra using cards, and, to the extent possible, the internal irises. The crystals should be checked for damage. The periscope filter on the output of the Palitra should also be removed and current output should be observed (Figure A1.5, top right corner, the periscope filter screws in to the outside of the panel). The 2nd stage pump and amplified seed are supposed to hit X2 at the same spot and remain parallel and on top of each other, removing the periscope filter permits one to check this alignment (the beams will appear not to overlap if it is left in). The pump will outshine the seed more than likely, but by putting a card in and out of the way of the 2nd stage pump at D2, will permit one to see if the 2nd stage pump and seed are overlapped (at X2 and outside of the Palitra). Finally, of all the things to check, one very important consideration is whether or not amplification is occurring at the first stage crystal (again: ensure the delays and angles are set to values that previously worked!) and also if the continuum, amplified or not, goes through I4. If the continuum isn't going through I4, then the alignment has definitely changed.

At this point very small adjustments to the mirrors outside of the Palitra can be made, one mirror in one axis at a time to begin with. Without great care, and sometimes even with, it is very easy to move the mirrors and change the alignment in such a way

that it is next to impossible to find the working alignment or go back to the original position. If there is 1st stage amplification at X1 then the alignment shouldn't be too far off. While moving the mirrors and looking for output, care should be taken to keep checking for 1st stage amplification. If it is lost too, then one may conclude the alignment is becoming worse.

The next step in working on the Palitra depends on the outcome of adjusting the input mirrors. In the best case scenario, signal is observed. If this occurs, then the periscope output filter should be put back on, and then, using either the Ocean Optics spectrometer or a power meter, the mirrors should continue to be adjusted for maximum power. The second best scenario is if the first stage amplification was previously not working, but now is working and the amplified continuum goes through I4. In this case, Delay 2A might only need to be changed to recover signal. The third scenario is if first stage amplification is working and the continuum goes through I4, but still there is no output - regardless of Delay 2A. In this case it may only be necessary to realign the amplified seed and the 2nd stage pump, which will be covered later on.

A1.5 Ab Initio Palitra Alignment:

The final scenario is that no amount of changing the input alignment can generate output nor can it even generate first stage amplification. This indicates that something has drastically changed inside of the Palitra itself. In this case the best course of action is likely to start from scratch. Figures A1.6 - A1.10 show the applicable beam path for each step of this process.

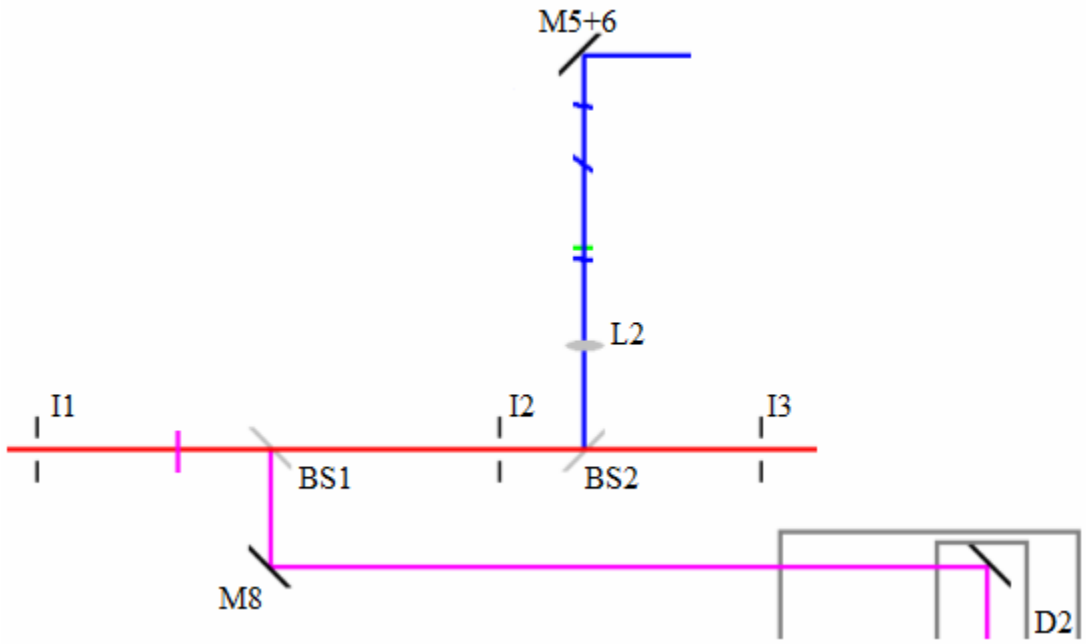

Figure A1.6: Beam path for input alignment. It is very important to block the beam at I3, M5+6, and D2.

The Palitra should be set to ("Signal") 1300 nm with the Palitra Commander software and Delay 1A should be set to 22150 steps (the correct position 09/22/2011), and any output filter still attached should be removed at this time. The first step is (attempting) to align the beam into the Palitra using the irises I1 and I3. Cards should be put at M5+6, D2, and right after I3, and the waveplate outside of the Palitra should be removed. This permits the full circular beam to go into the Palitra and also it allows much more power to go through the beamsplitters inside making it easier to see the beam on the irises. At no point should the cards be removed until the waveplate is put back in, or the crystals will get burned. Once the input beam is aligned to the irises, the waveplate is put back in and ensured that it itself is centered on the beam.

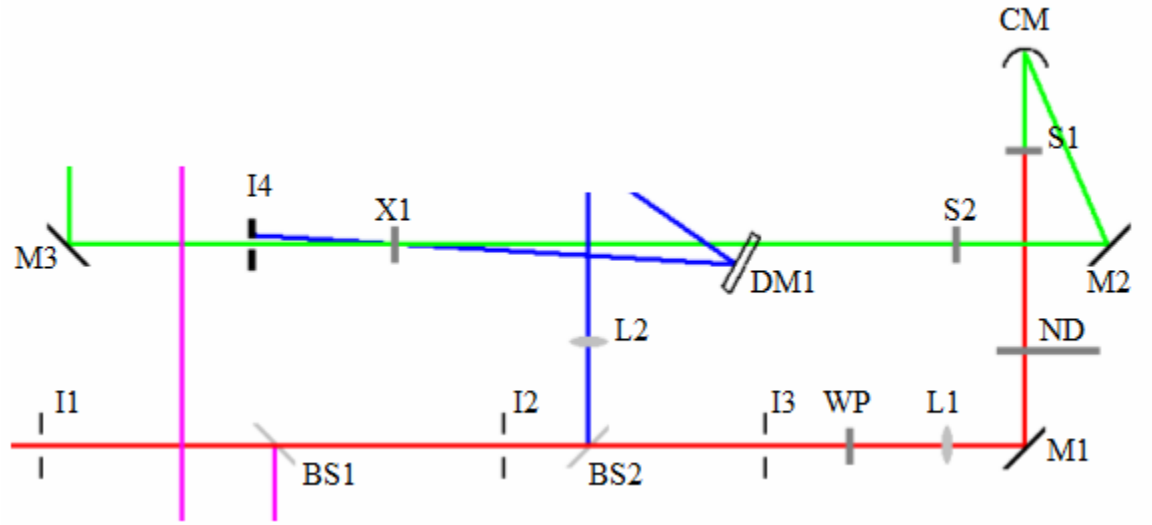

Figure A1.7: Beam path for continuum generation. Curved mirror CM is used to guide the beam through I4.

The continuum generation is the first thing to be set up and aligned in the Palitra. The card after I3 is moved to right before I4, the other cards are left in place. I3 should be opened or closed to optimized the power of the continuum. If need be, the ND slide can be adjusted if adjusting I3 alone cannot produce good continuum. Hopefully at this point, the continuum goes through X1 and then on to the card at I4. If it does not go through X1, the curved mirror CM should be adjusted until it does. The operational manual states that M2 may also be moved, however it does not appear to be possible to move this mirror in the enclosure. Once it goes through the center of X1, the continuum should be optimized again, and then the card right before I4 should now be moved to just in front of M3. M3 is a soft gold mirror, so care should be taken not to let the card physically touch it. The continuum should now be checked to see how well it goes through the aperture I4, and CM may need a very slight adjustment such that the center of the continuum goes cleanly through I4 and roughly through X1.

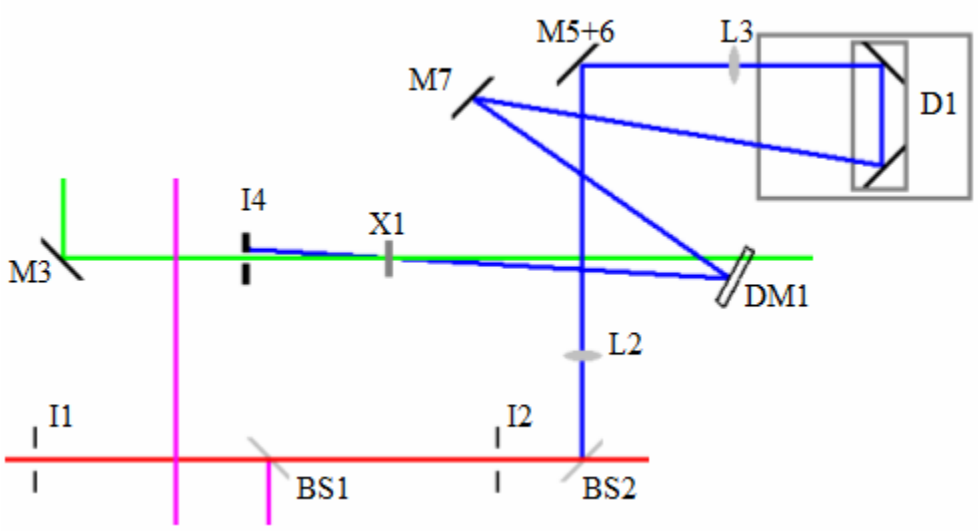

Figure A1.8: 1st stage pump beam path. Mirrors M7 and DM1 are used to overlap the 1st stage pump beam (blue) onto the continuum beam (green) in the first stage crystal X1.

Next is the alignment of the 1st stage pump. The card at M5+6 is removed and (ideally) the beam goes through/off L3, D1, M7, DM1, and X1 before being blocked by I4. I2 may need to be adjusted if the beam is too powerful (indicated by parametric fluorescence of the crystal). The card at M3 should be kept in place to prevent accidental exposure to the pump beam, while another card should be put just before I4. M7 and DM1 should now be used to spatially overlap the 1st stage pump with the continuum inside the crystal. Contrary to the schematic in the operational manual, the beams are NOT parallel, if they were then the pump would go through I4 and ruin the mirror M3! Note, because the input alignment has changed the initial guess for delay 1A may be incorrect, so there might not be any visual indicator, i.e. flash of light or appearance of signal/idler for achieving alignment at this point. The alignment is done by eye as well as possible. The following tips may be helpful during this process: 1) Looking at the

continuum and pump next to each other on a card just after DM1, M7 should be adjusted to make the pump the same height as the continuum, then, removing the card, and looking at the two spots at I4, DM1 should be adjusted to make the beams have the same height. This should process should be repeated until the beams have the same height before and after X1, indicating they go through the crystal at the same height. 2) The beams must cross inside of X1, one way of looking for this is to take a card and look at it before and after the crystal at roughly the same distance from it, the spots should appear at roughly the same distance from each other but have swapped sides. In other words, if the pump is on the left and the continuum is on the right before and after going through the crystal, then they certainly are not crossing inside of it. 3) If amplification is observed, then M7 and DM1 can be used to maximize it, in particular there will be a bright green spot between the pump and the continuum that can be optimized.

Once the alignment is believed to be done as well as possible, if there is no amplification, then the Delay 1A should be scanned with the Palitra Commander software while watching the card at I4 for amplification. If nothing is observed, then the pump alignment should be redone and the stage rescanned. This process may need to be repeated several times. Once the correct delay is found, M7 and DM1 should be used to maximize the intensity of the above mentioned green spot. As a last resort, L3 can be moved to change the pump focusing at X1. This might be necessary in the event the Libra irrevocably lost power. Moving L3 may change the alignment of the beam going into the delay stage, also the mount itself for L3 is not very good. It really should be kept as a last resort.

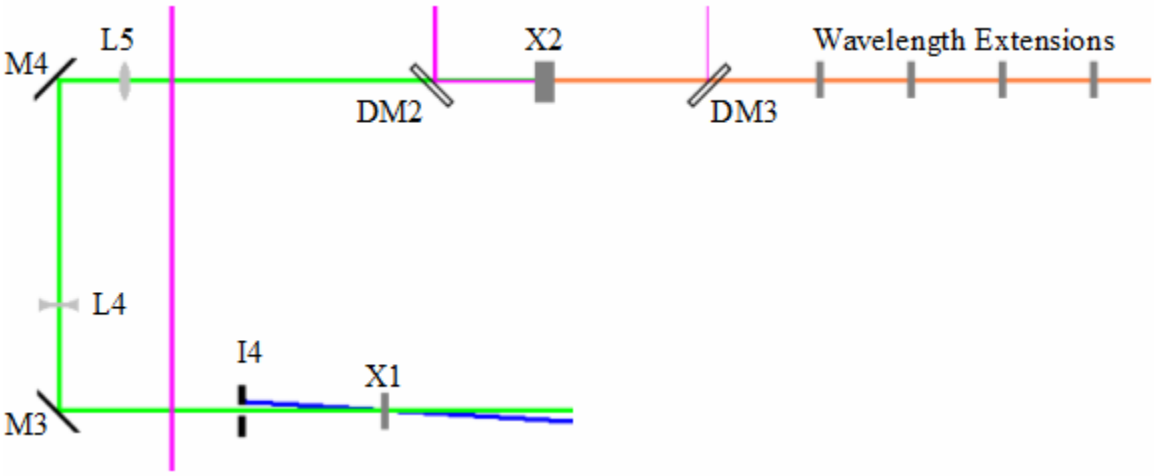

Figure A1.9: Beam path for the amplified continuum. After amplification in X1, the continuum is made to go through X2 and all of the wavelength extension crystals using mirrors M3 and M4.

Once first stage amplification has been achieved and optimized, the amplified continuum should take on a noticeable dull red hue from the self-doubled 1300 nm beam (it's easiest to see looking at the beam after M3). The card at I4 should be removed, and, ensuring that I4 blocks the 1st stage pump, the card at M3 is removed too. The amplified continuum should go through X2, all of the wavelength extension crystals, and then exit the Palitra. M3 and M4 should be used to ensure it travels through the centers of L4 and L5 and then roughly through the center of X2 before exiting the Palitra at roughly the center of the exit aperture. The collimation of the continuum should be checked by placing a beam block (as far away as possible), and L4 adjusted as need be (this was done 09/2011, but did not make much of a difference).

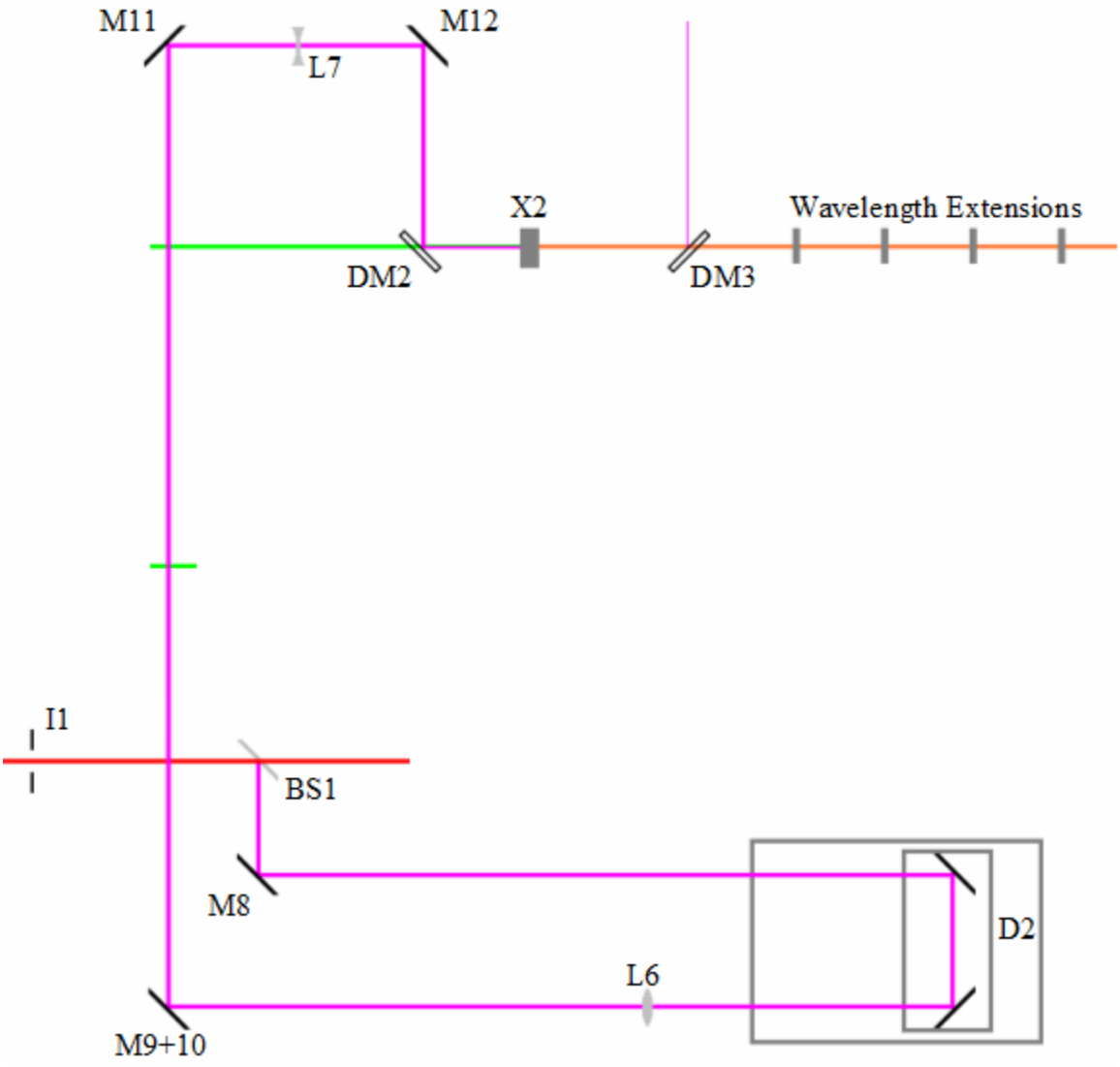

Figure A1.10: Beam path for the 2nd stage pump. Mirrors M12 and DM2 are used to overlap the 2nd stage pump beam (purple) on to the amplified continuum beam (green) in X2 and outside of the Palitra (past the wavelength extensions). The two beams must be on top of each other in both places to ensure they are perfectly parallel.

With the amplified continuum going through the second crystal and then out of the Palitra, the final step is to align the 2nd stage pump on to it. Given the size of the 2nd stage pump, this task is somewhat easier than the 1st stage alignment. The card at D2 and the pump dump mirror DM3 should be removed permitting the 2nd stage pump to pass through X2 and exit the Palitra. DM3 is not alignment critical and is on a magnetic mount, making its removal easy. M12 and DM2 are then used to move the pump beam around; M12 is used to overlap the beams at the crystal X2, DM2 is used to overlap them outside of the Palitra. The side panel (Panel B, Figure A1.5) of the Palitra should be unscrewed and moved out of the way (but not taken completely away - it's wired to the circuit boards) to access the set screws on M12. To see the beams at X2, a card may be placed directly in front of the crystal, however care should be taken that it doesn't catch fire! Once the beams appear to be roughly aligned, DM3 should be put back in. When the spatial alignment is close, there should be three spots visible coming out of the Palitra: the self-doubled signal (1300 + 1300 = 650 nm), the signal+pump (1300 + 800 = 495 nm), and the idler+pump (2080 + 800 = 578 nm). M12 and DM2 should continue to be adjusted until all three spots are exactly on top of each other (observing them at some distance from the Palitra). At this point, D2 can be scanned with the Palitra Commander software and there should be a noticeable flash when the correct delay is attained. Using a power meter, M12 and DM2 should then be adjusted slightly to achieve maximum power. If 2nd stage amplification fails to work or the power is very low, lens L6 may be moved to change the pump focusing on X2. Unlike the lens for the 1st stage pump, this lens is set up to be moved, and there are various holes drilled into the baseplate to permit it a wide

range of positions. Changing this lens's position should be done gradually. Focusing too tightly on the crystal can burn it. Each time the focus is changed, mirrors M12 and D2 are used to realign it with the amplified continuum seed, as explained above.

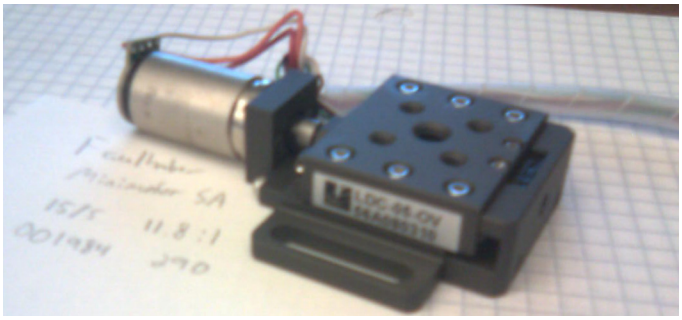

Figure A1.11: Delay stage D2. This stage was repaired 09/2011 by Pacific Laser Equipment (by Sabin Husariu). The model number is LDC-05-OV (serial# 56A080310).

A1.6 Device Failure

The Palitra contains 9 motors: 1) 1st stage delay, 2) crystal X1, 3) 2nd stage delay, 4) crystal X2, 5-9) doubling crystals. Each motor is controlled a small circuit board attached to the underside of the baseplate. There is one board per motor and each is labeled with the motor that is controls. The circuit boards are all connected to each other in series with RJ9 phone cords. One board has a USB connector, and a few others have DC inputs, however only one board needs to be powered. If a motor is stuck, at this point it is worthwhile to contact Quantronix or Pacific Laser Equipment (the company that makes the delay stages for Quantronix) and request help diagnosing the problem. A stuck

motor can sometimes be solved simply by increasing the voltage supplied to the motor or its velocity. These values can be set by closing the Palitra Commander software and using Microsoft's HyperTerminal program to communicate with the boards. The HyperTerminal commands are not provided in the manual and some of them are password protected, so it is necessary to contact Quantronix or Pacific Laser Equipment. If a motor needs to be removed or if a circuit board needs to be tested, then it will be necessary to access the underside of the baseplate. The best way to accomplish this is to tilt the baseplate on its side, specifically the side with X2 is down, while the side with D2 is up. It may be necessary to remove the notches that the Palitra lid screws into to be able to do this (Lid Support, Figure A1.5). In this way the wiring does not have to be disconnected, so troubleshooting with the computer can continue while being able to observe everything. There is nothing holding the baseplate down, side panel B near X2 should be unscrewed but left to sit next to it (the USB input from the computer connects to it so it shouldn't be removed), and panel A can taken off and set down as well (Panel A has LED's wired to it, but the wires are pretty long), and then one can just lift the board right up. When troubleshooting a stuck motor, the point of failure can somewhat be pinpointed by hooking the motor up to one of the other circuit boards and attempting to give it commands in HyperTerminal. If the motor can now move again, this means that its circuit board is bad and only it needs replacing. This is an important test because removal of a motor or delay stage will result in the need to realign the Palitra AND figure out the correct delays. A defective motor should be sent to Pacific Laser Equipment for fixing.